

Novel paths for switching of thermal transport in quantum materials

Dissertation

Presented in Partial Fulfillment of the Requirements for the Degree Doctor of Philosophy

in the Graduate School of The Ohio State University

By

Dung D. Vu

Graduate Program in Mechanical Engineering

The Ohio State University

2022

Dissertation Committee

Joseph P. Heremans, Advisor

Nandini Trivedi

Sandip Mazumder

Joshua Goldberger

Copyrighted by

Dung D. Vu

2022

Abstract

The realization of next-generation quantum-based computing and communication devices is dependent upon the advancement in thermal management. These challenges include but are not limited to sub-Kelvin temperature cooling for quantum computing and sensing and high-density thermal energy dissipation for electronics. Thermal circuit designs are limited by the conventional passive thermal components, such as thermal resistors and thermal capacitors, in contrast to a wide range of active components in the electrical domain. On the verge of the second quantum revolution, the development of materials that enable active switching of thermal transport in a wide range of temperatures and methods that provide advantages over current thermal management approaches are essential. In this thesis, I will introduce new mechanisms for controlling thermal transport in solids based on quantum phenomena.

Only recently was it recognized that topological properties of electrons in certain solids can have a dominant impact on the equations of motion of electrons. We discovered an ideal Weyl semimetal system, a topological material, that is field-induced: $\text{Bi}_{1-x}\text{Sb}_x$, with x varying from 0.04 to 0.22. We developed a theory for the topology-induced mechanism for the transport of heat by electrons, the thermal chiral anomaly, and experimentally proved its existence. Under the right conditions, the electronic thermal conductivity of a Weyl semimetal will increase linearly with the applied magnetic field.

Secondly, we investigated the effect of Bose-Einstein condensation of excitons, an electron-hole pair, on the lattice thermal conductivity of an excitonic insulator. Our data showed a surprisingly high low-temperature thermal conductivity in Ta_2NiSe_5 , an excitonic insulator, compared to those in Ta_2NiS_5 , a conventional insulator with a similar lattice structure. We postulated the enhancement in thermal conductivity is due to the coupling of exciton condensate to the lattice.

In the last chapter, we studied the effect of magnetism on the thermal transport of MnBi_2Te_4 . We discovered an intriguing switch of the magnetic field dependence of in-plane thermal conductivity in MnBi_2Te_4 as the material undergoes transition through different magnetic ordering in a magnetic field. Our study of the evolution of the magnon dispersion in the magnetic field revealed a strong, switchable interaction between magnons and the lattice, which strongly affects thermal transport in this solid.

Dedication

To my mom

Acknowledgments

First of all, I am blessed to work under the supervision of Professor Joseph P. Heremans for the last five years. Thank you for all the scientific discussions and puzzle-solving sessions full of great insights and fun. Your lectures were vital for me to grasp the knowledge of the field and I always have new ‘Ah’ moments whenever I review them. Your patience, curiosity, and optimism have constantly cheered me up throughout the projects in the lab. Your joyful character and lifestyle have been inspirational and influential for me during the last five years and will have a lasting impact on me in the future.

I started working in Thermal Materials Lab under the close guidance of Koen Vandaele, Bin He, and Sarah Watzman, to whom I am indebted. I’d like to thank lab members Yuanhua Zheng, Michael Adams, Mark Verosky, Renee Ripley, Brandi Wooten, and Joonsang Kang for the time and the knowledge we shared over the years. It was a pleasure working with you. Brandi Wooten is my academic sister who endured with me throughout the most difficult time of the lab and through the pandemic. Thank you for always having my back. I hope I was able to pass on some knowledge to the new generation of the lab: Minyue Zhu, Jiamin Wen, Mostafa Elnaggar, and Jackson Hise. I believe you will be successful and will continue the lab’s tradition of looking out for each other.

I'd like to thank Professor Nandini Trivedi and Professor Brian Skinner both in the Physics Department for their collaboration including many insightful discussions and theoretical ideas for explaining my data. In the first years of my Ph.D., I was lucky enough to collaborate with Professor Michael Flatte at the University of Iowa. Thank you for the amazing quality of work and your help with my academic career. The later part of my Ph.D. highlights collaboration with Professor Joshua Goldberger in the Department of Chemistry and Biochemistry. Thank you for the fruitful collaborations and many great ideas during the projects. In the Mechanical Engineering Department, I'm grateful for the tremendous guidance and support from Professor Sandip Mazumder throughout the program.

The first four years of my Ph.D. were funded by the Center for Emergent Materials (CEM), an NSF MRSEC. The CEM is an amazing research center that highlights broad collaborations cross-departmentally and cross-institutionally. I'm forever grateful for the chance of working on a day-to-day basis with a large group of brilliant minds. In the last year of my Ph.D., I'm honored to be awarded the Presidential Fellowship which helped me in concentrating my efforts on finishing my research. My latter projects were funded partly or wholly by the MURI, another group of top scientists in the field of thermal science. I truly appreciate all the discussions, support, and collaboration we had.

I'd like to thank the support from groups of friends in Columbus who cheered me on during these last couple of years. The parties, soccer games, bike rides, and poker nights will be an integral part of my memories in Columbus.

Finally, my Ph.D. would not be possible without support from my family. Thanks, Mom, for always encouraging me to carry on my academic career and Dad for taking care

of all other businesses at home so that I can concentrate on my study. My then-girlfriend now-wife, Trang, was the one who motivated me to start my Ph.D., which turned out to be one of the best decisions I've ever made. She has been with me through ups and downs in this journey and this dissertation literally would not come together without her help.

Sincerely,

Vita

2021-Present.....Presidential Fellow
Center for Emergent Materials Scholar
The Ohio State University
2020.....M.S. Mechanical Engineering
The Ohio State University
2012.....B.S. Mechanical Engineering
Korea Advanced Institute of Science and Technology

Publications

Vu, D., Zhang, W., Şahin, C., Flatté, M., Trivedi, N., Heremans, J. P., “*Thermal chiral anomaly in the magnetic-field induced ideal Weyl phase of $Bi_{1-x}Sb_x$* ”, Nature Materials 20, 1525–1531 (2021).

Kang, J. S., Vu, D., Heremans, J. P., “*Identifying the Dirac point composition in $Bi_{1-x}Sb_x$ alloys using the temperature dependence of quantum oscillations*”, Journal of Applied Physics 130 (22), 225106 (2021).

Vu, D., Nelson, R., Scudder, M., Goldberger, J., Heremans, J. P., “*Evidence of exciton condensate – phonon coupling in thermal transport properties of excitonic insulator candidate Ta_2NiSe_5* ”, In preparation.

Vu, D., Nelson, R., Wooten, B., Barker, J., Goldberger, J., Heremans, J. P., “*Thermal transport through magnetic ordering transitions of $MnBi_2Te_4$* ”, arXiv:2203.08032 (2022).

Vu, D., Heremans, J. P., “*Understanding the effect of different bands near Fermi level in thermal Hall effect of $Bi_{1-x}Sb_x$* ”, In preparation.

Vu, D., Watzman, S., Pan, Y., Kaustuv, M., Felser, C., Heremans, J. P., “*Giant thermal Hall and anomalous Nernst effect in $YbMnBi_2$* ”, In preparation.

Kang, J. S., Vu, D., Heremans, J. P., “*Identifying the optimum composition of $Bi_{1-x}Sb_x$ alloys for high-temperature thermal switching*”, In preparation.

Zhu, M., Vu, D., Heremans, J. P., “*The effect of doping on the thermal chiral anomaly in the Weyl semimetal phase of $Bi_{1-x}Sb_x$* ”, In preparation.

Fields of Study

Major Field: Mechanical Engineering

Table of Contents

Abstract.....	ii
Dedication.....	iv
Acknowledgments.....	v
Vita.....	viii
List of Tables	xii
List of Figures.....	xiii
Chapter 1. Introduction.....	1
1.1 Switching of thermal transport.....	1
1.2 Topological electronic phases in solids	5
1.2.1 Electronic band structure in solid-state crystals.....	5
1.2.2 Topology in band theory	7
1.2.3. 2D topological electronic systems, quantum Hall effects.....	10
1.2.4. 3D Topological electronic systems.....	15
1.3 Thermal conductivity in solids.....	21
1.3.1 Phonon thermal conductivity	22
1.3.2 Electronic thermal conductivity.....	26
1.3.3. Spin thermal transport and magnetic ordering.....	28
1.3.4 Techniques to separate common contributions of thermal conductivity	29
1.3.5. Thermal conduction by Bose-Einstein condensate.....	32
Chapter 2. Experimental methods.....	37
2.1. Voltage measurements and noises	37
2.1.1. Voltage measurement noises.....	37
2.1.2 Lock-in measurement.....	39

2.2. Temperature measurements	40
2.2.1. Thermometer selection.....	40
2.2.2 Working principle of thermocouple.....	41
2.2.3. Thermocouple calibration	43
2.2.4 Working principle of thermistors and thermistor resistance measurement	45
2.2.5. Thermistor calibration.....	47
2.3. Applications in heat and charge transport properties measurements.....	49
2.3.1 Hall and resistivity measurement.....	49
2.3.2 Longitudinal Magneto Resistance.....	52
2.3.4 Thermoelectric coefficient measurements	55
2.3.4 Thermal Hall and Thermal conductivity.....	58
Chapter 3. Thermal chiral anomaly in field-induced ideal Weyl semimetal phase of Bi-Sb alloys.....	62
3.1. Motivation and theory.....	62
3.2. Magnetic Field-induced $\text{Bi}_{1-x}\text{Sb}_x$ Weyl Semimetals.....	67
3.3. Magneto-Thermal Conductivity Measurements	70
3.4. Verification of the Wiedemann-Franz law and evidence for inter-Weyl point scattering.....	75
Chapter 4. Exciton condensate-phonon coupling in Ta_2NiSe_5 excitonic insulator.....	78
4.1. Introduction.....	78
4.2. Experimental Results	83
4.3. Discussion	89
Chapter 5. Thermal transport through magnetic ordering transitions of MnBi_2Te_4	95
5.1. Introduction.....	95
5.2. Results.....	98
5.3. Discussion of in-plane thermal conductivity	101
5.4. Magnon band calculation in a magnetic field.....	102
5.5. Thermoelectric and thermal Hall data.....	105
Concluding Remarks.....	109
Bibliography	112

List of Tables

Table 1. Classification of the topological electronic solid-state systems.....	15
Table 2. Thermometer types comparison.....	40
Table 3. Results of Type T thermocouple calibration.....	44
Table 4. List of Bi-Sb alloy samples used in the study	72
Table 5. Calculated phonon properties of Ta ₂ NiSe ₅ and Ta ₂ NiS ₅	89

List of Figures

Figure 1. A thermal switch is a two-terminal component with a Q vs ΔT relationship that is switchable between on and off states with an external control parameter ²	2
Figure 2. One-shot Adiabatic Demagnetization Refrigerator (ADR) puck from Quantum Design (top) in contrast to a continuous ADR cycle (bottom)	3
Figure 3. Free electrons in crystals move over the periodic potential of the nuclei of the atoms. Credit: Joseph Heremans.....	5
Figure 4. Schematic representation of a Bloch function in one dimension. Solid line represents the real part of a typical Bloch state. The dotted line is from the $e^{ik \cdot r}$ factor.	6
Figure 5. Zone folding and reduced zone scheme representation of the energy bands	7
Figure 6. Depiction of Berry connection χ as a vector potential in k space. Credit: Joseph Heremans	8
Figure 7. What is common between these figures of a dolphin, a cow, and a sphere? Their genus g is 0 i.e., their surfaces contain no holes. Credit: Brian Skinner.....	9
Figure 8. The trio of quantum Hall effects and their experimental realizations: the quantum Hall effect ⁶ , the quantum spin Hall effect ⁷ and the quantum anomalous Hall effect ⁸	10
Figure 9. Applying a magnetic field breaks time reversal symmetry: Forcing an electron to go backward on its trajectory breaks the law of Lorentz force.....	11
Figure 10. Band inversion in materials with strong spin orbit coupling. The conduction band near the gap obtains orbital characteristic of valence band and vice versa. Dotted lines depict the gapless edge states. Credit: Joseph Heremans.....	14
Figure 11. Band inversion in 3D topological materials can either form (a) TI or (b) Weyl semimetal with symmetry breaking. (c) Fermi arc surface states in a Weyl semimetal ²⁰ 18	18
Figure 12. Evolution of Weyl bands in a magnetic field parallel to the separation of the WPs and the mechanism of the chiral anomaly	19
Figure 13. Schematic plot for solutions of the phonon dispersion in 1D.....	23
Figure 14. Phonon thermal conductivity of a non-metallic crystal. ²⁵ Dominant phonon-scattering mechanisms are indicated along the abscissa. Upper curve is for a larger crystal	24
Figure 15. Normal phonon-phonon scattering process and Umklapp scattering process ²⁶	25
Figure 16. Electrical conductivity and electronic thermal conductivity of a metal as a function of temperature. ²⁵ The dominant electron scattering mechanism is indicated along the abscissa. The higher curves are for more perfect samples.....	26
Figure 17. Schematic illustration of a magnon or spin wave ²⁶	28

Figure 18. Magnon thermal conductivity of YIG, an electrically insulating FM, in an applied external magnetic field ²⁸	32
Figure 19. Creeping effect of Helium II superfluid.	33
Figure 20. Heat conduction in heat pipe and hypothesis for heat-pipe heat and mass transfer mechanism in superfluid.....	35
Figure 21. White noise is the flat part of a circuit's intrinsic noise spectrum on a noise power spectral density diagram. At lower operating frequencies, pink noise becomes more intense, emerging from white noise around the corner frequency and increasing at 3 dB/octave at lower and lower operating frequencies.....	38
Figure 22. Illustration of lock-in phase detection method's reference, measured signal and generated lock-in signal. Credit: Stanford Research Systems	38
Figure 23. Construction of a thermocouple for temperature measurement	41
Figure 24. Lakeshore Cernox bare chip packaging and dimensions.....	45
Figure 25. Wiring diagram for cernox resistance measurement. Resistances of cernox sensors are R_1 , R_2 and R_3	46
Figure 26. The reported result deviation in field $dT/T(\%)$ of CX-1050 sensor from Lakeshore website.....	49
Figure 27. Measurement configurations and sign convention for Hall and resistivity measurements.....	50
Figure 28. R_H as a function of Fermi level E_F	51
Figure 29. A device constructed for a longitudinal magneto resistance and longitudinal magneto thermal conductivity.....	52
Figure 30. Measurement configuration and sign convention for Seebeck and Nernst coefficient measurement	55
Figure 31. Measurement configuration for thermal Hall conductivity and Thermal conductivity.....	58
Figure 32. Thermal conductivity of copper	60
Figure 33. Modified wiring diagram to prevent heat loss at low temperature. Reds are manganin wires	61
Figure 34. Evolution of $\text{Bi}_{1-x}\text{Sb}_x$ alloys with composition and magnetic field:	67
Figure 35. $\text{Bi}_{89}\text{Sb}_{11}$ and $\text{Bi}_{85}\text{Sb}_{15}$ electronic and thermal properties:	70
Figure 36. $\text{Bi}_{95}\text{Sb}_5$, $\text{Bi}_{89}\text{Sb}_{11}$, and $\text{Bi}_{85}\text{Sb}_{15}$ thermal conductivity $\kappa_{zz}(H_z)$ dependence on longitudinal magnetic field along the trigonal direction at temperatures indicated:	73
Figure 37. Wiedemann-Franz law verification; temperature and angular dependence of the $\kappa_{zz}(H_z)$ increase:.....	75
Figure 38. Thermal conductivity analysis of 4 different samples of Ta_2NiSe_5 and of 3 samples Ta_2NiS_5 :	83
Figure 39. Specific heat of Ta_2NiSe_5 and Ta_2NiS_5	88
Figure 40. Mean free path calculated from the samples' diffusivity along the a-direction for the 50 μm thick Ta_2NiSe_5 and the 26 μm thick Ta_2NiS_5 samples, as function of temperature:	91
Figure 41. Schematic illustration of the phonon (A) and electron (B) dispersions in Ta_2NiS_5 and of the phonon (C) and electron (D) dispersions in Ta_2NiSe_5 :	93

Figure 42. Electrical transport data. Left panel: Field dependence of in-plane resistivity.
Right panel: Hall resistivity: 98

Figure 43. In-plane thermal conductivity of MnBi_2Te_4 : 99

Figure 44. Calculated magnon band evolution in an out-of-plane magnetic field:..... 103

Figure 45. Field dependence of thermoelectric coefficients Seebeck $S_{xx}(B_z)$ (Left
panel) and Nernst $N_{xy}(B_z)$ (Right panel): 105

Figure 46. Thermal Hall and Hall shows good agreement with Wiedemann Franz Law:
..... 107

Chapter 1. Introduction

1.1 Switching of thermal transport

Heat switches, also called thermal switches, are devices that alternate between good thermal conductors and good thermal insulators as needed.¹ When one is installed in the heat-conduction pathway between a hot, heat-producing component and a heat sink, the change in thermal conductance can be used to control the component's temperature. The thermal conductance of the heat switch can be controlled by an external input such as electrical voltage, temperature, or external magnetic field. As indicated in **Figure 1**, a thermal switch is defined as a two-terminal component with a Q vs ΔT relationship that is dependent on an external control parameter such as an electric field, magnetic field, or applied pressure.² The thermal conductance changes when this control parameter is changed.

The on/off switching ratio $r = K_{on}/K_{off}$ is a figure of merit for a thermal switch,² where K_{on} is the highest thermal conductance and K_{off} is the lowest thermal conductance that can be achieved by applying the control parameter.

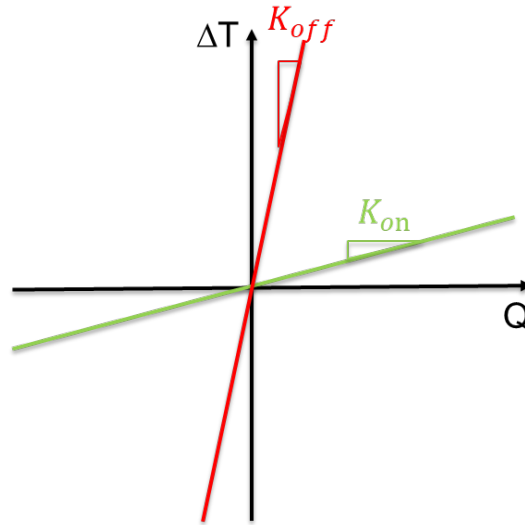


Figure 1. A thermal switch is a two-terminal component with a Q vs ΔT relationship that is switchable between on and off states with an external control parameter²

Heat switches can be used for a variety of purposes depending on the control input. Without the use of thermostats or heaters, temperature-activated heat switches can manage the temperature of heat-producing electronics or instrumentation, reducing power consumption and the need for heater control circuitry and software. One motivating example for thermal switches is spacecraft thermal management. Radiators that dump the spacecraft's excess heat into deep space must be sized to handle peak heat rejection loads. When the spacecraft generates far less heat, however, the same radiators may be overly effective in rejecting heat, causing the working fluid to freeze. Heat rejection rates and spacecraft temperature can be actively controlled using electric field-controlled thermal switches.

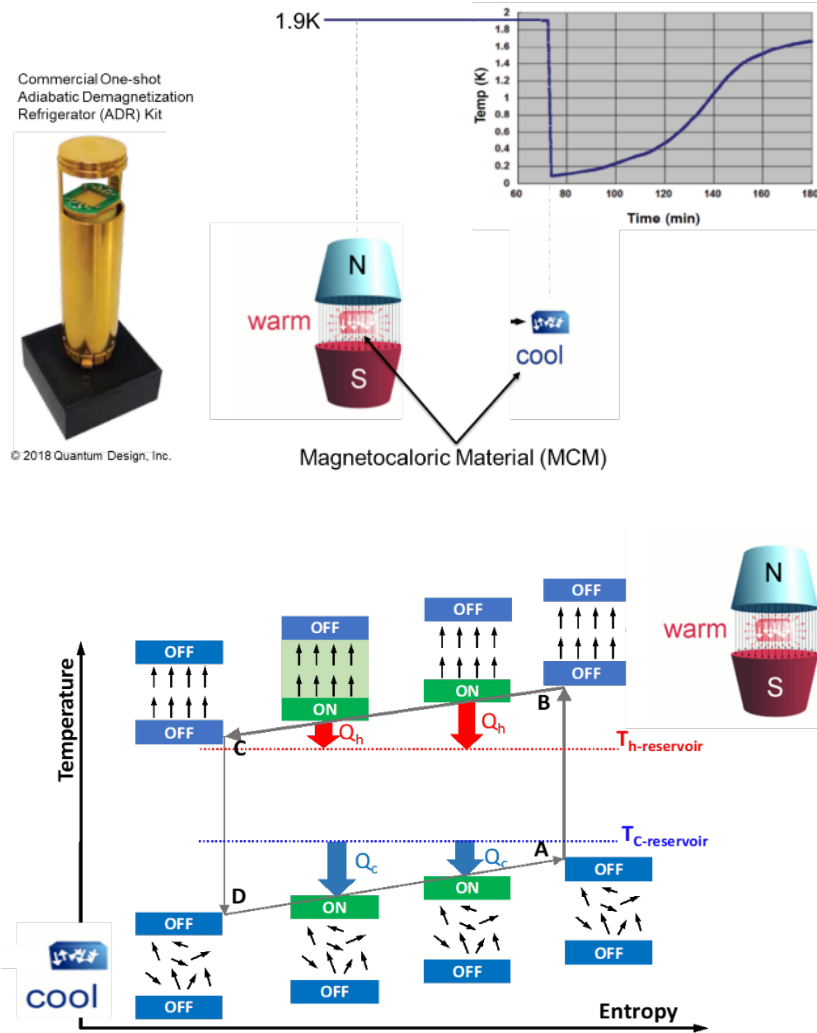


Figure 2. One-shot Adiabatic Demagnetization Refrigerator (ADR) puck from Quantum Design (top) in contrast to a continuous ADR cycle (bottom)

The magnetic cooling cycle is a promising technology for enabling sub-Kelvin refrigeration. Shown in **Figure 2** is the One-shot Adiabatic Demagnetization Refrigerator puck from Quantum Design. This device uses magnetocaloric material (MCM) which is a paramagnet. Cooling operation starts with a magnetic field to align the moments. When the field is off, the MCM returns to a disordered state and absorbs heat, and the temperature drops down to around 100 mK. However, this device cannot maintain the low temperature

for a long time and needs regeneration to get back to 100 mK again. To keep a stable temperature, a device like this needs to be operated in cycles. This means switching the field on and off continuously and a thermal switch is needed to bring the MCM in and out of thermal contact with the cold reservoir every time the field is switched. So far, only mechanical switches are found for this application. These switches are slow in switching frequency and prone to mechanical issues. Therefore, a solid-state heat switch that can be turned on by a magnetic field would be more desirable for this application.

Among the approaches to thermal switching, phase changing materials show good switching ratios and are heavily studied. Current phase changing materials rely on differential thermal conductivity between classical phase changes for thermal switching, for example: solid-liquid phase transitions or metal-insulator transitions. Our approach to thermal switching presented in this dissertation will be based on quantum phase transitions. The rest of Chapter 1 will provide theoretical background to the research projects presented in Chapter 3, 4 and 5. I will introduce topological electronic phases in Section 1.2. Topological electronic phase is an important concept in this dissertation since 2 out of 3 materials system used in this work (Bi-Sb alloys and MnBi_2Te_4) can be classified as topological materials. Section 1.3 provides background of thermal conductivity in solids which consists of contributions from different (quasi-)particles. In section 1.3, I will also discuss thermal transport involving Bose-Einstein condensation (Section 1.3.5), and magnetic phase transition (Section 1.3.3) pertaining data analysis in Chapter 4 and 5, respectively.

1.2 Topological electronic phases in solids

1.2.1 Electronic band structure in solid-state crystals

Electrons in single atoms occupy orbitals, or discrete quantum energy levels. In a solid-state crystal lattice, a large number of atoms arrange themselves into a periodic structure. In a crystal lattice, an electron is shared among atoms and the electron can hop between different atoms with momentum k .³ An electron now not only sees the potential from one atom but a periodic potential of the periodic arrangement of atoms.

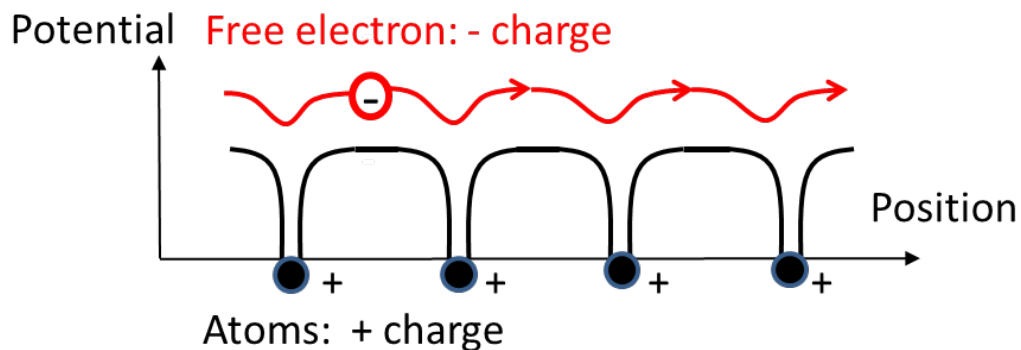


Figure 3. Free electrons in crystals move over the periodic potential of the nuclei of the atoms. Credit: Joseph Heremans

In this new problem, the electron's wavefunction $\psi(r) = \psi_0 e^{ik \cdot r}$, where ψ is the wave function and r is position, now not only depends on the momentum k but also subjects to a periodic function. Bloch theorem then states that the hybridized state wavefunction can be expressed as the product of two components: a plane wave that depicts a free electron wave function modulated by a periodic Bloch function $u(r)$ that depicts the effect of periodic potential in each unit cell on electrons. We have $\psi(r) = e^{ik \cdot r} u(r)$.

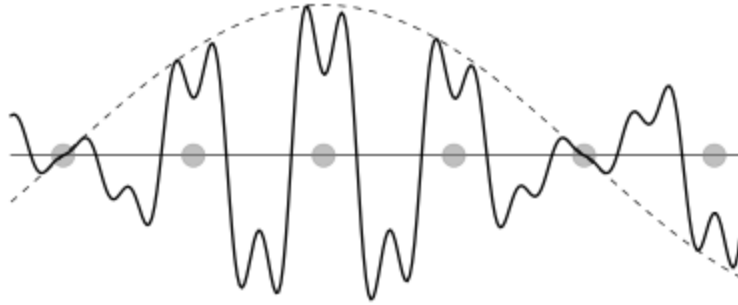


Figure 4. Schematic representation of a Bloch function in one dimension. Solid line represents the real part of a typical Bloch state. The dotted line is from the $e^{ik \cdot r}$ factor.

By plotting out energy $E(k)$, we can construct the electron band diagram (**Figure 5**). The momentum k can take only certain values since k must follow the periodic boundary conditions of the crystal. The de Broglie wavelength $\lambda = 2\pi\hbar/k$ associated with the wavefunction cannot be smaller than the minimum distance between 2 unit cells, the lattice constant a . The momentum in that each direction therefore has a maximum magnitude $\pi/2a$. The ensemble of allowable momenta in k -space is then defined as the Brillouin zone (BZ). The BZ shape is a real space to momentum space transformation the shape of the unit cell. Same as the unit cell in real space, the BZ has periodic boundary conditions. This allows zone folding and the representation of reduced zone scheme for the energy bands.

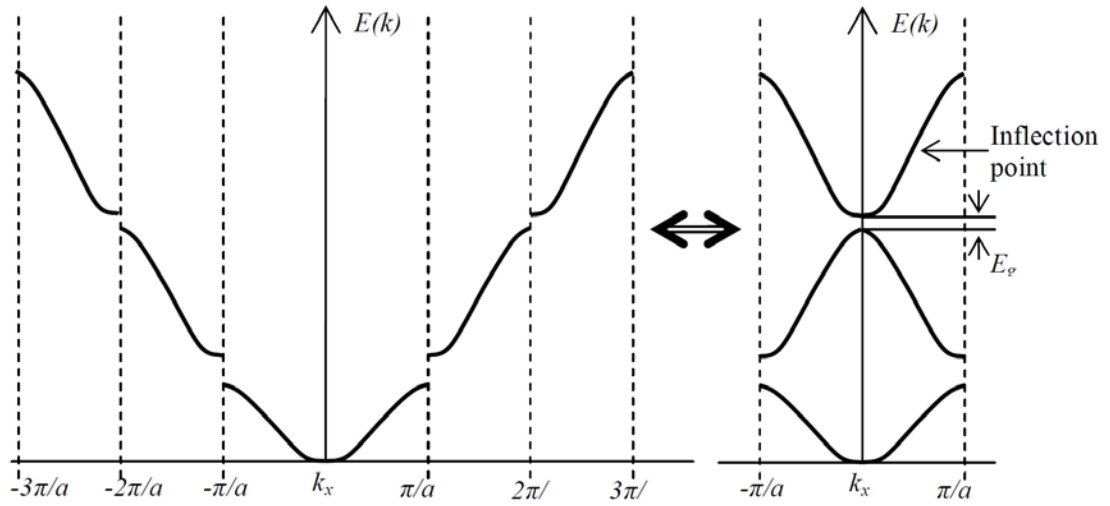


Figure 5. Zone folding and reduced zone scheme representation of the energy bands

1.2.2 Topology in band theory

We will go over some key characteristics of band structure that give rise to its topology. The Berry connection and Berry curvature will be discussed. We will draw some analogies to explain the role of topology in band theory.

Berry connection: Considering the electron wave function in a crystal, with each momentum k , the wavefunction has a r dependent spatial distribution that is centered at a specific r in the unit cell. This location defines the Berry connection χ , which is a k dependent vector field. Because the Berry connection is gauge-dependent, its local value cannot be observed. Berry connection can be thought of as analogous to the magnetic vector potential A in problems with magnetic fields in that only its curl has a physical meaning.³

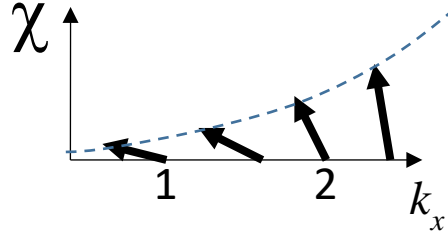


Figure 6. Depiction of Berry connection χ as a vector potential in k space. Credit: Joseph Heremans

Berry curvature: Now if we consider the electron band $E(k)$ in k -space, at each momentum point the electron wave function possesses a vector $\chi(k)$. Taking the curvature of this field with respect to k we have

$$\Omega \equiv \text{curl}_{(\chi)} = \nabla \times \chi \quad (1.1)$$

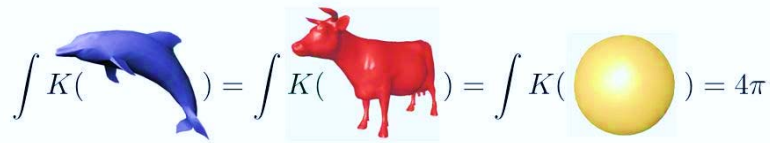
The Berry curvature can be calculated directly from wavefunction using Equation 1.1. Mathematically, Berry connection can be thought of as analogous to the magnetic field $B = \text{curl}_{(A)} = \nabla \times A$. The Berry curvature acts like a magnetic field in k -space, giving rise to the anomalous velocity, the equivalent of Lorentz force.

$$\dot{r} = \nabla_k \varepsilon + \dot{k} \times \Omega \quad (1.2)$$

$$\dot{k} = q \nabla_r \mu + q \dot{r} \times B \quad (1.3)$$

Symmetry properties of the Berry curvature^{4,5}: Berry curvature under basic symmetry operation: For Berry curvature $\Omega(k)$, the Berry curvature is inversion symmetric if $\Omega(k) = \Omega(-k)$. It can also be shown that for Berry curvature, it is time-reversal symmetric if $\Omega(k) = -\Omega(-k)$. Combining these two symmetries, if a system has both time reversal symmetry and inversion symmetry, $\Omega(k)$ must be zero for any k .

Chern number: The concept of a topological invariant emerges from topology, a branch of mathematics that studies properties of geometric objects that are conserved under continuous deformations. The Gauss–Bonnet theorem is its paradigm: the integral of geometric curvature K over the entire surface of an object is $4\pi(1-g)$, where g (the genus of the surface) is the number of holes in a three-dimensional shape (**Figure 7**). Its remarkable implication is that if one changes the object’s surface continuously without poking a hole through the object, g remains unchanged: it is a topological invariant.



$$\int K(\text{dolphin}) = \int K(\text{cow}) = \int K(\text{sphere}) = 4\pi$$

Figure 7. What is common between these figures of a dolphin, a cow, and a sphere? Their genus g is 0 i.e., their surfaces contain no holes. Credit: Brian Skinner

The integral of the Berry curvature, like the physical Gaussian curvature of a manifold, is a quantized topological invariant known as the Chern number. For the n^{th} electronic band, the Chern number is:

$$c_n = \frac{1}{2\pi} \int dk \cdot \Omega_n(k) \tag{1.4}$$

where $k = (k_x, k_y)$ is 2D crystal momentum. The integral is integrated over the entire Brillouin zone.

The electronic properties of a topological material are governed by a global invariant determined by applying the Gauss-Bonnet theorem to the Berry curvature in k space. These properties do not change continuously by defects or perturbations, an effect called topological protection, and can be very counter-intuitive. For example, unlike a

classic electron which would bounce off an obstacle such as a defect in a crystal, a topological electron must travel around a defect then continue with its trajectory if its velocity is topologically protected.

1.2.3. 2D topological electronic systems, quantum Hall effects

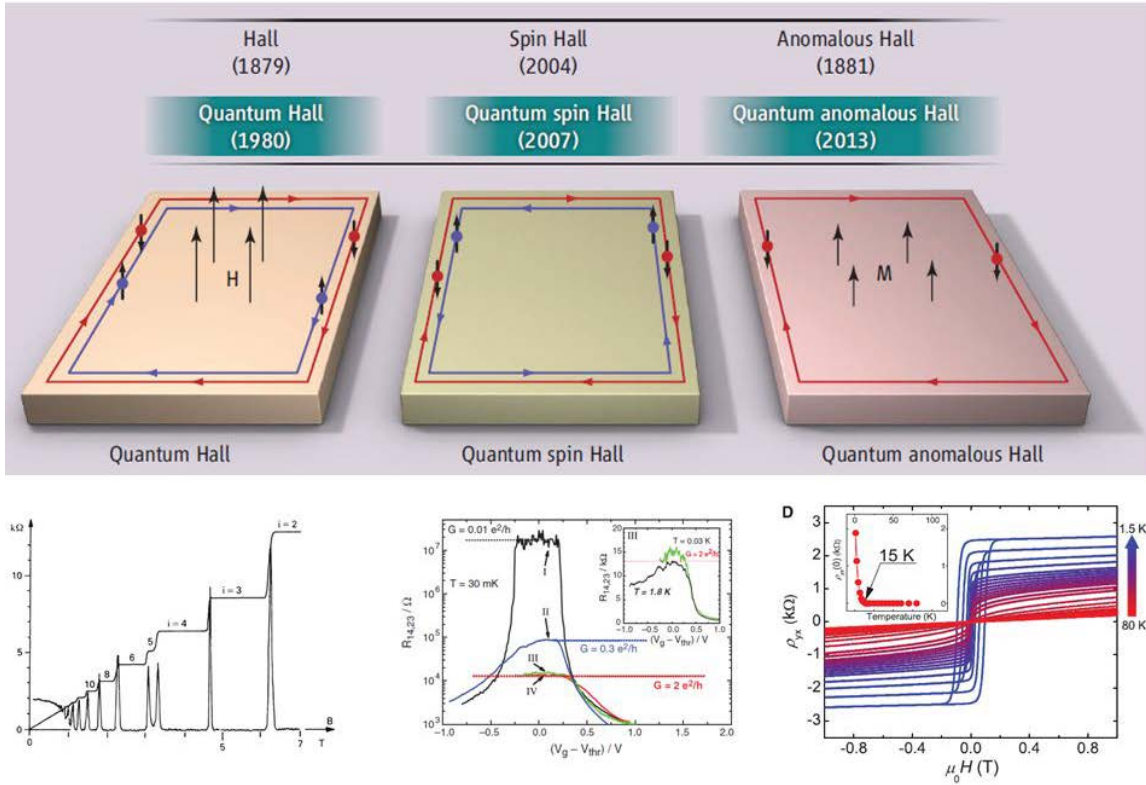


Figure 8. The trio of quantum Hall effects and their experimental realizations: the quantum Hall effect⁶, the quantum spin Hall effect⁷ and the quantum anomalous Hall effect⁸

Integer quantum Hall effect⁶: The integer quantum Hall effect is the most basic example of the Chern number appearing in a transport property. When a two-dimensional electron gas is placed in a strong perpendicular magnetic field at low temperature, the integer quantum Hall effect occurs. Here, the Hall resistance R_{xy} exhibits steps in magnetic field that jumps in quantized values determined by:

$$R_{xy} = \frac{h}{e^2\nu} \tag{1.5}$$

where e is the elementary charge, h is Planck's constant and the factor ν can take on integer values ($\nu = 1, 2, 3\dots$). As we will show next, ν is the Chern number for this system.

Quantization of the circular orbits (cyclotron orbits) of electrons results in quantized Landau levels (LL).⁹ If n LLs are filled and the rest are empty, as in an insulator, an energy gap separates the occupied and empty states. A magnetic field breaks time-reversal symmetry in quantum Hall systems by forcing electrons into spiral trajectories with a particular handedness determined by the magnetic field direction. Forcing an electron to travel backward on that spiral trajectory without flipping the magnetic field would violate the law of Lorentz force, $F = qE + qv \times B$. Either going forward or backward, the circular motion of the electron (cyclotron orbit) is preserved, time reversal symmetry is therefore said to be broken. For this reason, applying a magnetic field to a fermionic system would break time reversal symmetry. Broken time-reversal symmetry allows nonzero Berry curvature in k -space.

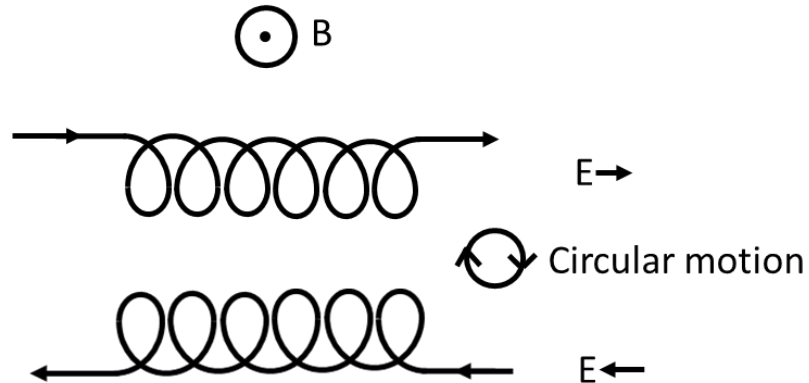


Figure 9. Applying a magnetic field breaks time reversal symmetry: Forcing an electron to go backward on its trajectory breaks the law of Lorentz force

As discussed previously, the Berry curvature acts like a magnetic field in the equation of motion of electrons in k -space¹⁰.

$$v_n(k) = \frac{\delta \varepsilon_n(k)}{\hbar \delta k} - \frac{e}{\hbar} E \times \Omega_n(k) \quad (1.6)$$

where $v_n(k)$ is velocity of electron with momentum k in the n^{th} band and $\Omega_n(k)$ is the Berry curvature of the n^{th} band. The anomalous velocity, which is a contribution to $v_n(k)$ in addition to the band dispersion contribution, is the second term in the equation. This velocity is always perpendicular to the electric field, resulting in a Hall current in the transverse direction. As a result of the equation above, in a two-dimensional band insulator the system's Hall conductivity is given by:¹⁰

$$\sigma_{xy} = \frac{e^2}{\hbar} \int_{BZ} \frac{d^2 k}{(2\pi)^2} \Omega_{k_x k_y} \quad (1.7)$$

We can immediately recognize the integral in Equation 1.7 is the Chern number thus it takes on integer value $\nu = 1, 2, \dots, n$. As a result, the Hall conductivity of a two-dimensional band insulator of noninteracting electrons is quantized.¹⁰ The transition as the LLs passes through the chemical potential is not continuous thus it induces changes in topology of the band structure and jumping of Chern number by integer numbers only. For the case of a 2D electron gas, the Chern number for each LL is 1.

The only condition for the quantum Hall effect to occur, as shown by the above derivation, is that the Chern number must be finite. Even in the absence of an external magnetic field, it is possible for the Chern number of some materials to be nonzero. A nonzero Chern number arises when the periodic boundary condition fails or there are singularities of Berry curvature (band crossing) in the Brillouin zone. If a topological material combines broken inversion symmetry with a strong coupling between electron

momentum and spin (spin-orbit coupling or SOC), edge states can exist even if time-reversal symmetry is preserved. For example, in a 2D topological insulator (TI), the two spin states will have nonzero Chern numbers with different signs. In this case, there exists counter-propagating spin-polarized helical edge states (**Figure 8**). This effect is known as the quantum spin Hall effect (QSHE).

Quantum spin Hall systems, 2D topological insulators and Z₂ classification:

As mentioned in the last section, the time-reversal symmetry is preserved in QSHE, the Hall conductivity vanishes and the Chern number, C , is zero. Yet, the Berry phase picked up by each spin is not necessarily zero. One can consider opposite spins picking up the same Berry phase and hence resulting in the same nonzero spin dependent Chern number, however, with opposite signs.¹¹ It was discovered that the QSHE can be described by other invariants, and therefore indeed realizes a novel topological phase at zero field, also with dissipationless edge states but different from the QHE. The Z₂ invariant determines the number of pairs of helical edge states in the system. ν is 0 or 1 when there are even or odd pairs of helical edge states, respectively.¹² If the topological analogy of Chern number is the number of holes an object has, then the analogy of Z₂ classification is the mobius strip. Starting from a cylinder which has 2 surfaces and then proceed to cut the cylinder along its length to get a strip, if one twist one edge 180° and reattach the 2 twisted ends of the strip, we get a mobius strip with one single continuous surface. If one twists the strip twice then reattach, the object once again has 2 surfaces, and so on. The model predicted by Kane and Mele¹¹ was realized in materials with strong SOC and band inversion which requires the existent of helical edge modes. The bulk-boundary correspondent requires the existence of

metallic gapless states on the surface for a smooth transition from topologically nontrivial state in the bulk to a topologically trivial state of vacuum without closing the gap in the bulk, hence the existence of protected surface states.

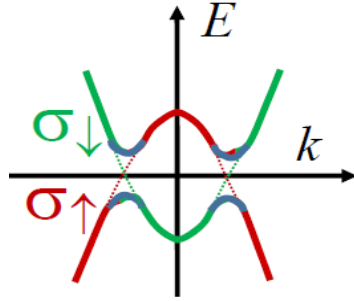


Figure 10. Band inversion in materials with strong spin orbit coupling. The conduction band near the gap obtains orbital characteristic of valence band and vice versa. Dotted lines depict the gapless edge states. Credit: Joseph Heremans

In a Z2 TI, the topological inverted band must come back to topologically trivial state at the boundary. The gapless edge mode allows this transition. In transport, the spin-polarized gapless edge mode can be detected as a quantized Hall conductance. This was experimentally realized in HgCdTe heterostructures. The heavier element, Hg in HgTe, leads to a strong spin-orbit coupling. Depending on the thickness of HgTe, the band orders in the CdTe/HgTe quantum well can be either inverted or normal which shows corresponding quantized Hall conductance or non-quantized Hall conductance.⁷

Quantum anomalous Hall effect

The quantum anomalous Hall effect is a quantized Hall effect that occurs in a system without an external magnetic field. It requires the spontaneous magnetization of a ferromagnetic material even in the absence of a magnetic field. The quantum anomalous

Hall effect that occurs in magnetic topological insulators is the quantized version of the anomalous Hall effect. The Hall conductivity R_{xy} exhibits quantized values in multiples proportional to e^2/h , or the quantum of conductance. Similar to the QHE, the integer multiple is the Chern number. Unlike the QSHE, the spontaneous ferromagnetic (FM) magnetization favors one spin and results in a single spin polarized chiral edge state. Systems in which QAHE are observed are called quantum anomalous Hall insulators or Chern insulators.

Experimental realization of the QAHE was first observed in a thin films magnetic topological insulator: Cr-doped $(\text{Bi,Sb})_2\text{Te}_3$.⁸ With Fermi level tuning of a gate, anomalous Hall resistance reaches the predicted quantized value of h/e^2 at zero magnetic field, accompanied by a drop in longitudinal resistance. The longitudinal resistance goes to zero in a strong magnetic field, while the Hall resistance remains quantized.

1.2.4. 3D Topological electronic systems

So far, only 2D topological systems have been considered. This section expands those concepts to 3D topological materials and discusses the symmetry of each class.

Table 1. Classification of the topological electronic solid-state systems

System	Dimensions	TRS	Topo-invariant	Edge state
IQHE	2	No	Chern (n)	n gapless chiral edge states
QSHE – 2D TI	2	Yes	\mathbb{Z}_2 (ν)	ν # of pairs of gapless spin-locking helical edge state
QAHE	2	No	Chern	n gapless chiral edge states
3D TI	3	Yes	\mathbb{Z}_2	ν # of pairs of gapless spin-locking Dirac surface state
3D Magnetic TI	3	No	\mathbb{Z}_2 and Chern	Additional symmetry other than TRS can protect Dirac surface states. Some surface can have chiral edge states

Weyl semimetal	3	Yes or No	Protected Weyl pairs	Fermi arcs
----------------	---	-----------	----------------------	------------

Topological insulator: In a Z_2 topological insulator, the non-trivial band gap leads to gapless surface states at its boundaries as dictated by Kramer's theorem.¹³ First discovered in 2D systems, this concept was soon generalized to 3D topological insulators.¹⁴ Similar to the case of 2D topological insulators, their Hamiltonian is time-reversal symmetry invariant, which means global Chern number is zero, but Chern number for each spin is ± 1 . This can be achieved in small-gap semiconductors for which the spin-orbit coupling is large enough to induce band inversion and spin-momentum locking. Inherently, topological insulator protected by time reversal symmetry, with chiral edge states of spin polarized electron insulator has an insulating interior but conducting surface. Ordinary band insulators can also support conductive surface states. However, topological insulators possess surface states that are Dirac fermions propagating in opposite directions.

Small perturbations have no effect on the Z_2 index, and gapless conducting edge states are symmetry-protected. However, the edge states can be gapped out in the presence of magnetic impurities that break TRS.

Magnetic TI: Magnetic topological insulators are 3D magnetic materials with a non-trivial topological index that are protected by a symmetry other than time-reversal symmetry.¹⁵ It can also be seen as 3D version of the QAHE. In contrast to topological insulators in the previous section, introducing magnetism into topological insulators breaks time-reversal symmetry at certain surfaces. Surface states of an 3D MTI can be gapped if the topology-protecting symmetry is broken at that specific surface. In these 2D surfaces

with broken TRS, a non-zero Chern number can be defined and each gapped surface state exhibits a half-quantized anomalous Hall conductivity of $e^2/2h$ coming from the edge state of the surface. Additional symmetry on other surfaces can protect the gapless surface states in an MTI.

The only example of an intrinsic MTI realized today is MnBi_2Te_4 . In its ground state of magnetic ordering AFM-z, the equivalent time-reversal symmetry $S=T\tau$, which combines TR operation and the half-magnetic-lattice translation operation τ along the z axis, protects gapless Dirac cones on the $\langle 001 \rangle$ and $\langle 100 \rangle$ surfaces.¹⁶ The $\langle 0001 \rangle$ surfaces however are gapped under the Neel temperature due to the broken symmetry.¹⁷ Monolayer MBT is ferromagnetic and topologically trivial. Even-layer MBT is fully compensated antiferromagnetic with zero net magnetization. The Chern number is therefore zero. With the half-quantized edge state conductance of top and bottom surfaces of opposite signs, the Hall effect exhibits zero quantized conductance. Odd layer MBT has a nonzero Chern number and exhibits QAH effect.¹⁸ These striking phenomena were experimentally observed by Deng et al.¹⁹

Weyl semimetals

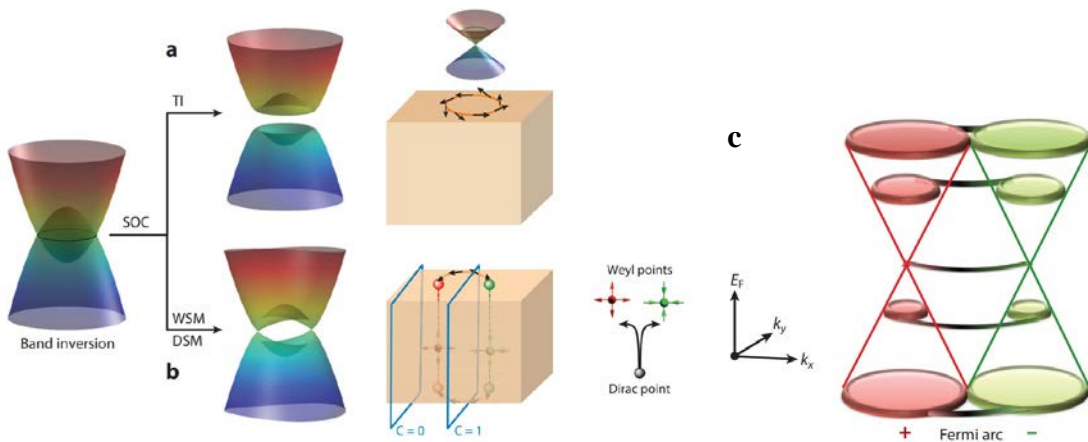


Figure 11. Band inversion in 3D topological materials can either form (a) TI or (b) Weyl semimetal with symmetry breaking. (c) Fermi arc surface states in a Weyl semimetal²⁰

A Weyl semimetal (WSM) is a topological material of different class than previously described systems with a unique band structure that is topologically protected. Low energy excitations of WSM are Weyl fermions.²¹ In a WSM's electronic band structure, Weyl fermions exist as low-energy excitations in which bands disperse linearly in three-dimensional (3D) momentum space through a pair of nodes called "Weyl points" (WPs) that are separated in momentum space. Weyl fermions have chiralities. In a WSM, the chirality of Weyl fermions at the WPs can be seen as topological charges. This leads to monopoles and anti-monopoles of Berry curvature in momentum space that act like a momentum space magnetic field. Compared to the Dirac fermions in graphene or on the surface of topological insulators (TIs), Weyl fermions in a WSM are the most robust electrons and do not depend on symmetries except the translation symmetry of the crystal lattice.

A Weyl semimetal either has TRS breaking or inversion symmetry (IS) breaking. The BZ has Weyl points which are monopoles of Berry curvature that comes in pairs. The existence of WPs and Fermi arc surface states is topologically protected and is its own topological invariant classification. It takes a large disturbance to bring the monopoles together to cancel them. Like TIs, WSMs also have topologically nontrivial surface states. The solutions to the Dirac equation of Weyl fermions on a lattice requires the existence of surface states called Fermi arcs. These arcs are discontinuous or disjointed segments of a two-dimensional Fermi contour, which are terminated onto the projections of the Weyl

fermion nodes on the surface. These so-called Fermi arcs are expected to induce fascinating transport properties and this subject is being heavily studied.

Consider a slice through the BZ between two Weyl points, the net Berry flux accumulated across the slice leads to a Chern insulator with a nonzero Chern number, which will carry chiral edge states. If the slice stays far away from the two Weyl points, the material is a trivial 2D insulator. Thus, the chiral edge states exist only between these two Weyl points.²⁰

The chiral anomaly

The chiral anomaly is an important phenomenon that occurs in WSM and will be the basis for arguments in Chapter 3. The chiral anomaly²² is produced in ideal WSMs by applying parallel electric and magnetic fields aligned along the direction of the WP separation, giving rise to charge pumping between the WPs of opposite Berry curvature.

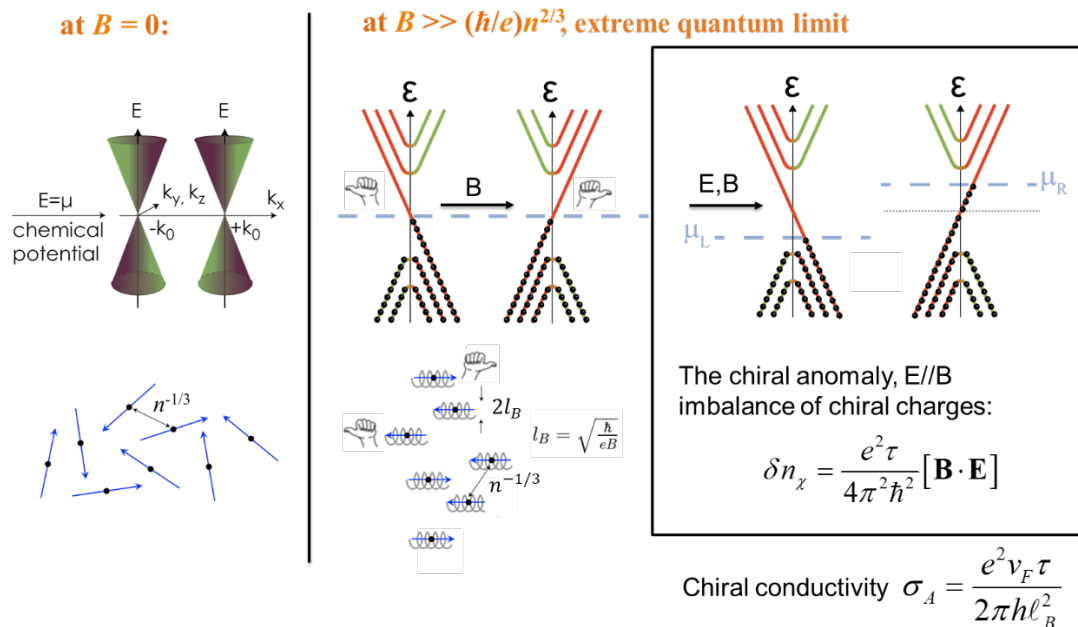


Figure 12. Evolution of Weyl bands in a magnetic field parallel to the separation of the WPs and the mechanism of the chiral anomaly

The remarkable evolution of the band structure into this point is explained as follow: (a) At zero field, we have the linear dispersing bands with crossing points WL and WR. In real space, the carrier has the same velocity but can move in an arbitrary trajectory. (b) By applying a field parallel to WL-WR, because of the Lorenz force, the magnetic field confines the electrons' motion in helixes. At an extreme field, the diameter of these helixes becomes so small the motion electrons can be considered 1D motion along the applied magnetic field. Now going back to momentum space, the electron bands are separated in Landau levels with the lowest energy LLs being two lines either slanted to the left or right. Carriers occupying states on these last LLs can only either move left or right. This bulk state at the fermi level resembles the surface state in the QHE. (c) Now we can apply an electric field in the same direction causing the local Fermi level to shift up on one WP and down on the other WP. This creates an imbalance of left movers and right movers. The excess of right movers is given by $\delta n_z = \frac{e^2 \tau}{4\pi^2 \hbar^2} [\mathbf{B} \cdot \mathbf{E}]$ which counts the number of states within the fermi level separation. The excess chiral charges move at the exact velocity dictated by the band structure and in the direction of the magnetic field. Their motion is said to be protected by topology. The anomalous current is proportional to the Fermi velocity v and the change in carrier density between W_L and W_R . The latter is proportional to the 2D density of state (DOS) $1/l_B^2$, where $l_B \equiv \sqrt{\hbar/eB}$ is the magnetic length and the electric field is $E = |\mathbf{E}|$. The longitudinal electrical conductivity along the direction z of an ideal WSM then is given by:²²

$$\sigma_{zz} = N_v \frac{e^2 v \tau}{4\pi \hbar l_B^2} \quad (1.8)$$

where τ^{-1} is the inter-WP scattering rate. The increase of σ_{zz} with H_z gives rise to the longitudinal negative magnetoresistance (MR),²³ which the scientific community has considered the experimental signature of the chiral anomaly.

1.3 Thermal conductivity in solids

In 1822, Fourier wrote in his book *Theorie analytique de la chaleur*: “Heat, like gravity, permeates all parts of the universe.” The reason is that everything carries thermal energy so thermal transport experiments are extremely useful when spin transport or charge transport is not accessible. For example, among elementary (quasi-)particles like electron, magnon and phonon, some has spin, some has charge but all of them carry thermal energy. However, heat transport can have contributions from many different (quasi-)particles and we usually can only measure a total effect of these contributions. It is therefore crucial to understand the behavior of each contribution in order to recognize and separate the contributions when possible.

$$\kappa = -\frac{q''}{\nabla T} = \kappa_{lattice} + \kappa_{electron} + \kappa_{magnon} + \dots \quad (1.9)$$

Assuming heat is conducted independently by electrons, magnons, and the lattice, thermal conductivity can be broken down as the sum of thermal conductivities contributed by electrons, magnons, and the lattice. There can be interactions between heat carriers, but the interactions are typically small and can be assumed negligible. When these interactions are large, special considerations should be taken in theoretical treatment and experiment design.

In the diffusive regime, thermal conductivity can be derived from the Boltzmann transport equation for each type of heat carrier or (quasi-)particle.

$$\kappa = \int \frac{d^3\mathbf{k}}{(2\pi)^3} \tau \mathbf{v} \cdot \mathbf{v} \left(-\frac{\partial f_0}{\partial \varepsilon} \right) \frac{(\varepsilon - \mu)^2}{T} \quad (1.10)$$

With transformation of variable we can also write:

$$\kappa = \int d\varepsilon D(\varepsilon) \tau v^2 \left(-\frac{\partial f_0}{\partial \varepsilon} \right) \frac{(\varepsilon - \mu)^2}{T} \quad (1.11)$$

Where $D(\varepsilon)$ is the density of states and f_0 is the statistical distribution function of each heat carrier. The thermal conductivity is an integral over the entire BZ. One can recognize the statistical distribution of the particle also comes into the equation as the energy derivative of the distribution function.

1.3.1 Phonon thermal conductivity

A phonon is a bosonic quasiparticle that is a quantum of lattice vibration. Like electron band structure, phonons in a 1D crystal have dispersion relation $\omega(k)$ that can be solved analytically in a simple model of masses and springs.

$$\omega_{\pm}^2 = K \left(\frac{1}{m_1} + \frac{1}{m_2} \right) \pm K \sqrt{\left(\frac{1}{m_1} + \frac{1}{m_2} \right)^2 - \frac{4\sin^2 \frac{ka}{2}}{m_1 m_2}} \quad (1.12)$$

The solution in Equation 1.12 can be plotted out as in the figure below.

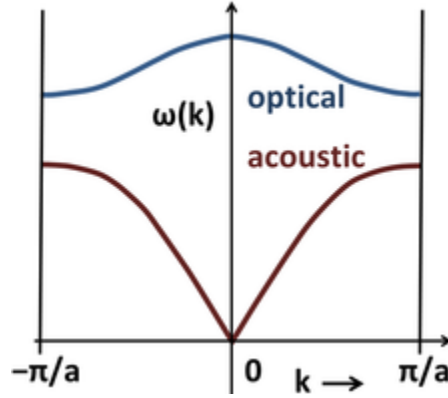


Figure 13. Schematic plot for solutions of the phonon dispersion in 1D

This solution yields two phonon branches. The acoustic mode is the branch resulting from the solution with the minus sign, while the optical mode is the branch resulting from the solution with the plus sign. The slope of the acoustic dispersion relation, $d\omega/dk$, determines the speed of propagation of an acoustic phonon, which is also the speed of sound in the lattice. The dispersion relation can be approximated as a linear dispersion at low values of k , corresponding to long wavelengths, and the speed of sound is approximately the slope of the acoustic branch at low k . Therefore, long-wavelength phonon packets can travel long distances across the lattice without scattering. They then become the dominant heat-carrying phonon.²⁴ Optical modes usually have much higher frequencies than acoustic phonons and have flat dispersions. This optical mode is therefore propagates in short distance and becomes the dominant scatterer.

Phonon thermal conductivity can be calculated from Equation 1.10 over all phonon modes to get:

$$\kappa_L = \int C_v(k)v(k)l(k)dk^3 \quad (1.13)$$

where $l(k)$ is the mean free path.

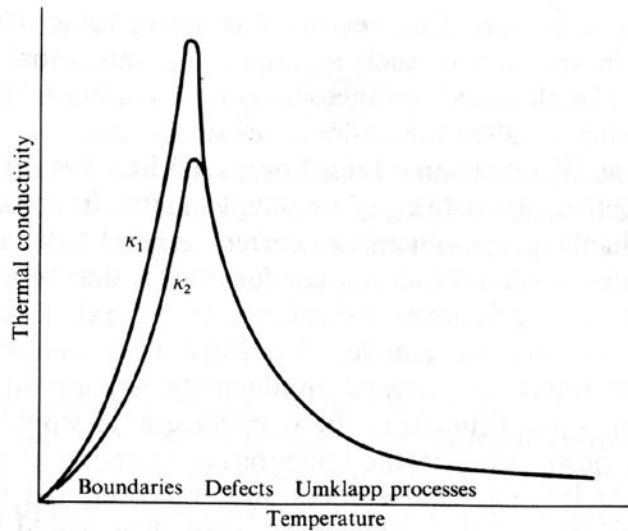


Figure 14. Phonon thermal conductivity of a non-metallic crystal.²⁵ Dominant phonon-scattering mechanisms are indicated along the abscissa. Upper curve is for a larger crystal

Figure 14 shows the classic phonon thermal conductivity curve.²⁵ At low temperature, the Boltzmann transport integral is deduced to $\kappa = \frac{1}{3}Cvl$, where C is the volumetric specific heat, v is the group velocity, and l is the mean free path. At low temperature, the mean free path is assumed to be the size of the sample, which is a constant, also called the Casimir regime. For phonons, acoustic phonons dominate at low temperature so the velocity is also a constant. Therefore, at low temperature, the phonon thermal conductivity is directly proportional to the specific heat, which follows a T^3 law. Since the mean free path is only limited by the sample size, the peak of thermal conductivity of a larger sample is higher at lower temperature. At high temperature, phonon-phonon scattering dominates. There are two types of processes: normal and Umklapp. Normal processes transfer heat and conserve momentum; they are additive and

do not increase a crystal's thermal resistance. Umklapp processes however are resistive and doesn't conserve momentum as the resultant momentum is folded back to the first BZ.

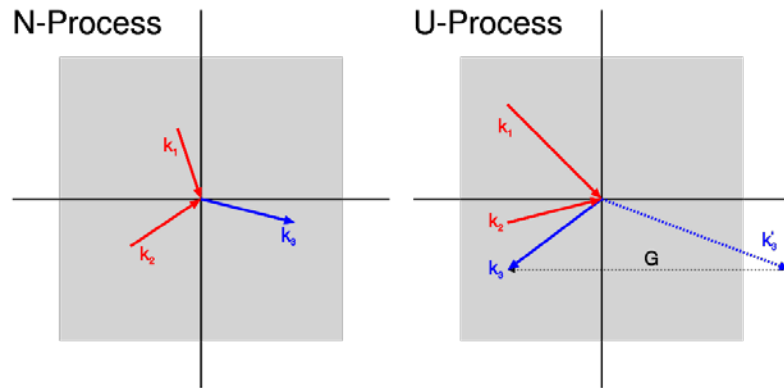


Figure 15. Normal phonon-phonon scattering process and Umklapp scattering process²⁶

Umklapp scattering becomes a dominant process at high temperature, as high as $1/2$ the Debye temperature Θ . The scattering time now becomes strongly temperature dependent and proportional to the number of phonons, following Bose-Einstein statistic. The scattering time is proportional to $\exp(\Theta/T)$, giving phonon thermal conductivity κ_L a T dependency of $\exp(-\Theta/T)$. In the limit of high temperature, the temperature dependency of the number of phonons reduces to a T^3 dependency. The region in which the above 2 regimes meet is where the phonon thermal conductivity is maximum; the peak temperature is typically between $1/10$ to $1/100$ of Θ . In this region, the thermal conductivity is most sensitive to defect scattering. As the number of defects in the crystal increases, the $\kappa_L \sim \exp(-\Theta/T)$ regime and the $\kappa_L \sim T^3$ regime both smear out and the maximum gets lower and flatter.

1.3.2 Electronic thermal conductivity

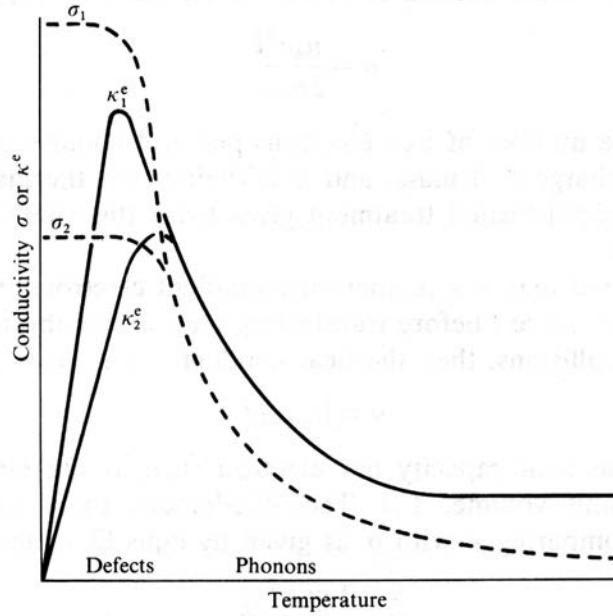


Figure 16. Electrical conductivity and electronic thermal conductivity of a metal as a function of temperature.²⁵ The dominant electron scattering mechanism is indicated along the abscissa. The higher curves are for more perfect samples.

In the free electron gas picture where each electron carries an electric charge e and quantity of heat $k_B T$, in the absence of all interactions and the scattering is elastic, kinetic theory of gases gives $\kappa = \frac{1}{3} c_v m n l \langle v \rangle$ where $c_v = 3 \frac{k_B}{m}$ is the Dulong–Petit specific heat, n is electron density, l is the mean free path and $\langle v \rangle = \sqrt{\frac{8k_B T}{\pi m}} = \sqrt{\frac{8}{3\pi}} v_{rms}$ is the group velocity of electrons. From Drude model, the conductivity is $\sigma = \frac{ne^2\tau}{m} = \frac{ne^2 l}{m \langle v \rangle}$. Therefore, $\frac{\kappa}{\sigma} = \frac{c_v m^2 \langle v \rangle^2}{3e^2} = \frac{8}{\pi} \frac{k_B^2 T}{e^2} = LT$ which is the classical derivation of the Wiedemann–Franz law with L being the Lorenz ratio. However, the Lorenz ratio of $L=8/\pi \sim 2.55$ from this derivation does not accurately predict the correct experimental values. The Lorenz ratio

is then corrected to $\frac{\pi^2}{3} \approx 3.29$ using the Sommerfeld method, which takes quantum effects into account. This value agrees very well with experimental values.

In metals, the electrical conductivity is governed by the Bloch-Gruneisen law:²⁵

$$\rho(T) = A \left(\frac{T}{\Theta_R} \right)^n \int_0^{\Theta_R/T} \frac{x^n}{(e^x - 1)(1 - e^{-x})} dx \quad (1.14)$$

At low temperature, the electron concentration is constant. Defect scattering limits the mean free path to a constant. The electrical conductivity is constant and simply limited by the defect level of the crystal so the electronic thermal conductivity follows a $\kappa_e \sim T^1$ law.

In the high temperature regime ($T > \Theta$), the electron-acoustic phonon interactions dominate. The highest energy phonons are the phonons with the k vector as large as the size of the BZ which is the same k vector that the electrons at the Fermi level have. Electron-acoustic phonon scattering changes the momentum of the electron by a large angle that is temperature independent. In this regime, the number of phonon modes is fixed; thus, the number of phonons is simply proportion to the temperature. Therefore, the scattering rate is proportional to T and electrical conductivity is proportional to T^{-1} , leading to a $\kappa_e \sim T^0$ law

In the intermediate regime ($T < \Theta$), phonons have momenta that are smaller than the electrons at the Fermi level, so electron-phonon scattering is small angle scattering. The number of phonon modes and the population of phonons in each mode are both temperature dependent. Combining these effects, the temperature dependence of electrical conductivity in this regime has a T^{-5} dependency. In this intermediate regime, if the scattering were elastic, WFL would predict a T^{-4} dependence of the electronic thermal conductivity;

however, scattering becomes inelastic in this regime which also makes the Lorenz ratio vary.

1.3.3. Spin thermal transport and magnetic ordering

At a finite temperature, localized spins develop a precession with a cone angle normal to the direction of magnetization. The propagation of this cone angle through the solid is known as a magnon. Magnons are bosonic quasiparticles which follow a wave equation similar to that of phonons. In analogy, the vibrational displacement of the lattice is propagated in phonons, while the precession cone angle is propagated in magnons.

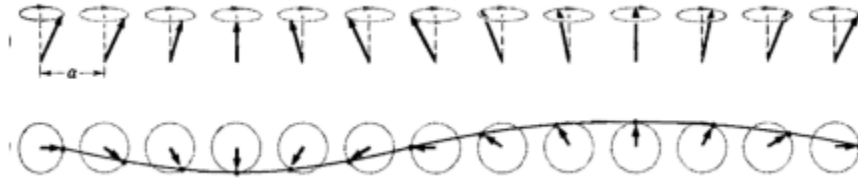


Figure 17. Schematic illustration of a magnon or spin wave²⁶

For an antiferromagnetic (AFM) ordering, the magnon dispersion relation is:²⁷

$$\hbar\omega = \hbar\omega_{max}|\sin(ka)| \quad (1.15)$$

The Taylor expansion at low energy gives:

$$\hbar\omega = \hbar\omega_{max}ka \quad (1.16)$$

Magnetic anisotropy adds a Zeeman term, which manifests as a small energy gap at the zone center. For ferromagnetic (FM) magnons, for simplicity, we consider a one-dimensional dispersion relation:

$$\hbar\omega = 4JS(1 - \cos ka) \quad (1.17)$$

With small k , Taylor expansion of Equation 1.17 results in a parabolic dispersion, $\hbar\omega \cong (2JSa^2)k^2$, which is more commonly written as $\hbar\omega \cong Da^2k^2$, where D is the magnon stiffness. Surprisingly, FM magnon dispersions at small k resemble the dispersion of electrons near the band edge. When we apply an external magnetic field B_{ext} , a Zeeman energy $g\mu_B B_{ext}$ is added to the magnon dispersion, which opens a gap. The gap size grows linearly with magnetic field. If we figure in magnetic anisotropy, the anisotropy energy (i.e., the energy gain that this alignment gives to the magnetic system) can be expressed in terms of an anisotropy field B_a by writing it as a Zeeman energy $g\mu_B B_a$. In turn, B_a then can be added to the external field B_{ext} to form an “effective” field B_{eff} . The final magnon dispersion for FMs is then:

$$\hbar\omega = g\mu_B B_{eff} + Da^2k^2 \quad (1.18)$$

Like phonons, magnons contribute to both specific heat and thermal conductivity.²⁸ Although the magnonic thermal conductivity can add to the total thermal conductivity, magnons can also have add negative contributions to the lattice thermal conductivity by scattering into phonons.

1.3.4 Techniques to separate common contributions of thermal conductivity

Separate lattice thermal conductivity: In semiconductors or semimetals, separation of contributions from electron and phonon from the total thermal conductivity can often be done by using magneto resistivity measurements. Using Boltzmann transport equation with relaxation time approximation, we get:

$$\kappa_e(B) = \int \frac{d^3k}{(2\pi)^3} \tau v \cdot v \left(-\frac{\delta f_0}{\delta \varepsilon} \right) \frac{(\varepsilon - \mu)^2}{T} \frac{1}{1 + \mu^2 B^2} \quad (1.19)$$

or simply $\kappa_e(B) = \frac{\kappa_e(B=0)}{1+\mu^2 B^2}$, where μ is the electron mobility. This shows that the electronic thermal conductivity of a high mobility sample approaches zero in a large magnetic field. Since $\kappa_{total}(B) = \kappa_e(B) + \kappa_L(B)$ and $\kappa_e(B) \rightarrow 0$ as $\mu B \rightarrow \infty$, we have $\kappa_L = \kappa_{total}(B)$ as $\mu B \rightarrow \infty$. In other words, the lattice thermal conductivity is not sensitive to magnetic field; so, in high field, the total thermal conductivity asymptote is the lattice thermal conductivity value. The electronic thermal conductivity is then deduced simply by taking the subtraction of the total thermal conductivity at zero field to the lattice thermal conductivity. This is an established method that is commonly used in high mobility samples.²⁹

Separating electronic thermal conductivity: In many cases, calculating electronic thermal conductivity using WFL $\frac{\kappa}{\sigma} = \frac{c_v m^2 \langle v \rangle^2}{3e^2} = \frac{8}{\pi} \frac{k_B^2 T}{e^2}$ with free electron value of the Lorentz ratio can result in accurate values. However, prior knowledge of cases where WFL is violated is important in data analysis.

Typically, the Lorenz ratio deviates from the free electron value when the scattering is inelastic. The free electron gas value of the Lorenz ratio applies at low temperature and at high temperature, where large angle, elastic scattering dominates. In the intermediate regime where small angle scattering dominates, the Lorenz ratio can be as low as 40% of the free electron value. As a rule of thumb, the Lorenz ratio may vary from slightly above the free electron value to about half or one-third of the free electron value. The Lorenz ratio for semiconductors is dictated by the position of the chemical potential relative to the band gap. If the Fermi level is deep into the band or at high temperature, we approach the degenerate limit and the Lorenz ratio recovers to the free electron value. As the number of

carriers decrease and the fermi energy goes into the band gap, electrons are more sensitive to scattering mechanisms. Here, the energy dependence of the scattering time is

$$\tau = \tau_0 e^\lambda \quad (1.20)$$

where λ is the scattering exponent dictated by the scattering mechanism. The Lorenz ratio L therefore is proportional to $\lambda + \frac{5}{2}$. For example, $\lambda = 0$ in case of neutral impurity scattering and $\lambda = 3/2$ in case of ionized impurities scattering. The Lorenz ratio L is then calculated to be about 2 and 4 respectively, which is $\pm 25\%$ of the free electron value of 3.29. In summary, in both metals and semiconductors, the Lorenz ratio classically can vary above or below about a third of the free electron value due to scattering mechanisms.

Separate magnon thermal conductivity: With both being bosons, it is typically difficult to separate magnon thermal conductivity from phonon thermal conductivity. In ferromagnets, one technique to separate the two is to depopulate magnon bands by applying a magnetic field that opens a Zeeman-energy gap in the dispersion.

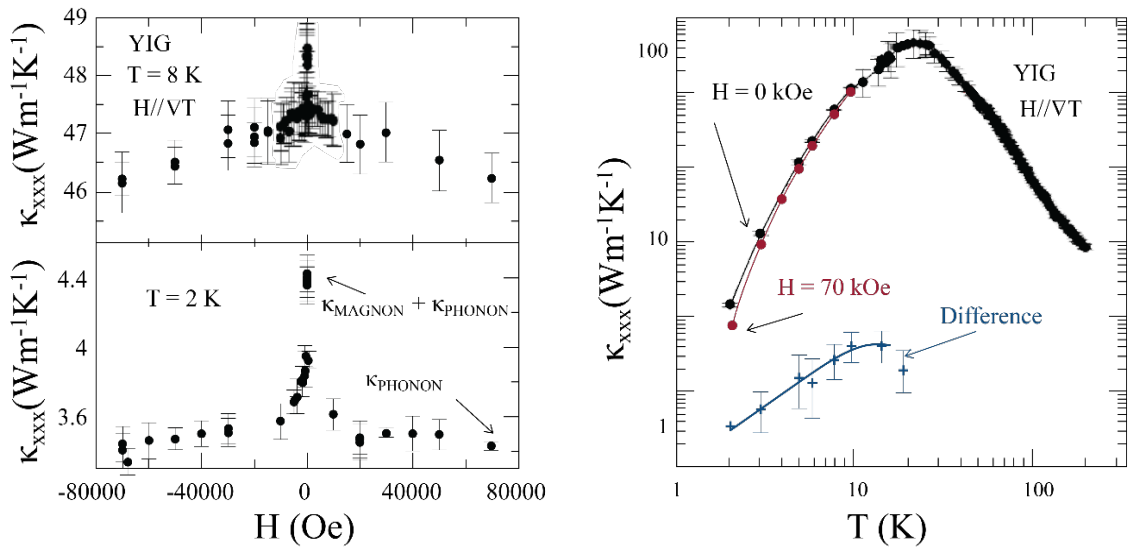


Figure 18. Magnon thermal conductivity of YIG, an electrically insulating FM, in an applied external magnetic field²⁸

The magnetic-field dependence of the total thermal conductivity is now $\kappa = \kappa_p + \kappa_m(B_{ext})$. The freeze-out of κ_m is visible in its field dependence, which shows a saturation at low temperature. Assuming that magnon-phonon interactions are negligible and phonons are insensitive to the magnetic field, magnon thermal conductivity can be deduced by subtracting $\kappa(7T)$ from $\kappa(0T)$,²⁸ as seen in **Figure 18**. Here, we can see that the temperature dependence of phonon and magnon thermal conductivity at low temperature follow different power laws, which is a result of the difference between phonon linear dispersion and FM magnon quadratic dispersion.

This technique only works in some cases. In several cases, phonons are scattered by magnons, and the scattering mechanisms can reduce the thermal conductance. When the phonon-magnon scattering is suppressed by the magnetic field, this effect is removed and the thermal conductivity can increase, as we will discuss in Chapter 5.

1.3.5. Thermal conduction by Bose-Einstein condensate

In many systems with bosonic quasiparticles such as phonons, magnons, and excitons (an electron-hole pair), it is often asked if the bosons will form a Bose-Einstein condensate (BEC) and further, if the BEC will participate in thermal transport. In Chapter 4, we will seek to answer these questions in a solid which is expected to host an exciton BEC. This section provides some background information on BECs and ways a BEC can participate in thermal transport.

An extended introduction to Bose-Einstein condensation can be found in Ref³⁰. In summary, a BEC is a collective quantum state of bosonic particles in which all the particles are at the same quantum state and have the same wave function. BECs thus carry no entropy and do not contribute to heat. However, there exists mechanisms which allow extremely good thermal transport in systems with BEC.

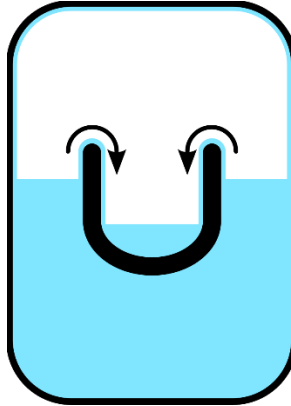


Figure 19. Creeping effect of Helium II superfluid.

Under certain circumstances, BECs exhibit a remarkable low-temperature phenomenon: superfluidity. This phenomenon was observed in the helium isotopes ^3He and ^4He at cryogenic temperatures. ^4He atoms are bosons, and although ^3He atoms are fermions, they can pair up with their counterpart of opposite spins to form boson-like states with zero net spin and thus, also undergo Bose condensation. In the superfluid state (also called Helium II), the individual particles don't interact with each other and there is only observable interaction between the collective of particles and the physical container. He II flows through capillaries as thin as 10^{-7} to 10^{-8} m; it has no viscosity.³¹ He II also exhibits a creeping effect. When given solid surfaces that extend across the liquid surfaces of He II in two separate containers, He II will creep along solid surfaces against gravity in order to

reach an equal level. He II's viscous-free flow allows for extremely efficient mass transfer while having no heat transfer. When measured between two moving discs, however, a viscosity comparable to that of gaseous helium was measured. The two-fluid model for He II is used to explain this. According to this model, liquid helium below the phase transition point contains both a fraction of He II atoms in a ground state, which is superfluid and flows with zero viscosity, and a fraction of He atoms in an excited state, which behaves more like a regular fluid.

The thermal conductivity of He II is rather extraordinary: the thermal conductivity is dependent on the temperature gradient, the vessel dimensions, and is greater than that of any other known substance, almost a thousand times larger than copper.³² This is because heat conduction in He II is governed by unique quantum mechanisms. When using the two-fluid model, entropy transfer is governed by equations that are similar to the wave equation that describe sound waves. The velocity of heat propagation called 'second sound' is given by³³

$$u_2 \approx \frac{TS^2}{C} \frac{\rho_s}{\rho_n} \nabla^2 T \quad (1.21)$$

where T is temperature, S is entropy, C is heat capacity, $\frac{\rho_s}{\rho_n}$ is the ratio of density between the superfluid portion and normal fluid portion. $\frac{\rho_s}{\rho_n}$ is a function of the order parameter and thus, is a function of temperature.

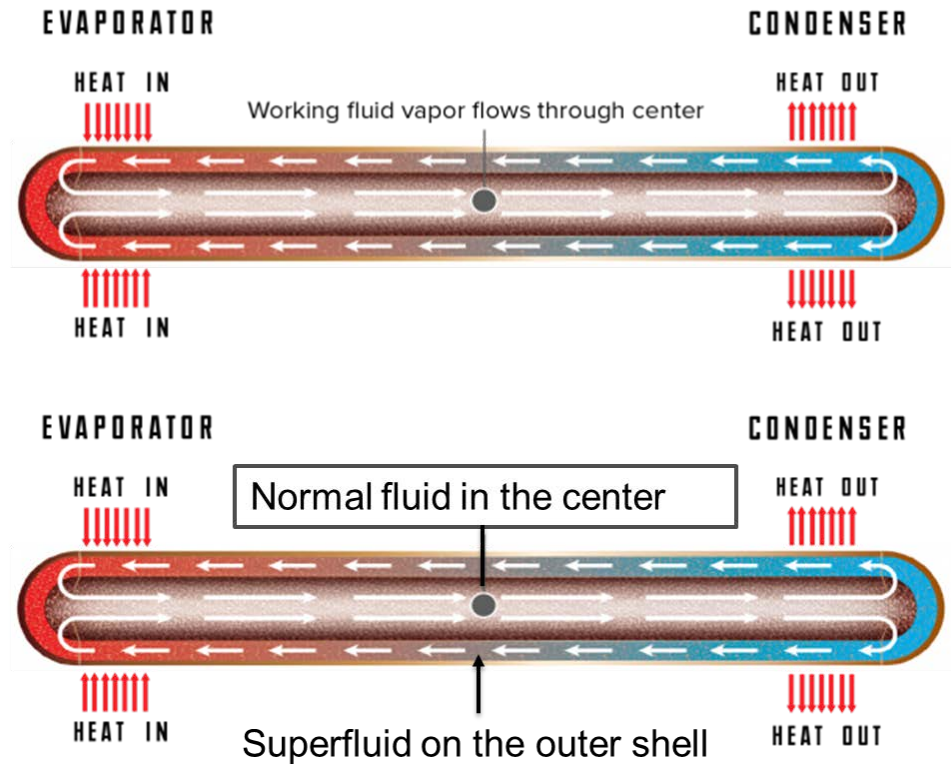


Figure 20. Heat conduction in heat pipe and hypothesis for heat-pipe heat and mass transfer mechanism in superfluid

Another very interesting hypothesis is that superfluid in two-fluid model can conduct heat with a heat pipe mechanism. In a heat pipe, a working fluid sticks to the edges of the walls with a wicking layer. There is a cavity in the middle of the pipe. When the heat pipe is placed between a heat load and heat sink, the working fluid will evaporate on the hot end, vapor will travel through the cavity from hot to cold then condense on the cold end. The wick absorbs the working fluid and transfers the working fluid from cold to hot using the cohesion-tension mechanism like how water is transported through plants by evaporation of water from the leaves. The heat transfer rate is very high with this mechanism. Like heat pipes, the effective thermal conductivity is dependent on the

temperature gradient and the length of the heat pipe, deviating from the Fourier law in solids. With superfluid, we can apply the same two-fluid model with normal fluid in the center carrying heat from hot to cold and the superfluid creeping along the wall from cold to hot to complete a continuous loop. Because of the creeping property of superfluid, the wick is no longer required. Experimentally in He II, under a critical heat current density and under a critical temperature, the temperature gradient is reported to deviate from Fourier law³⁴. The verification of Fourier law and the sample's length dependence of thermal conductivity will be ample experimental testing for the two-fluid heat conduction mechanism.

Chapter 2. Experimental methods

2.1. Voltage measurements and noises

The measurement of heat and charge transports revolves around 2 fundamental measurements: voltage measurement and temperature measurements. For measuring voltage, our lab uses Keithley 2182A nanovoltmeters. The voltage measurement can be found in the instrument's manual and other resources.

2.1.1. Voltage measurement noises

A voltage signal V_{signal} measured with instruments in the lab often has erroneous contributions other than the intrinsic voltage V_0 from external factors:³⁵

$$V_{signal}(t) = V_0 + V_{offset} + V_{white\ noise}(t) + V_{1/f\ noise}(t) \quad (2.1)$$

The offset voltage V_{offset} is a residual DC voltage given by the instrumentation and wirings. $V_{white\ noise}$ is the random fluctuation of the noise that has a Gaussian distribution and is often characterized as thermal noise or Johnson–Nyquist noise. Fundamentally, it is the electronic noise generated by the thermal agitation of the charge carriers (usually the electrons) inside an electrical conductor at equilibrium. This type of noise is approximately constant over the frequency spectrum. The power spectrum of white noise is independent of frequency up to a critical frequency where the noise power goes to zero. White noise can be filtered by simply averaging the signal over time.

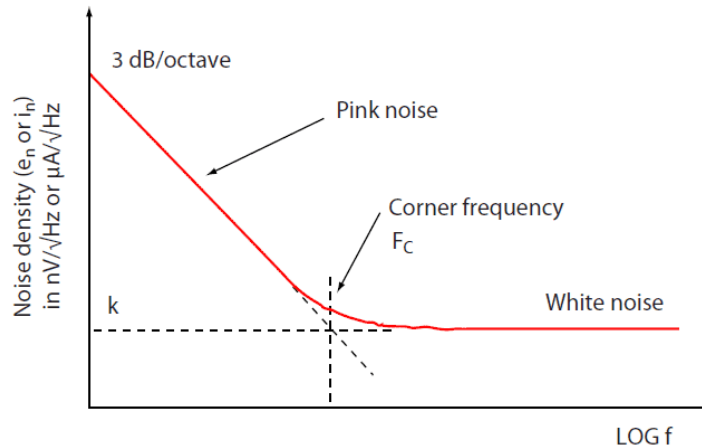


Figure 21. White noise is the flat part of a circuit's intrinsic noise spectrum on a noise power spectral density diagram. At lower operating frequencies, pink noise becomes more intense, emerging from white noise around the corner frequency and increasing at 3 dB/octave at lower and lower operating frequencies.

$V_{1/f \text{ noise}}$ is a component coming from the instruments that slowly drifts over time, also called pink noise or flicker noise. Noise spectrum studies have shown that this kind of noise has power density proportional to $1/f$. It is easily seen that high frequency measurements can help reduce the density of $1/f$ noise. However, it is not always possible to operate measuring instrument at higher frequencies than the corner frequency.

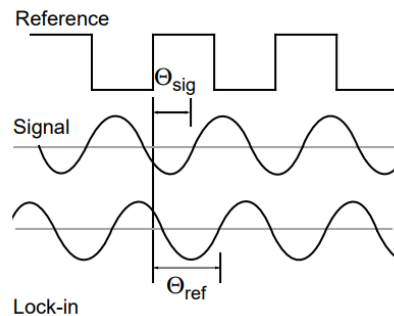


Figure 22. Illustration of lock-in phase detection method's reference, measured signal and generated lock-in signal. Credit: Stanford Research Systems

2.1.2 Lock-in measurement

A clever solution to treat time dependent noise is to use the lock-in phase detection method. The lock-in generate a reference lock-in voltage $V_L \sin(\omega_L t + \theta_{ref})$ at the same frequency and as the input current (or input voltage in voltage mode). The measured signal $V_{sig} \sin(\omega_r t + \theta_{sig})$ is then multiplied by the lock-in voltage to get V_{psd} (psd stands for Phase Sensitive Detection)

$$\begin{aligned} V_{psd} &= V_{sig} V_L \sin(\omega_r t + \theta_{sig}) \sin(\omega_L t + \theta_{ref}) \\ &= \frac{1}{2} V_{sig} V_L \cos([\omega_r - \omega_L]t + \theta_{sig} - \theta_{ref}) - \frac{1}{2} V_{sig} V_L \cos([\omega_r + \omega_L]t + \theta_{sig} + \theta_{ref}) \end{aligned} \quad (2.2)$$

In practice, there should be additional V_{psd} terms coming from frequency dependent noises with different frequencies ω_{noise} different from ω_L . For the moment, we consider only the signal with frequency ω_r , since $\omega_r = \omega_L$, the first term will be time independent while the second term is time dependent. For the noises, both the first and second terms are time dependent since $\omega_{noise} \neq \omega_L$. These time dependent terms can be filtered out with a low pass filter or software where the AC components are omitted, what we are left with is

$$V_{psd} = \frac{1}{2} V_{sig} V_L \cos(\theta_{sig} - \theta_{ref}) \quad (2.3)$$

From which we can calculate V_{signal} once the phases θ_{sig} and θ_{ref} are detected by the lock-in. The above description describes “in-phase lock-in” scheme. In systems where θ_{sig} and θ_{ref} are exactly 90 degrees out of phase, V_{psd} of “in-phase lock-in” will be zero.

Additional lock-in reference that is orthogonal to the reference can be used in this case to

$$\text{create a phase independent output } V_{psd,R} = \sqrt{V_{psd,in-phase}^2 + V_{psd,out-of-phase}^2}$$

2.2. Temperature measurements

2.2.1. Thermometer selection

The measurement of temperature has many nuances that special considerations should be taken in different contexts. There are different types of thermometers with different optimum range of temperatures and different complexity and robustness under external fields. In the scope of this dissertation, temperature in thermal experiments were measured with either Type T thermocouples or Cernox[®] thermistors. The table below shows key differences in performance of these 2 types of thermometers.

Table 2. Thermometer types comparison

	Thermocouples (TC)	Cernox[®]
Temperature Range	T>60K	T<60K with options available
Magnetic field induced error	<3% at 60K (7T field) for Cu-Constantan TC (see 2.2.3)	3% at 2K (8T) field (Lakeshore website)
Cost	Negligible	Hundreds of dollars for each cernox
Installation	Relatively easy	Sensors are tiny and fragile, requires intricate mounting techniques
Self-heating	Negligible	Excitation current dependent
Calibration	Tables readily available	In-situ calibration needed, heat cycling recommended

2.2.2 Working principle of thermocouple

The working principle of thermocouple involves the Seebeck effect: An electric field is developed when there is a temperature gradient in a material of conductor or semiconductor. The Seebeck coefficient S is given by: $S=dV/dT$

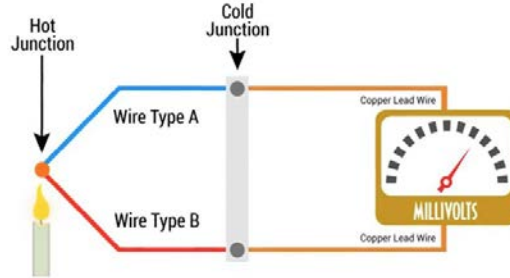


Figure 23. Construction of a thermocouple for temperature measurement

Two distinct types of metals are linked together to make two junctions in a thermocouple. These two materials are commonly made from opposite-sign Seebeck coefficient materials. The body whose temperature is to be measured is attached to the hot junction. The other ends are connected to a body with a known temperature that is colder.

To calculate actual temperatures T_h at the hot junction, we first obtain T_b as a base temperature, usually at the same temperature as the cryostat sample stage. T_b is measured using calibrated Cernox thermometer that comes with the cryostat and temperature controller. Assuming the Seebeck coefficient of thermocouple variation between T_h and T_c is negligible, T_h is calculated as

$$T_h = V_{Th} / S_{CuCon}(T_b) + T_b \quad (2.4)$$

Here, S_{CuCon} is Seebeck coefficient of copper-Constantan (a Ni-Cu alloy) thermocouple as a function of temperature. S_{CuCon} is taken from published reference table in NBS handbook.³⁶ In the next section, we detail how S_{CuCon} were measured in our lab in a calibration process. To ensure that all four ends of thermocouple wires that are attached to the base are at temperature T_b and that T_h is measured exactly on the sample, thermocouples are made of thin wires, $d_{TC}=0.0025$ mm. This diameter minimizes heat flow through the wires while still allows manageable handling of the thermocouples and maintains a low electrical resistance. Copper and constantan wires were spot-welded to form the hot junction then attached to the sample with a small dot of silver epoxy to ensure measurements of voltage and temperature differentials were at exactly same points on the sample. Estimated measurement error is at the order of 3% above liquid nitrogen temperature, mostly due to noise in the voltages. Estimated error for temperatures down to liquid helium temperature is detailed in the next section.

EMF integration method: The above section describes method of inferring T_h assuming a small temperature gradient T_h-T_c thus the change in Seebeck coefficient S_{CuCon} of the thermocouple between T_h and T_c is negligible. This is often applicable in experiments above liquid nitrogen temperature. It is customary that the temperature gradient is kept within 1-3K thus the variation in S_{CuCon} is within a few percent. A more accurate approach to calculate T_h without the assumption is to use the absolute electromotive force function of the thermocouple, defined as

$$E(T) = \int S(T)dT \tag{2.5}$$

The value of $E(T)$ can be numerically integrated from the calibrated $S(T)$ function. The voltage measured across the thermocouples can be written as

$$V_{TC} = \int_{T_b}^{T_h} S(T)dt = E(T_h) - E(T_b) \text{ thus } E(T_h) = V_{TC} + E(T_b) \quad (2.6)$$

From here, T_h can be found by solving for $E(T) = V_{TC} + E(T_b)$ numerically

2.2.3. Thermocouple calibration

The sensitivity of Cu-Constantan thermocouples used in thermal conductivity measurements of this work has been checked experimentally. The Seebeck coefficients of constituent 25 μm diameter copper and Constantan wires used to fabricate the thermocouples were measured as follows: A temperature gradient was created along the length of a slender piece of glass with one end bonded to a resistive heat source and one end bonded to a heat sink. At steady-state condition, the heat sink temperature was controlled by the temperature controller of Quantum Design PPMS, and the heat flux was constant. At two specific points on the glass, where the ends of the sample wires were welded, temperatures of these points were measured with cernox temperature sensors that were calibrated in the temperature and field range of the experiment by Quantum Design. The voltage between two ends of the sample wires were measured with a Keithley nanovoltmeter. The measurements were conducted at discrete temperature points between 5 K to 300 K, in sweeping-down magnetic field from maximum field of 7 T to minimum field of -7 T in Quantum Design PPMS. Controls software was programmed using LabVIEW.

We calculate the Seebeck coefficient of the sample wires using the following formulas:

$$S_{Cu} = \frac{V_{Cu}}{T_H - T_C} - S_M \quad (2.7)$$

$$S_{Co} = \frac{V_{Co}}{T_H - T_C} - S_M \quad (2.8)$$

where V_{Cu} and V_{Co} are the voltages measured between the two ends of sample wires, T_H and T_C are temperatures measured at the two ends of sample wires, and S_M is the Seebeck coefficient of the measuring circuit. Accordingly, the Seebeck coefficient of the Cu-Constantan couples was calculated using:

$$S_{TC} = S_{Cu} - S_{Co} = \left(\frac{V_{Cu}}{T_H - T_C} - S_M \right) - \left(\frac{V_{Co}}{T_H - T_C} - S_M \right) = \frac{V_{Cu}}{T_H - T_C} - \frac{V_{Co}}{T_H - T_C} \quad (2.9)$$

The resulting values are reported in **Table 3**.

Table 3. Results of Type T thermocouple calibration

T(K)	S_{TC} at zero field (V/K)	Max. deviation of S_{TC} in field (V/K)	Relative deviation of S_{TC} field (%)	S_{TC} from NBS125 (V/K)	Deviation of S_{TC} from NBS125 (%)
60	1.30E-05	1.33E-05	2.2	1.38E-05	-5.8
40	9.42E-06	1.02E-05	8.1	1.02E-05	-7.3
20	5.33E-06	5.83E-06	9.4	5.50E-06	-3.0
10	2.44E-06	2.62E-06	7.3	3.03E-06	-20

The calculated field dependence of Cu-Constantan thermocouples is the difference between columns 2 and 3, given in % in column 4. The total deviation from National Bureau of Standards (NBS) table 125 (data repeated in column 5) is given in column 6.³⁶

The absolute values of the error, the deviation from NBS reported in the last column, is below 6% down to 60. Above 60 K, the total error is 12%, but the relative error on the temperature dependence is below 6%. The relative error in the magnetic-field dependence is less than or equal to 2% down to 60 K, and less than 10% at 34 K.

2.2.4 Working principle of thermistors and thermistor resistance measurement

Thermistors are semiconductor-based temperature measurement devices. Because the resistance of a thermistor varies with temperature, the temperature of the object in thermal contact with the thermistor can be inferred by measuring resistance.

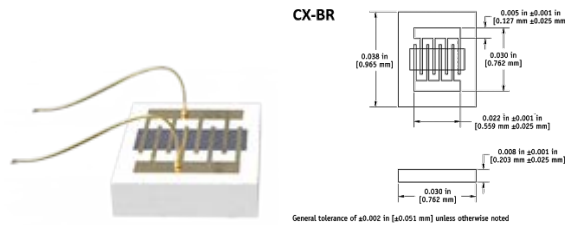


Figure 24. Lakeshore Cernox bare chip packaging and dimensions

Thermistors resistance measurement: To use thermistors, we need to measure their resistances. Due to limitation of the number of pins out on most cryostat, it is more practical to wire the thermistors in series. This way, the setup only needs to use 5 pins for 2 thermometers in quasi-1D thermal measurements and 1 additional pin for each additional thermistor. The wiring diagram is shown below.

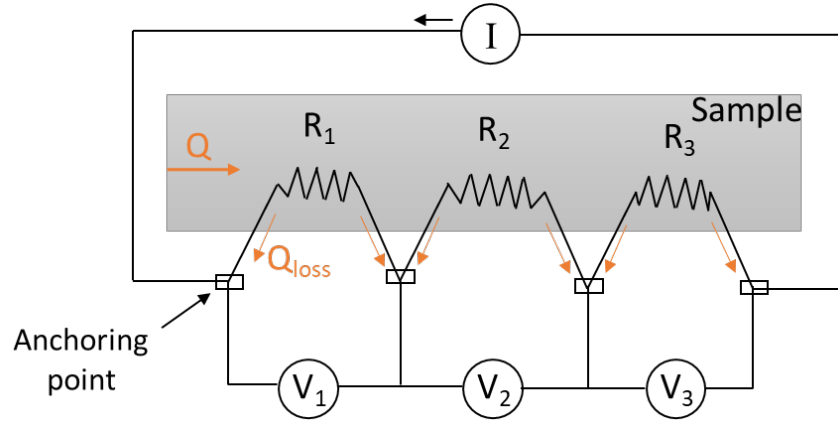


Figure 25. Wiring diagram for cernox resistance measurement. Resistances of cernox sensors are R_1 , R_2 and R_3

Note that the resistance measured is the total resistance of the thermistor and resistance of the wires from anchoring point to the thermistor, added by the contact resistance of between the wire and the thermistor. The later 2 resistances should be avoided since they add additional error with varying temperatures and magnetic field. It is recommended to use electrically conducting metal lead wires such as gold or copper to limit the contribution of wire resistance to less than an ohm at room temperature. Short wire or no wire at all (standard 4 leads measurement) is ideal in this regard but this can create another problem with heat loss, as will be discussed later. At cryogenic temperature, the wire resistance contribution would generally be negligible. To reduce contact resistance, it is recommended to attach the leads to the chip using Indium solder or hot-pressed gold contact from factory. For more detail, refer to Lakeshore Cernox Appendix C: Sensor Packaging and Installation.

DC resistance method: The DC method uses Ohm's law and measures the DC voltage drops across a thermistor. DC current is applied across the thermistor by a Keithley

6001 and voltages are measured by Keithley 2182A with 7002 switch box. Thus, the resistance can be calculated using Ohm's law:

$$R = \frac{V}{I} \quad (2.10)$$

AC resistance method: AC resistance bridges such as Lakeshore 370 use lock-in method and directly give the resistance as the output. When allowed, AC method is preferred over DC method since it is extremely sensitive to small signal that is sometimes too miniscule compared to noise. Thus, a smaller excitation current can be used to reduce self-heating of the sample. The disadvantage of AC measurement is the delay for the time dependence process of phase detection and converting the time domain signal to frequency domain. Therefore, AC measurement is less sensitive to signal that changes faster than its integration time. For example, it is generally not suitable for measurement in a sweeping magnetic field.

Self-heating consideration: Special care must be given to minimize the heat generation on the thermistors due to Joule heating. To be safe, excitation current should be chosen to be small enough so that the Joule heating power $P_J = I^2 R$ on each thermistor is in the order of nW.

2.2.5. Thermistor calibration.

Zero field measurement: For a thermistor, calibration is the process of generating an equation that relates the resistance to the temperature. The Steinhart-Hart Equation can be used to approximate the relationship between thermistor resistance and temperature.³⁷

$$T = \frac{1}{c_1 + c_2 \ln(R) + c_3 (\ln(R))^3} \quad (2.11)$$

By inverting both sides and adding a quadratic term we can transform the equation to a polynomial form

$$\frac{1}{T} = a_1 + a_2 \ln(R) + a_3 (\ln(R))^2 + a_4 (\ln(R))^3 \quad (2.12)$$

The values of the constants, a_1 , a_2 , a_3 and a_4 are determined in the calibration process. Calibration was done by measuring the resistance of cernox in-situ, meaning that the thermistor is mounted on the sample as it should be measured in the measurement and thus, the resistance should be identical in the actual measurement. The sample is mounted on the platform of the PPMS. The calibration program then varies the platform temperature, waits for temperature stabilization and measures the resistance. A table of temperature vs resistance is then constructed that allow calibration constants to be computed. To avoid divergence of $1/T$, T should be in Kelvin. Polynomial regression functions can be used to find the coefficients a_1 to a_4 , which can be done on any common program such as MathCad.

Calibration in a magnetic field: The same process can be repeated to generate a polynomial function that relates $1/T$ to $\ln(R)$ at each magnetic field that the measurement will be done at. Generally, magnetic field dependence of cernox sensor is extremely small and only becomes necessary for temperature below 10 K. The reported deviation in field ($dT/T(\%)$) of these sensor even at 2 K is less than 3% at 8 Tesla.

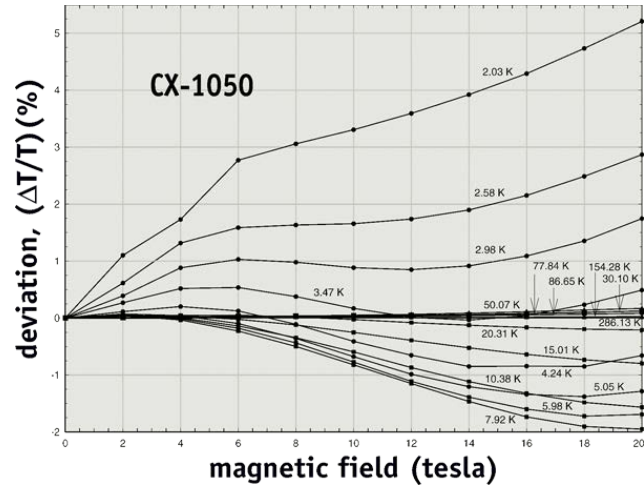


Figure 26. The reported result deviation in field $dT/T(\%)$ of CX-1050 sensor from Lakeshore website

2.3. Applications in heat and charge transport properties measurements

2.3.1 Hall and resistivity measurement

The isothermal electrical resistivity and Hall resistivity were measured using a typical Hall bar-geometry setup (5-point probe method) with the magnetic field perpendicular to the electric field. The sample was put on an electrically insulating but thermally conducting sapphire substrate (see **Figure 27**). This was done to eliminate the effect of secondary Seebeck and Nernst voltage and ensure isothermal measurement conditions by keeping the temperature gradient along the length of the sample and across the sides of the sample to a minimum. Electrical probing contacts were constructed with copper wires that were spot welded to the sample. When necessary, silver epoxy was used to reinforce the contact mechanically. A brass or copper current spreader was used to make electrical current contacts. The current spreader is electrically contacted to the sample with a thin layer of silver epoxy to create an even distribution of current lines.

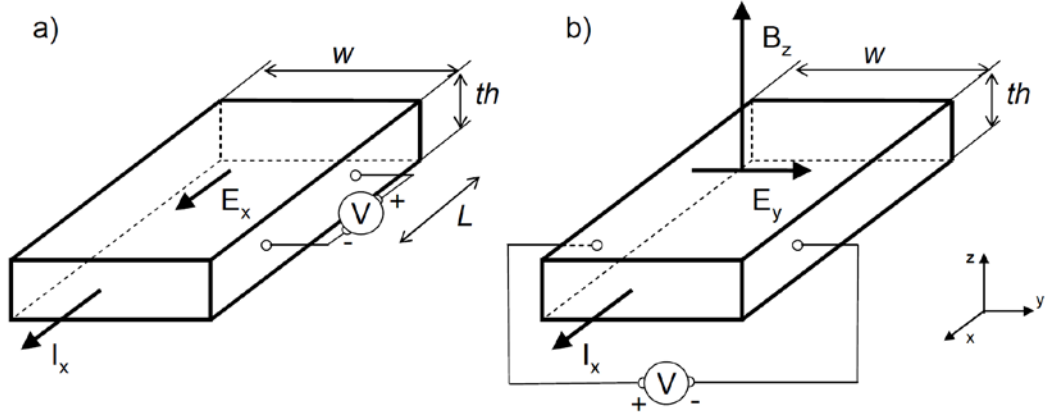


Figure 27. Measurement configurations and sign convention for Hall and resistivity measurements

Electrical conductivity is defined as a tensor, describing proportionality of electron flux j to the electric field E . For a Hall bar geometry, the conductivity tensor can be considered 2D

$$\begin{pmatrix} j_x \\ j_y \end{pmatrix} = \begin{pmatrix} \sigma_{xx} & \sigma_{xy} \\ \sigma_{yx} & \sigma_{yy} \end{pmatrix} \begin{pmatrix} E_x \\ E_y \end{pmatrix} \quad (2.13)$$

we can then define $\sigma = \begin{pmatrix} \sigma_{xx} & \sigma_{xy} \\ \sigma_{yx} & \sigma_{yy} \end{pmatrix}$. In our measurement, we measure electrical resistivity and the Hall resistivity which can be written as:

$$\rho_{xx} = \frac{E_x}{j_x} = \frac{V_x}{I_x} \cdot \frac{w \cdot th}{L} = R_{xx} \cdot \frac{w \cdot th}{L}; \quad \rho_{xy} = \frac{E_y}{j_x} = \frac{V_y}{I_x} \cdot \frac{w \cdot th}{w} = R_{xy} \cdot th \quad (2.14)$$

Either V_x , V_y , I_x can be obtained from DC method or R_{xx} and R_{xy} can be obtained from AC measurement. To find conductivities, we apply a tensor inversion $\sigma = \rho^{-1}$

The low-field (i.e., $H < 5$ mT at 10 K and < 50 mT at 100 K) Hall coefficients R_H were measured and converted into a carrier concentration via the relation:

$$R_H = -\frac{1}{nq} \quad (2.15)$$

The carrier concentration is therefore $n = -\frac{1}{qR_H}$. The low-field mobility then was derived from the resistivity and the carrier concentration. The carrier mobility is obtained as follows: $\mu_n = -\sigma R_H$

The error in the Hall and resistivity measurements in the transverse magnetic-field setup comes from the geometrical effect. If the sample is short with L/W ratio of approximately 2, at higher field (i.e. $\mu B > 1$), the effect of distorted current lines could lead to an underestimation of Hall resistivity and resistivity magnitude by as much as 5 to 10%, as reported in literature.³⁸

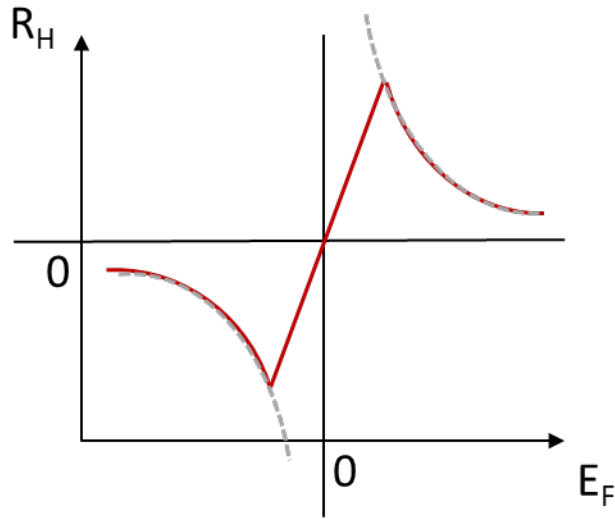


Figure 28. R_H as a function of Fermi level E_F

Note that the Hall measurement measures majority carrier concentration. A special caution when measuring carrier concentration using R_H is when Fermi level near the mid-

gap in semiconductors or near compensated point in semimetals. The method we use assumes R_H is a $1/n$ function as shown in dotted lines in **Figure 28** which diverges at charge neutrality point. In reality, as Fermi level moves to charge neutrality point, R_H will go through zero as shown in the red line, since there are as many electrons as holes deflected to one side of the sample in magnetic field. The relation $R_H \sim 1/n$ is therefore not applicable when E_F is near zero. To recognize this scenario, one should keep in mind that when E_F is near zero, the Hall coefficient R_H would vary greatly with temperature and magnetic field and potentially switch signs, making the Hall resistivity non-linear. Therefore, if measurement of R_H shows non-linear in field, it is an indication of Fermi level near zero and the method for getting majority carrier concentration is no longer applicable.

2.3.2 Longitudinal Magneto Resistance

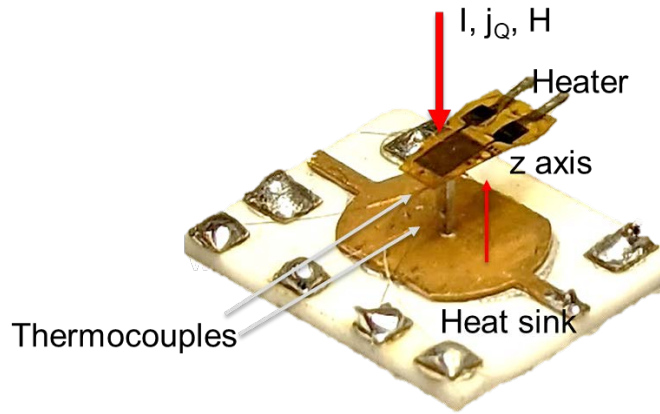


Figure 29. A device constructed for a longitudinal magneto resistance and longitudinal magneto thermal conductivity

Longitudinal magneto resistivity was measured on samples using standard 4 probes set up. The direction of the magnetic field was parallel to the electric field. The sample stood vertically on a current spreader which was attached to an alumina base plate. The

sample was stabilized thermally at each temperature point for 30 minutes before each measurement started. Electrical measurements were conducted with direct current and sweeping-down magnetic field from a maximum field of 9 T to a minimum field of -9 T in a Quantum Design Physical Property Measurement System with a sweeping rate of 5 mT/s. In the device in **Figure 29**, the sample was mounted in such a way that both electrical and thermal measurements were performed in 1 experiment to avoid any effect of dislocations due to thermal cycling. Magneto resistance is defined as the relative difference of resistance compared to the resistance at zero field.

$$MR(\%) = \frac{R(B) - R(0)}{R(0)} * 100\% \quad (2.16)$$

A negative LMR is deemed a signature transport property of the chiral anomaly in Weyl semimetal. However, as discussed in next section, there are other extrinsic effects that can create faulty LMR result in an LMR measurement.

Extrinsic effects in LMR measurement: Longitudinal magnetoresistance (MR) measurements on high mobility semiconductors, can contain extrinsic signals unless extreme care is taken in sample preparation, dimensions, and alignment. The extrinsic signals can be generated in three ways: current jetting³⁹, the galvanomagnetomorphic effect,⁴⁰⁻⁴² and the geometrical MR.⁴³ Current jetting and the galvanomagnetomorphic effect give rise to an extrinsic negative longitudinal MR, the same sign as would the chiral anomaly. The galvanomagnetomorphic effect is not likely to occur in our samples, first, because their dimensions are orders of magnitude larger than the Larmor radius of the electrons in fields above 1 T, and second, because the data show the transport to be robust

to defect scattering, so that it is likely also robust to surface scattering. Current jetting is minimized and checked for by keeping sample dimensions small and placing the voltage contacts at different locations, looking for variations.

The geometrical MR gives rise to an extrinsic positive MR, and arises either when the sample surface is not smooth,⁴⁴ or when the field is slightly misaligned with respect to the current flow lines in the sample, as can occur during sample mounting. This is the main cause of difficulties in the present measurements of longitudinal magnetoresistance. The positive geometrical magnetoresistance is³⁸ $\rho_{Geom} = \rho(1 + A\mu_{mo}^2 B_{\perp}^2)$ and the relative correction for the positive geometrical MR is:

$$\Delta\rho_{Geom}/\rho = A\mu_{mo}^2 B_{\perp}^2 \quad (2.17)$$

where $B_{\perp} = \mu_0 H_{\perp}$ is the magnetic induction in the direction perpendicular to the current and μ_{mo} the mobility and the pre-factor A depends on the ratio between the length of the sample along the current flow direction to its width. The pre-factor varies from $A=1$ for a Corbino disk geometry, to $A=0$ for an infinitely long and thin sample. For the geometries of concern here, A is of the order of $A=0.25$ for a square sample and $A=0.05$ for a length-to-width ratio near 10:1.^{38,43} In longitudinal measurements \vec{B} is in theory parallel to the current direction, but in practice field misalignment by an angle θ generates a transverse component $B_{\perp} = |\vec{B}| \sin \theta$ to the magnetic field vis-à-vis the current lines, so that the Lorenz force distorts them. The relative error bar on longitudinal MR measurements is

$$\Delta\rho_{Geom}/\rho = A\mu_{mo}^2 B^2 \sin^2(\theta) \quad (2.18)$$

In some samples, this error is the main source of error in the electrical resistivity measurements. To overcome these challenges, improvements to sample mount methods was developed to avoid the extrinsic effects. First of all, the crystal was shaped in a long needle shape with L/W ratio approach a factor of 10. This is to avoid current line distortion. Secondly, current spreaders are mounted on both ends of the sample, with the voltage probing wires along the spine of the sample to avoid current jetting. Last but not least, it is crucial to align the crystal with the base with best precision. A set precision machined scaffold was fabricated to make sure the sample is perpendicular to the base and is parallel to the field. A goniometer (Wixey Model WT41) was used to measure the angle between the long direction of the sample and the base of the heat sink to calculate the error bar. The alignment error was limited to 0.1 deg, which limit error of positive MR to 5% given by Equation 2.18.

2.3.4 Thermoelectric coefficient measurements

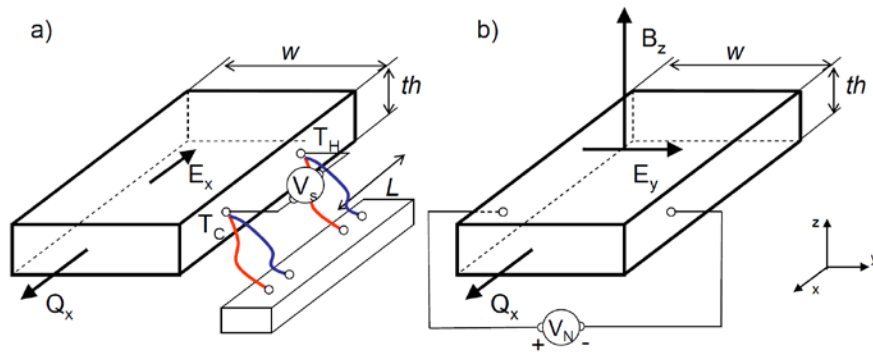


Figure 30. Measurement configuration and sign convention for Seebeck and Nernst coefficient measurement

Seebeck coefficient: Seebeck coefficient relates the developed electric field when temperature gradient is established in a material, $E = -S\Delta T$. Consider the electron and hole

gas in a temperature gradient, electrons and holes are diffused in the sample from hot to cold, equilibrium is established by the opposing electric field E_x . **Figure 30a** above depicts a geometry in which heat flux is in the x-direction and it establishes the opposing electric field in same direction. This is a one-dimensional case in which the Seebeck coefficient is defined as a constant:

$$S = -\frac{E_x}{dT/dx} = \frac{-dV/dx}{dT/dx} = \frac{V_s}{T_H - T_C} \quad (2.19)$$

T_H and T_C are temperatures measured at two points along the temperature gradient created by heating one end of the sample with a resistive heater and thermally anchor the other end with the sample stage of the cryostat. V_s is the voltage between two points at which these temperatures are measured. Note that the measured voltage has a thermoelectric contribution of the measuring circuit which is made of copper (See thermocouple calibration 2.2.3). To correct for this,

$$S_{sample} = \frac{V_{measured}}{T_H - T_C} - S_{Cu} \quad (2.20)$$

From this expression, we see that measurement of the Seebeck coefficient does not depend on the geometry of a sample. Since holes and electrons are both diffused in the same direction, the Seebeck coefficient measures the effect of the majority carrier.

Nernst coefficient: The Nernst coefficient relates the developed transverse electric field observed when heat flux passes through a material which is in a magnetic field, B . The measurement assumes a one-dimensional heat flux going through the sample with magnetic field perpendicular to the sample as shown in **Figure 30b**. Electrons and holes are diffused

from hot end to cold end. Under the influence of the Lorentz force like in the case of Hall effect, electrons and holes are deflected to opposite sides of the sample. Equilibrium is established by the electric field E_y which can be calculated by measuring Nernst voltage, V_N . In this configuration Nernst coefficient N is

$$E_y = N \cdot B \frac{dT}{dx} \quad (2.21)$$

Unlike the Seebeck coefficient, to calculate N , we need to determine sample geometry.

$$N = \frac{E_y}{B_z \frac{dT}{dx}} = \frac{dV/dy}{B_z \frac{dT}{dx}} = \frac{V_N}{B_z(T_C - T_H)} \frac{L}{w} \quad (2.22)$$

In 2 carrier systems, the Nernst effect measure combined effect of both carriers thus it is large in 2 carrier systems. Origin of errors is again mainly in measuring sample's geometry.

For S and N , errors are estimated to 7%.

2.3.4 Thermal Hall and Thermal conductivity

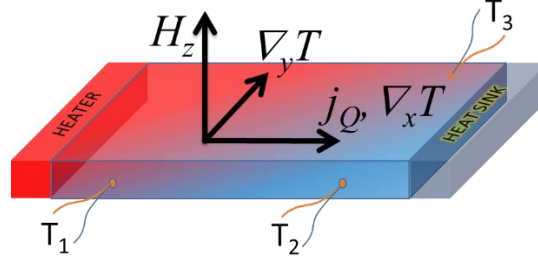


Figure 31. Measurement configuration for thermal Hall conductivity and Thermal conductivity

The thermal conductivity measurement uses plate-like sample with cross-sectional area A and distances l_{xx} and l_{xy} (when thermal Hall is also measured) between temperature measurement points along the x and y direction. The configuration is shown in **Figure 31**. The magnetic field when applied is in z direction perpendicular to the sample plane. The thermal conductivity tensor $\bar{\kappa}$ is then defined as the tensor correlating the applied heat current J_Q across the sample along the x direction to the resultant temperature gradient ∇T :

$$J_Q = -\bar{\kappa} \cdot \nabla T = -\begin{pmatrix} \kappa_{xx} & \kappa_{xy} \\ \kappa_{yx} & \kappa_{yy} \end{pmatrix} \cdot \nabla T \quad (2.23)$$

The thermal resistivity tensor is defined as the inverse, $\bar{w} = \bar{\kappa}^{-1}$. The heat current can be calculated as $J_Q = Q/A$ where Q is the heater power obtained from Joule heating power of the resistive heater. The thermal gradients can be calculated from the temperature differences δT_{ij} such that $\delta T_{xx} = (-\partial_x T) \cdot l_{xx}$ and $\delta T_{yx} = (-\partial_y T) \cdot l_{xy}$. The temperature differences $\partial_x T$ and $\partial_y T$ are measured using thermometers such as cernox sensor or thermocouples as discussed previously. The thermal resistivities are the quantities that are actually measured and are calculated as follow.

$$w_{xx} = \frac{\delta T_{xx}}{l_{xx}Q} \quad (2.24)$$

$$w_{yx} = \frac{\delta T_{yx}}{l_{yx}Q} \quad (2.25)$$

The Onsager's relations demand $w_{xy} = -w_{yx}$ (anti-symmetric in field) and we may relate the conductivities to the experimentally measured w_{ij} as follows⁵

$$\kappa_{xx} = \frac{w_{yy}}{w_{xx}w_{yy} + w_{xy}^2} \quad (2.26)$$

$$\kappa_{xy} = \frac{w_{yx}}{w_{xx}w_{yy} + w_{xy}^2} \quad (2.27)$$

For many cases where only longitudinal thermal conductivity is the property of interest, the experiment is simplified to a quasi-1D heat flow problem where we only need to measure w_{xx} with 2 thermometers along the temperature gradient. With a long and thin sample, w_{xy} becomes negligible and thermal conductivity can be found by simply invert w_{xx} : $\kappa_{xx} = \frac{1}{w_{xx}}$. With this setup, we can also apply the field in arbitrary direction to measure field dependence of thermal conductivity.

Heat loss prevention and treatment: Since the thermal conductivity measurement assume a known Q and that the heat flow through the sample, special consideration about heat loss should be given when measuring samples with high thermal resistance and at low temperature. Like in electrical circuit where current will dominantly flow through the lower resistance branch out of a node. Thermal resistance of a sample is given by

$$R = \frac{L}{A\kappa} \quad (2.28)$$

With A the cross-sectional area, L the length of the sample and κ the sample's thermal conductivity. For long, or thin, or low thermal conductivity, the thermal resistance can be large. Once this thermal resistance becomes large enough and comparable to the thermal resistance of the contact wires, we will have large conduction heat loss from the wires (**Figure 25**). Although we have purposefully chosen small gauge wires to geometrically limit their thermal conductance. It can be easily seen in **Figure 32** that the problem exacerbated at low temperatures where thermal conductivity of copper, a common contact wire, becomes extremely large.

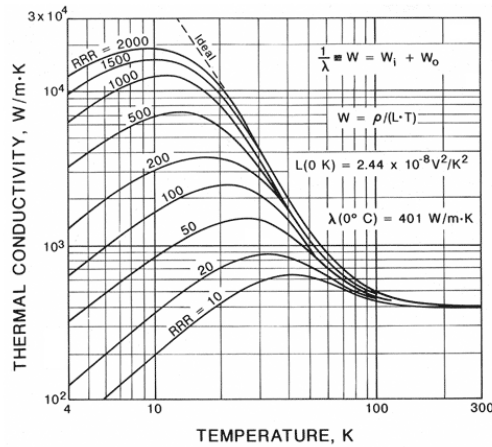


Figure 32. Thermal conductivity of copper

It is therefore customary to calculate the thermal conductance of the wires and estimate that for the sample to compare. When the wire conductance becomes an order of magnitude as large as the sample thermal conductance, it is recommended to use smaller wire gauge or longer contacting wires.

For the cernox sensor circuit, insulating the gold/copper leads wires by adding manganin wires between the gold/copper wires and thermal anchoring point proved to be

effective. The modified circuit (**Figure 33**, with manganin wires in red) still maintains 4 probe setup thus resistance of the manganin wires does not contribute to the resistance measurement result. Unlike copper, manganin or constantan has thermal conductivity that decreases with temperature. At temperatures below 50 K, manganin thermal conductivity is reduced to a few W/m.K and to 0.1 W/m.K at 2 K. Its electrical resistivity however maintains constant across the temperature range from room temperature to liquid helium.^{45,46}

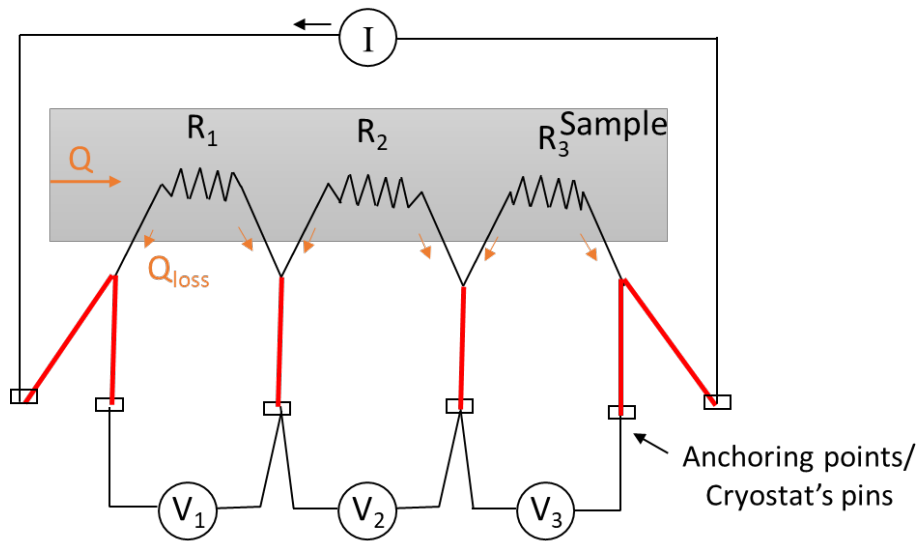


Figure 33. Modified wiring diagram to prevent heat loss at low temperature. Reds are manganin wires

Similar to the cernox sensors circuit, the circuitry for the resistive heater that also measures heater power should also be insulated with manganin wires using the same principle.

Chapter 3. Thermal chiral anomaly in field-induced ideal Weyl semimetal phase of Bi-Sb alloys

3.1. Motivation and theory

The chiral anomaly was predicted²² to be an experimental signature for the existence of WSMs. However, previous experimental determination methods for the chiral anomaly are tainted. First, currently investigated WSMs^{47–49} are not ideal; their Fermi surfaces contain features other than Weyl nodes. Second, the signature chiral anomaly feature is a negative longitudinal magnetoresistance (MR);²³ though the distorted current lines in the applied magnetic field complicates the interpretation.

Ideal WSMs have two distinguishing characteristics. First, the band structure has linearly dispersing bands that intersect at Weyl points (WPs) in a system that breaks time reversal symmetry (TRS) or inversion symmetry (IS). Second, the electrochemical potential μ is at the WP energy ($\mu = 0$). In an ideal WSM, there are no trivial bands at energy μ , which is pinned to the WPs. Then, the Fermi surface consists only of WPs with opposite Berry curvatures, W_R right-handed or W_L left-handed. One pair of WPs in the Brillouin zone (BZ) is the minimum required by the Nielsen-Ninomiya theorem²² for a TRS-breaking ideal WSM. Experimentally, an ideal WSM displays no Shubnikov-de Haas (SdH) oscillations; at finite temperature, a nearly equal density of intrinsic holes and electrons is excited thermally, with any unbalance due to unintentional doping smaller than this intrinsic concentration.

The chiral anomaly in ideal WSMs results from applying parallel electric \mathbf{E} and magnetic fields \mathbf{B} along the direction of the WP separation as discussed in Section 1.2.4.

The anomalous contribution to the electrical conductivity generated by N_w degenerate pairs of WPs is:

$$\sigma_{zz} = N_w \frac{e^2 v \tau}{4\pi \hbar \ell_B^2} = N_w \frac{e^3 v \tau}{4\pi \hbar^2} B_z \quad (3.1)$$

which is a negative longitudinal magneto resistivity. The scientific community considers the resulting negative longitudinal MR the crucial experimental chiral anomaly signature.^{39,47–49}

Negative MR was observed in many WSMs, e.g., XPn compounds (X=Nb, Ta; Pn=As, Sb)^{47–49} and Dirac semimetals,^{39,50–52} but also in materials without Weyl points near μ , e.g., XPn₂ compounds^{53–56} and elemental semimetal Bi.³⁹ Broadly observing this effect revealed that the negative MR is unlikely a unique chiral anomaly signature; other, classical effects might be present, as discussed next.^{40,57}

The classical effects that make longitudinal MR measurements ambiguous arise because the Lorentz force distorts the current flow spatial distribution in samples with high-mobility (μ_B) electrons under a magnetic field (i.e., when $\mu_B |\mathbf{B}| > 1$). This causes extrinsic, geometry-dependent MR mechanisms. The first is *current jetting*,^{48,53,57–59} arising in 4-contact measurements. With $\mathbf{B} // \mathbf{E}$, the Lorentz force concentrates the current in a cyclotron motion near the sample center. Progressively less current passes near the voltage probes as \mathbf{B} increases, lowering the measured voltage and possibly leading to the erroneous conclusion that the resistivity decreases with \mathbf{B} . The second is an extrinsic *positive geometrical MR* arising if \mathbf{B} is slightly misaligned vis-à-vis the current flow lines. In the present samples, striations present on the surface of a Czochralski-grown crystal⁴⁴ can

overwhelm the MR measurements, and extreme care needs to be taken with the sample alignment and geometry (see Section 2.3.2). Samples with reduced cross-section and smooth edges minimize both effects. Thermal conductivity $\kappa_{zz}(H_z)$ measurements avoid problems with extrinsic MR because there is no external current flow and the lattice contribution to κ maintains a more \mathbf{B} -independent heat flux than charge flux distribution in the sample (there is a magnetic-field effect on anharmonic phonon scattering,⁶⁰ but it is an order of magnitude smaller than the effects discussed here).

Energy transport in WSMs poses theoretical challenges not encountered in charge transport. From the equations of motion for charge carriers at the WP and the Boltzmann transport equation, we write the imbalance between left and right moving particles (δn_χ) and energy ($\delta \varepsilon_\chi$, the *thermal chiral anomaly*) in the presence of both an electric field \mathbf{E} and thermal gradient $\nabla_r T$ as:⁶¹

$$\delta n_\chi = \frac{\chi e^2 \tau}{4\pi^2 \hbar^2} [\mathbf{B} \cdot \mathbf{E}] C_0 + \frac{\chi e \tau}{4\pi^2 \hbar^2} \left[\mathbf{B} \cdot \frac{-\nabla_r T}{T} \right] C_1 \quad (3.2)$$

$$\delta \varepsilon_\chi = \frac{\chi e^2 \tau}{4\pi^2 \hbar^2} [\mathbf{B} \cdot \mathbf{E}] (\mu C_0 + C_1) + \frac{\chi e \tau}{4\pi^2 \hbar^2} \left[\mathbf{B} \cdot \frac{-\nabla_r T}{T} \right] (\mu C_1 + C_2) \quad (3.3)$$

where $C_m = \int (\varepsilon - \mu)^m \left(-\frac{\partial f_0}{\partial \varepsilon} \right) d\varepsilon$, $m \in \{0, 1, 2, \dots\}$ with f_0 the Fermi-Dirac distribution function. The thermal chiral anomaly thus has two terms: First, a temperature gradient $\nabla_r T$ alone, disregarding any induced electric field, creates an imbalance between the energy carried by the left and right movers while maintaining equal populations when $\mu = 0$ ($C_1 =$

0, $\delta n_\chi = 0$, $\delta \varepsilon_\chi \neq 0$). This response contrasts with the electrical case where $\nabla_r T = 0$ and \mathbf{E} create an imbalance between the populations of left and right movers while, when $\mu = 0$, maintaining the same total energy ($\delta n_\chi \neq 0$, $\delta \varepsilon_\chi = 0$). Second, when the sample is mounted in open-circuit conditions and no external electric field is applied, applying $\nabla_r T$ induces a Seebeck electric field $\mathbf{E} = S (-\nabla_r T)$ (S is the thermopower), driving both $\delta n_\chi \neq 0$ and $\delta \varepsilon_\chi \neq 0$. This creates an additional $\kappa_{zz}(H_z)$ term, the ambipolar thermal conductivity, ⁶² $S^2 T \sigma$. The total thermal conductivity becomes $\kappa_{zz} = \kappa_{zz,0} + S^2 \sigma T$, where $\kappa_{zz,0}$ denotes the energy carried directly by the charge carrier.

The experimental tests for these theories are first to observe an increase in electronic thermal conductivity in a longitudinal magnetic field, and second to verify the Wiedemann-Franz law (WFL) in the EQL:

$$\kappa_{zz} = L T \sigma_{zz} \quad (3.4),$$

with L the Lorenz ratio. If each electron carries charge e and entropy k_B , and conserves its energy during scattering, $L = L_0 = \pi^2 / 3 \left(k_B / e \right)^2$. The experiment consists in testing the ratio $\kappa_{zz} / T \sigma_{zz}$, which we define as L , against the independent variables H_z and T , and, if L is independent of these, to verify if the value equals L_0 . In particular, a Weyl semimetal in which inelastic scattering is limited by the inter-WP scattering time τ , in the quasi-classical limit at $H=0$ is expected to have $L = 7\pi^2 / 5 \left(k_B / e \right)^2$ but $L=L_0$ in the EQL.⁶³ In the

presence of ambipolar conduction $L > L_0$, because L_0 applies only to $\kappa_{zz,0}$. Extrinsic effects result in underestimations (current jetting) or overestimations (geometrical MR) of L .

We report the thermal conductivity $\kappa_{zz}(H_z)$ dependence on H_z , and show experimentally that the chiral anomaly affects energy and charge transport similarly, i.e., $d\kappa_{zz}/dH_z > 0$, as expected from Eq. (3.1) and (3.4). We then experimentally derive values for L . Previous $\kappa_{zz}(H_z)$ measurements exist: an increase in κ_{zz} for GdPtBi has been reported at $H_z = 9$ T.⁶⁴ However, those samples exhibited SdH oscillations in their MR, which proves that μ is not at the WPs, and the increase in κ_{zz} is also observed in transverse field, which is difficult to reconcile with Weyl physics. A positive magneto thermoelectric conductance is observed in NbP,⁶⁵ dubbed a gravitational anomaly due to the formal link^{66,67} between gradients $\nabla\Phi$ in the gravitational field and $\nabla_r T$. Here, we report $\kappa_{zz}(H_z)$ in magnetic-field induced ideal WSMs, $\text{Bi}_{1-x}\text{Sb}_x$ alloys with $x = 11$ and 15 at.%. We demonstrate that these alloy samples, topological insulators (TIs) at $|\mathbf{B}|=0$,¹⁴ become WSMs without trivial bands in a quantizing magnetic field along the trigonal axis ($z=[001]$). We further identify the WP locations. In these material samples, we show their carrier concentrations are intrinsic above ~ 30 K, where the relevant κ_{zz} data are collected. This makes them ideal WSMs by construction. Their $\kappa_{zz}(H_z)$ shows an electronic thermal conductivity increase by up to 300% at 9 T. Lorenz ratio $L = \kappa_{zz} / T\sigma_{zz}$ measurements show that $L \approx L_0$. We show that the effect is robust to disorder and phonon scattering, depends as

expected on the ratio of the temperature to the Weyl bandwidths, and is absent in samples that fall outside the range of compositions where WSMs form.

3.2. Magnetic Field-induced $\text{Bi}_{1-x}\text{Sb}_x$ Weyl Semimetals.

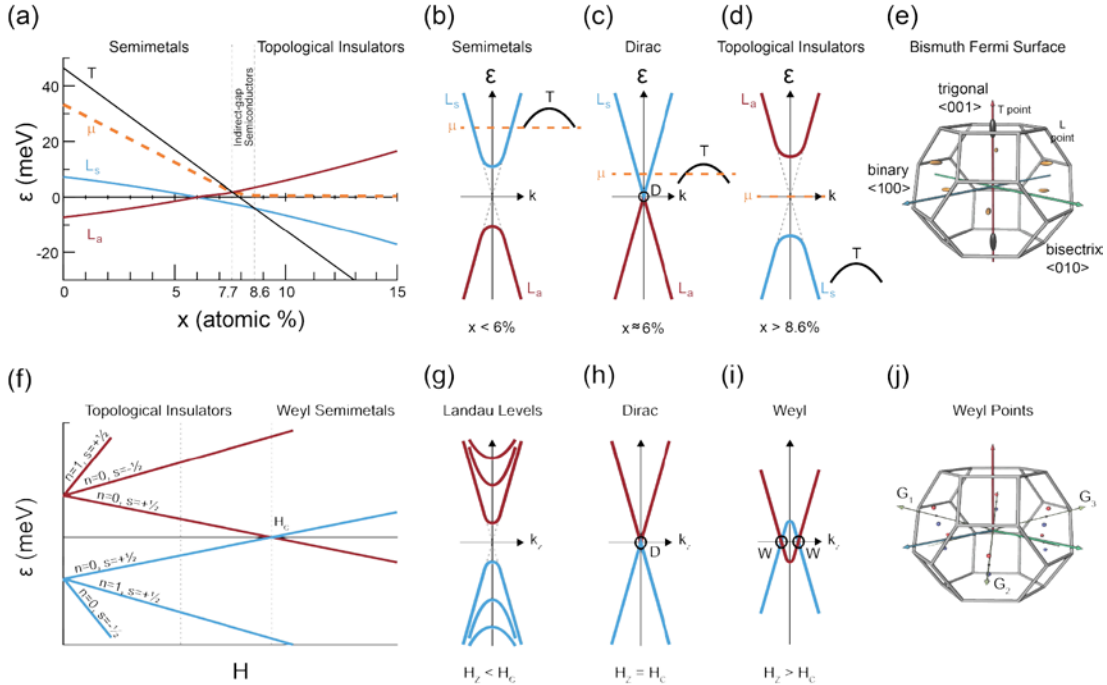


Figure 34. Evolution of $\text{Bi}_{1-x}\text{Sb}_x$ alloys with composition and magnetic field:

(a) Band-edge energies' composition dependence at zero applied magnetic field. Elemental semimetal Bi has electrons residing in a conduction band, L_s , and holes in the valence band, T ; with a filled second valence band, L_a . Adding Sb (x in at.%), the $L_a - L_s$ gap closes until the bands intersect near $x \approx 6\%$. The T -band edge intersects that of the L_a and L_s bands at $x \approx 7.7\%$ and $x \approx 8.6\%$, respectively. The chemical potential $\mu(x)$ evolution for samples with no unintentional doping is shown as a dashed orange line. Alloys with $x < 7.7\%$ are semimetals with μ in a band; alloys with $x > 8.6\%$ are direct-gap topological insulators with μ at mid-gap in undoped material. (b) Semimetal Bi dispersion relation, (c) $\text{Bi}_{94}\text{Sb}_6$ alloys' Dirac dispersion, and (d) Bi-Sb TIs' dispersion. (e) Bi BZ and Fermi surfaces: electrons fill 6 pockets at the BZ L -points; holes fill 2 pockets at the T -points. (f) TI alloy $\text{Bi}_{89}\text{Sb}_{11}$ band-edge energies in a magnetic field H_z applied along the trigonal direction. The field separates the L_a and L_s valence bands into Landau levels, with orbital quantum number n and spin s . With increasing H_z , the $n=0, s=1/2$ of the L_a and L_s bands cross again at a critical field H_c . At higher fields, the crossing points develop into Weyl points. (g) Dispersions along k_z at $H_z < H_c$. (h) Dispersion in k_z at $H_z = H_c$. (i) Dispersion at $H_z > H_c$ becomes that of a field-induced Weyl semimetal. (j) $\text{Bi}_{1-x}\text{Sb}_x$ BZ with locations of calculated WPs schematically; blue and red points indicate WPs with opposite Berry curvature.

We predict that $\text{Bi}_{1-x}\text{Sb}_x$ alloys ($\sim 9 < x < \approx 18$ at%) become ideal WSMs in a magnetic field H_z above a critical threshold H_C because: (1) their conduction and valence bands cross at H_C ; (2) at $H_z > H_C$ two crossing points appear that are Berry curvature monopoles, i.e., WPs; and (3) no trivial bands cross μ .

The band structure of $\text{Bi}_{1-x}\text{Sb}_x$ alloys (**Figure 34 (a)-(e)**) at zero magnetic field evolves with increasing x through four successive regimes:⁶⁸ conventional semimetals, semimetals with an inverted band at the BZ L-point, semiconductors, and TIs. A tight-binding Hamiltonian describes the band structure of unalloyed bismuth and antimony,⁶⁹ incorporating the s - and p -orbitals of the two atoms in the conventional hexagonal unit cell. The alloy electronic structure is calculated using a modified virtual crystal approximation (VCA) in which the tight-binding parameters are obtained directly from those of the elemental semimetals and agree with previous experiments⁷⁰⁻⁷² within the experimental uncertainty on compositions (1 at.%). The details of the electronic structure of the Bi-Sb alloy change slowly as the band positions change relative to μ , as indicated by the nearly unchanged intrinsic spin-Hall conductivity calculated through the semi-metal-TI transitions.⁷³

With these parameters, we show that a quantizing magnetic field along the trigonal direction of the TIs (**Fig. 34 (f)-(i)**) inverts the bands again. The g_{eff} -tensors at the high-symmetry BZ L- and T-points are calculated⁷⁴ from the tight-binding electronic structure above for valence and conduction bands. The T-point g_{eff} -tensor has only one non-zero component, $g_{\mu z} = 20.5$, which only couples to the magnetic field along z . The more complicated effective g_{eff} -tensor at the L-point shows significant asymmetry. For the

conduction and valence bands at the Bi₈₉Sb₁₁ L-point with a magnetic field applied along the trigonal direction, the calculated values are $g_z = -77.5$ and -72.3 , respectively. SdH oscillations⁷⁵ in Bi confirm the extremely large g -factor values experimentally. This results in an anomalously large effective Zeeman splitting energy $\Delta\varepsilon_z = -\mu_B g_z B_z \approx -4.2$ meV/T at the L-point that overwhelms the orbital splitting of the LLs. Consequently, the band gaps close (**Fig. 34 f,h**) at a critical field H_C , calculated to be ~ 3 T for alloy compositions near $x=11\%$. Magnetic-field-induced band closings are uncommon but have been reported via magneto-optical measurements on Bi.⁷⁶ H_C is sensitive to parameter values used in the calculations, and is of the order of 1–4 T. At $H_z > H_C$, the Zeeman energy increase further splits the degeneracy of the Kramers doublets (points W in **Fig. 34 (i)**).

We further demonstrate that the Kramers doublets become WPs resulting from explicit TRS breaking by showing that the Chern number changes by an integer for a momentum slice taken between these WPs. The Chern number in this case is an integer that counts the monopoles enclosed in a given Gaussian surface in the BZ.

We calculate the Berry curvature distribution $\Omega_n(\mathbf{k})$ in momentum space to search for the WPs where the Berry curvature is concentrated and singular. The two WPs carry monopole Berry curvature $\Omega(\mathbf{k}) = \chi \mathbf{k}/k^3$ with opposite chirality, $\chi = \pm 1$. Integrating the Berry curvature provides the Chern number. A Chern number integer change provides evidence of a topology change and existence of WPs, a pair of points separated symmetrically near each L-point in the 3D BZ (**Fig. 34 (j)**). The separation between the two WPs is in the binary-trigonal plane with a major component along the trigonal direction

(coinciding with the external magnetic field direction) and a minor component along the bisectrix direction.

Finally, to ascertain that the $\text{Bi}_{89}\text{Sb}_{11}$ system is an ideal WSM at $H_z > H_C$, the model verifies that no trivial bands contribute to transport: neither the T-point band nor any new bands move near μ with increasing H_z . In a semiconductor or semimetal without unintentional doping, μ is pinned at the energy of the lowest DOS, which, without trivial bands, occurs at the WPs. Therefore, if we can minimize unintentional doping, our experimental systems below will form ideal WSMs by construction.

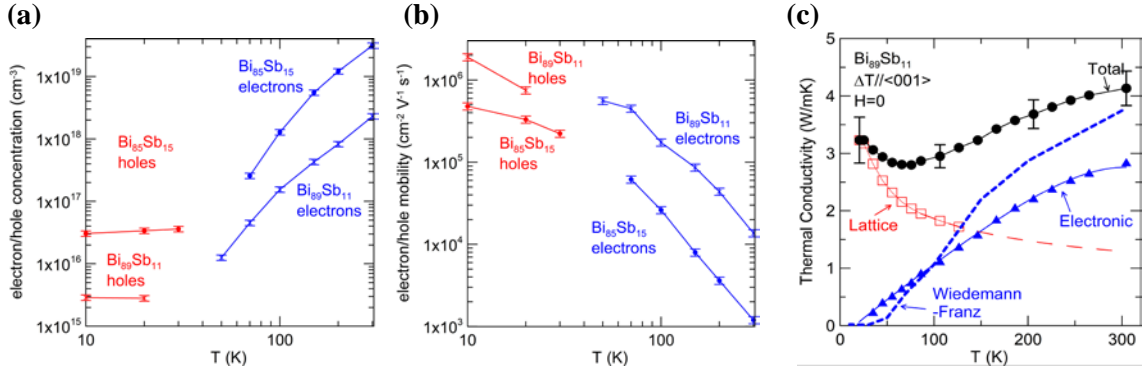


Figure 35. $\text{Bi}_{89}\text{Sb}_{11}$ and $\text{Bi}_{85}\text{Sb}_{15}$ electronic and thermal properties:

(a) carrier concentration and (b) mobility; the samples switch from dominantly n-type at 300 K to dominantly p-type at 10 K. (c) $\text{Bi}_{89}\text{Sb}_{11}$ zero-field κ_{zz} separated into lattice κ_L and electronic κ_E parts. The dashed blue line is κ_E calculated from the resistivity and the Wiedemann-Franz law (WFL) with $L=L_0$. The error bars are standard deviation and their origins are described in the methods section.

3.3. Magneto-Thermal Conductivity Measurements

Evidence for the thermal chiral anomaly is shown in six single-crystal samples of $\text{Bi}_{1-x}\text{Sb}_x$, $x \sim 11$ and 15 at%. For control, we report the absence of the anomaly in two semi-metallic samples with $x \approx 5\%$; for this composition an ideal WSM does not exist. The sample compositions and characterizations are presented in **Table 4**. The temperature

dependence of the resistivity and low-field Hall effect of the best samples (#1 with $x=11\%$ and $x=15\%$) are used to derive carrier concentration and mobility (**Fig. 35 (a-b)**) showing that charge carriers freeze out. This, and the absence of SdH oscillations in the high-field longitudinal magneto-resistivity down to 2 K and other transport properties, indicate that they are ideal WSMs. The zero-field thermal conductivity κ_{zz} along the trigonal direction of sample #1 is given in **Fig. 35(c)**. It consists of a phonon κ_L and electronic κ_E contribution separated by measuring $\kappa_{zz}(H_y)$ which shows a steady decrease to a saturation value at high field. This is the ordinary behavior of high-mobility materials^{29,77} used to isolate $\kappa_L = \lim_{H_y \rightarrow \infty} (\kappa_{zz}(H_y))$ for $T < 120$ K. At $T > 120$ K, $\kappa_L(T)$ is extrapolated following a $T^{-1/3}$ law⁷⁸ to 300 K. κ_L dominates κ_{zz} below 35 K, limiting measurements of κ_E to $T > 35$ K. At zero field, $\kappa_E(H_z=0)$ follows the WFL with $L=L_0$ (dashed line in **Fig. 35(c)**) above 30 K.

Table 4. List of Bi-Sb alloy samples used in the study

Sample name	Growth	x	Used for	density	mobility
		at%		cm ⁻³	cm ² V ⁻¹ s ⁻¹
Sample #1	TMZ	10.5±0.5	$\kappa_{zz}(H_z)$, $\kappa_{zz}(H_y)$ $\kappa_{zz}(H_z)$ Ag contacts		
Hall	TMZ	10.5±0.5	Hall, resistivity	3×10^{15} (10 K)	1.9×10^6 (10 K)
Sample #2	Czochralski	11.3±0.7	Negative MR		
		11.3±0.7	Magneto-Seebeck		
		11.3±0.7	$\kappa_{zz}(H_z)$, $\kappa_{zz}(H_y)$		
Sample #3	Czochralski	11.3±0.7	$\kappa_{zz}(H_z)$, $\kappa_{zz}(H_y)$		
		11.3±0.7	$\kappa_{zz}(H_z)$ -angular dependence		
Sample #4	Czochralski	11.3±0.7	$\kappa_{zz}(H_z)$, $\kappa_{zz}(H_y)$		
Hall	Czochralski	11.3±0.7	Hall, resistivity	1.4×10^{16} (12 K)	2×10^4 (12 K)
Sample #5	TMZ	15.1±0.7	$\kappa_{zz}(H_z)$, $\kappa_{zz}(H_y)$		
Hall	TMZ	15.1±0.7	Hall, resistivity	3×10^{16} (10 K)	4.5×10^5 (10 K)
Sample #6	TMZ	10.5±0.5	$\kappa_{zz}(H_z)$, $\rho_{zz}(H_y)$	as #1	as #1
semimetal	Bridgeman	5±0.5	$\kappa_{zz}(H_z)$ $\kappa_{zz}(H_z)$ Ag contacts, Hall, resistivity	4.5×10^{16} (79 K)	8×10^4 (79 K)

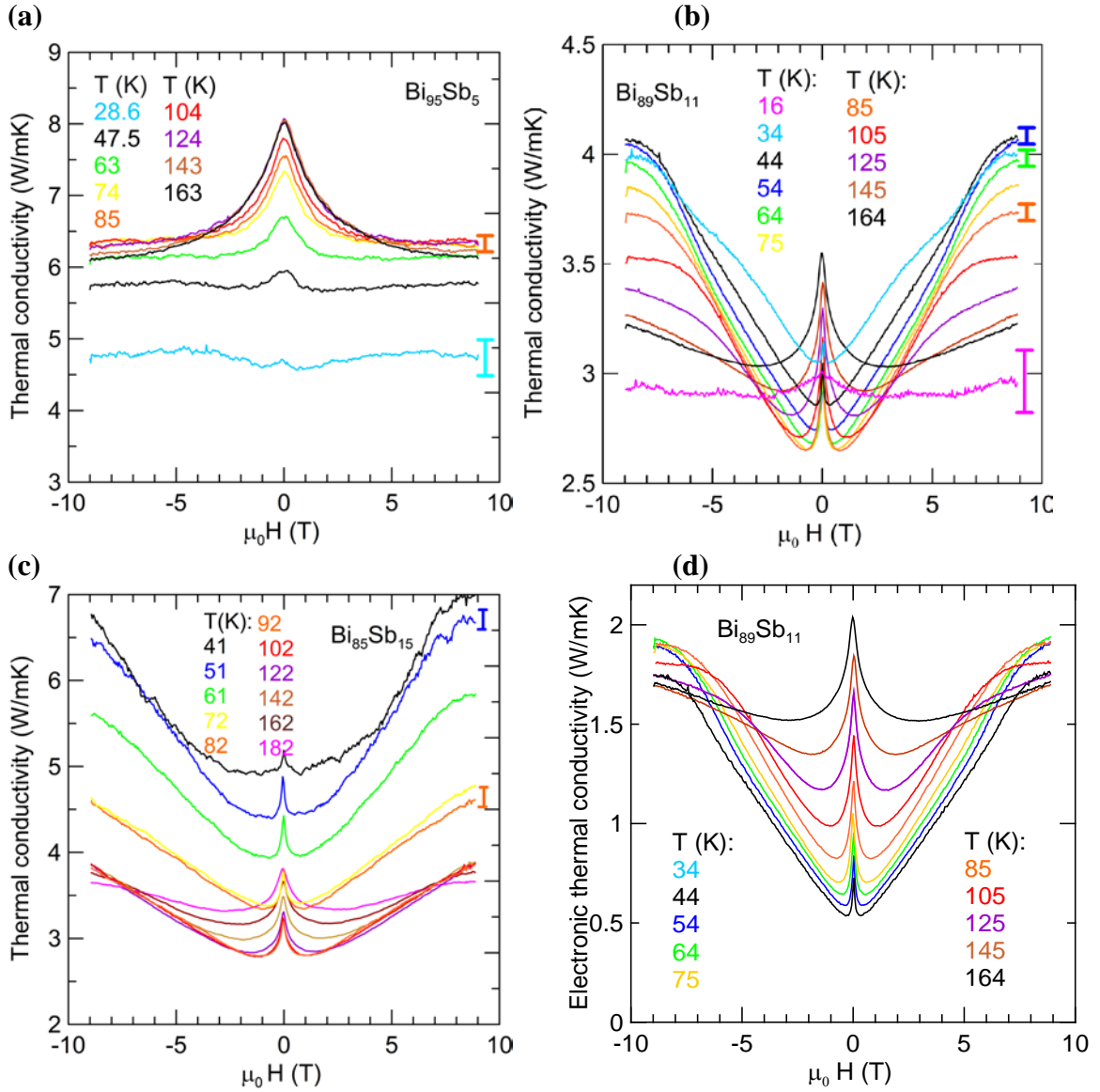


Figure 36. $\text{Bi}_{95}\text{Sb}_5$, $\text{Bi}_{89}\text{Sb}_{11}$, and $\text{Bi}_{85}\text{Sb}_{15}$ thermal conductivity $\kappa_{zz}(H_z)$ dependence on longitudinal magnetic field along the trigonal direction at temperatures indicated: (a) $\text{Bi}_{95}\text{Sb}_5$, a conventional, not Weyl, semimetal, has $\kappa_{zz}(H_z)$ that monotonically decreases with H_z , due to a positive MR. The $\kappa_{zz}(H_z)$ of (b) $\text{Bi}_{89}\text{Sb}_{11}$ (sample 1) and (c) $\text{Bi}_{85}\text{Sb}_{15}$ shows a decrease due to a conventional positive MR in the TI regime, followed by an increase that we posit is evidence for the thermal chiral anomaly. (d) The electronic contribution κ_E of the total thermal conductivity κ_{zz} for $\text{Bi}_{89}\text{Sb}_{11}$ is obtained by subtracting the lattice contribution κ_L . κ_E shows a >300% increase with field at 9 T. The error bars, the standard deviation relative to the field dependence, are obtained as described in the methods section. They are temperature dependent and are the same for all samples at the same temperatures.

Figure 36 shows the longitudinal magneto-thermal conductivity $\kappa_{zz}(H_z)$ of three samples: **(a)** Bi₉₅Sb₅ (not a WSM); **(b)** Bi₈₉Sb₁₁, and **(c)** Bi₈₅Sb₁₅; (both WSMs above 1–2 T). $\kappa_E(H_z)$ of Bi₈₉Sb₁₁ is reported as a function of H_z in **Fig. 36 (d)**: the relative κ_E increase in magnetic field reaches above 300% from 34 to 85 K at 9 T. At low field, $d\kappa_{zz}/dH_z < 0$ for $H_z < 1$ T at $T < 50$ K and $H_z < 3$ T at $T = 160$ K. Here, the last LLs of the conduction and valence bands have not crossed in energy. At high field, in WSM phase, $d\kappa_{zz}/dH_z > 0$. We posit the large increase in $\kappa_{zz}(H_z)$ (**Fig. 36(b-d)**) at high field is experimental evidence for the thermal chiral anomaly. The following observations justify the thesis. First, **Fig. 36(a)** shows that $d\kappa_{zz}/dH_z < 0$ at all fields for Bi₉₅Sb₅, which in zero field is a conventional semimetal, not a TI, with a trivial hole pocket in its Fermi surface at the BZ T-point. In Bi₉₅Sb₅, the band crossing with field does not create an ideal WSM phase; if the $d\kappa_{zz}/dH_z > 0$ observation on Bi₈₉Sb₁₁ and Bi₈₅Sb₁₅ resulted from effects other than the chiral anomaly, e.g., ionized impurity scattering,⁷⁸ known to be weak even in doped Bi,⁴⁴ it also would occur in similarly prepared Bi₉₅Sb₅. Second, to ascertain that a circulating current or an artifact on the sample surfaces does not induce the effect, samples of Bi₉₅Sb₅ and Bi₈₉Sb₁₁ were mounted with its top and bottom faces covered by electrically conducting Ag epoxy. We observe no effect from the added surface conducting layers. Third, the $d\kappa_{zz}/dH_z > 0$ data at high H_z were reproduced on Bi₈₉Sb₁₁ samples 2–4, which had a mobility of only 2×10^4 cm²V⁻¹s⁻¹ at 12 K, demonstrating the robustness of the

observations vis-à-vis defect scattering. Fourth, $d\kappa_{zz}/dH_z > 0$ in **Fig. 36(b-d)** is observed up to 200 K, twice the Bi Debye temperature, demonstrating the robustness of the effect to phonon scattering. The effect disappears only for $T > 200$ K, which we will demonstrate in the next section to be due to thermal smearing of the carrier population between the WPs, independent of phonons.

3.4. Verification of the Wiedemann-Franz law and evidence for inter-Weyl point scattering

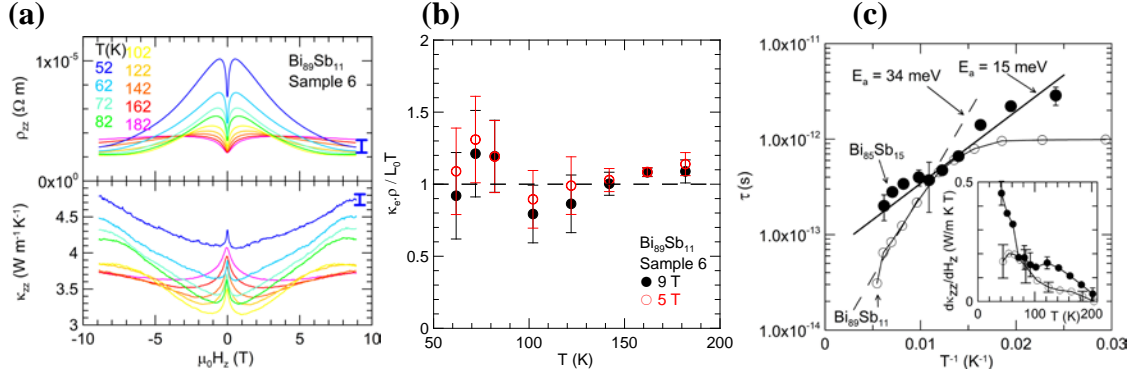


Figure 37. Wiedemann-Franz law verification; temperature and angular dependence of the $\kappa_{zz}(H_z)$ increase:

(a) $\text{Bi}_{89}\text{Sb}_{11}$ (sample 6) $\kappa_{zz}(H_z)$ and $\sigma_{zz}(H_z)$. The error bars on the resistivity and thermal conductivity are the standard deviation obtained as described in Chapter 2. (b) Lorenz ratio $L = \kappa_{zz,e}(H_z) / \sigma_{zz}(H_z)$ derived from (a), normalized to L_0T at two values of H_z ; L is independent of H_z within the error bar. The error bars arise from the errors on $\sigma_{zz}(H_z)$ and on $\kappa_{zz,e}(H_z)$ determined from $\kappa_{zz,e}(H_z)$ and κ_L . (c) The inter-WP scattering time τ , derived from equation (5) fits Arrhenius plots (lines) at $T > 60$ K with an activation energy of $E_a = 34$ meV for $\text{Bi}_{89}\text{Sb}_{11}$ and 15 meV for $\text{Bi}_{85}\text{Sb}_{15}$. The inset shows the temperature dependence of $d\kappa_{zz}(H_z)/dH_z$ between 4 and 8 T of TMZ sample #1 $\text{Bi}_{89}\text{Sb}_{11}$ and $\text{Bi}_{85}\text{Sb}_{15}$. The error bars are the standard deviation.

Simultaneous $\kappa_{zz}(H_z)$ and MR ($\rho_{zz}(H_z)$) measurements were taken on a specially prepared $\text{Bi}_{89}\text{Sb}_{11}$ sample (sample #6), and are shown **Fig. 37a**. Subtracting κ_L ⁷⁷ from $\kappa_{zz}(H_z)$ gives $\kappa_{zz,e}(H_z)$. **Fig. 37b** verifies that the WFL holds in an applied field with $L \approx L_0$,

as expected theoretically in an ideal WSM where the WSM phase is induced in EQL. The error bar increases with decreasing T as κ_L increasingly dominates $\kappa_{zz}(H_z)$ and becomes as large as the signal below 50 K; κ_L masks the electronic contribution completely below 35 K. This knowledge allows fitting the $d\kappa_{zz}/dH_z$ (inset in **Fig. 37c**) experimental temperature dependence for $T > 60$ K. Using equations (1) and (4) with $L=L_0$, $N_w=12$ to derive the thermal chiral conductivity, then taking its field derivative, we obtain:

$$\frac{d\kappa_{zz}}{dH_z} = \frac{\pi e v k_B^2}{\hbar^2} T \tau \quad (3.5).$$

Using the calculated $v \approx 4.5 \times 10^5$ m/s, Eq. (3.5) can be used to derive the inter-WP scattering time $\tau(T)$ (**Fig. 37(c)**). Below ~ 60 K, $\tau \sim 10^{-12}$ s and temperature independent for Bi₈₉Sb₁₁, one order of magnitude longer than the electron relaxation time in Bi₉₅Sb₅ at 4.2 K. This suggests a high degree of charge-transport protection. In Bi₈₅Sb₁₅ and at $T > 60$ K in Bi₈₉Sb₁₁, τ increases exponentially with T^{-1} , activated behavior with an activation energy $E_a = 34 \pm 2$ meV for Bi₈₉Sb₁₁ and $E_a = 15 \pm 2$ meV for Bi₈₅Sb₁₅, as expected when charge carriers are thermally excited above the Weyl bandwidth limit τ . The calculated band width at 7.5 T is $E_{BW} = 35$ meV for $x = 10.5$ at.% and $E_{BW} = 20$ meV at 7.5 T for $x = 15.1$ at.%, the measured concentrations in the samples. The correspondence between E_a and E_{BW} for two compositions suggests that thermal smearing of the carrier population between the WPs is the main mechanism inhibiting the observed increase in $\kappa_{zz}(H_z)$, and that E_{BW} is the only energy scale in the observations.

Altogether, we posit that the $d\kappa_{zz}/dH_z > 0$ observation constitutes robust experimental evidence for energy pumping between opposite chirality monopoles when a thermal gradient is applied parallel to a magnetic field in an ideal WSM. This is related to the excess electrical conductivity due to the charge pumping between opposite chirality monopoles, the chiral anomaly, and by the Wiedemann-Franz law with a Lorenz number of $\pi^2/3 \left(k_b/e\right)^2$. The robustness of the results vis-à-vis defect and phonon scattering, and the identification of the Weyl bandwidth as the only energy scale, all point to the topological origin of the data.

Chapter 4. Exciton condensate-phonon coupling in Ta_2NiSe_5 excitonic insulator

4.1. Introduction

Excitons are a bound state of an electron-hole pair that exists in insulators, semiconductors, and some liquids. Excitons form in both direct-gap (light exciton) and indirect gap (dark exciton) semiconductors. Spatial delocalization increases the exciton lifetime, favoring their spontaneous formation. Most excitonic systems are either layered, e.g. in the MoSe_2 – WSe_2 system,⁷⁹ or chained, with electrons and holes localized in different layers or chains. An excitonic insulator (EI) is either a narrow gap semiconductor or a semimetal with small band overlap. A flat dispersion around the top of the valence band is then assigned as the effect of excitonic coupling between the valence and conduction bands; this was observed experimentally.^{80,81} The flat band signify that the electrons and holes are localized as their velocity becomes near zero thus supports its spontaneous formation of excitons. Below the critical temperature excitons forms Bose-Einstein condensates and the material enters excitonic insulator phase.^{80–82}

Since excitons do not carry charge, the thermal conductivity is the only convenient transport measurement that can be carried out on EI systems. The present paper does so in Ta_2NiSe_5 , using Ta_2NiS_5 as a “null-experiment”.

Ta_2NiSe_5 , a presumed EI, is layered with the layers stacked along the b direction. Each layer in a-c plane consists of TaSe_6 and NiSe_4 chains along the a direction. The c direction is perpendicular to the chains. Band calculations indicate small direct gap at Γ -point. The valence band is dominantly composed of states associated with the Ni 3d orbitals

while conduction band is dominantly composed of Ta 5d orbitals. Holes and electrons both exists at the Γ -point, but they are spatially delocalized in real space, residing in the Ni and Ta chains, respectively. ARPES data show the signature flat bands at Γ -point,^{81,83} and high temperature gap of about 0.16 eV.^{84,85} Upon cooling through 328 K, the crystal undergoes a structural phase transition from orthorhombic to monoclinic,⁸⁶ which is often considered to be the critical temperature for the transition to an EI state.

Ta₂NiS₅ is a sister compound of Ta₂NiSe₅ with a band gap at Γ -point of ~0.25 eV.⁸⁵ ARPES data do not show the signature band flattening of an EI⁸⁷ and the lattice distortion is faint and occurs at lower temperature ~120 K⁸⁸. These differences that make the sulfide a comparison material to isolate the effect of the excitons in this study of the thermal transport in the selenide.

The formation of a Bose-Einstein condensate (BEC) of excitons in the direct-gap Ta₂NiSe₅ is expected to break the crystal lattice symmetry⁸⁸ and indeed this lattice symmetry breaking was observed to occur below a critical temperature $T_c = 328$ K. Despite arguments that the nature of the symmetry breaking is purely structural,^{89,90} numerous experimental and theoretical studies provided strong evidence that the phase transformation and the formation of an EI phase are linked. Coupling of the excitonic continuum with the *B2g* phonon, which describes oscillation of Ta atoms relative to Ni atoms, plays crucial role in driving the structural transition.^{88,91-93} In S-Se alloys Ta₂Ni(Se_{1-x}S_x)₅, the structural transition persists, but T_c decreases with increasing x and the EI phase disappears for $x > 0.7$.^{88,91,94}

Werdehausen et al⁹⁵ proved experimentally that in Ta₂NiSe₅ the condensed exciton strongly couples to the *A_g* TO optical phonon at 1 THz, which describes the transverse (relative to *a*) oscillation of neighboring Ta-Ni-Ta blocks. This coupling is absent in Ta₂NiS₅, where that TO phonon's frequency is 1.2 THz. In the selenide, the coupled 1 THz mode's amplitude follows the characteristic behavior of a purely electronic Higgs-like amplitude mode. A similar coupling between condensed excitons and a phonon is present in Tm mono-chalcogenides.⁹⁶ More specifically, TmSe_{0.45}Te_{0.55} can be tuned from a semiconductor phase to an EI to a semimetal phase by applying pressure, enabling Wachter and Bucher⁹⁶ to follow the specific heat of the compound through the EI transition. They observe that the specific heat is depleted in the EI phase, and attribute that to the strong exciton-phonon coupling. Upon cooling in the EI phase, the paper stated “more and more wave-like phonons become locked onto the excitons, giving no more contributions to the specific heat”.⁹⁶ This work presents similar evidence in Ta₂NiSe₅.

There are many interesting theoretical predictions for energy transport in EI's. First, Remez et al⁹⁷ predict energy propagation with long mean free path by Goldstone modes, a gapless branch of the collective modes, which should manifest themselves in an additional thermal conductivity and heat capacity. Second, there is a controversy on the potential of the BEC collective state for superfluid energy transport.⁹⁸ Wachter claimed there is possibility of a superfluid phase in a Bose condensed excitonic state TmSe_{0.45}Te_{0.55},^{96,99} but Zittartz' calculations support a classical phonon thermal conductivity in EI's.⁹⁸ A recent theory also showed there is additional thermal conductivity produced by the additional heat current driven by the EI.¹⁰⁰ A third question concerns the role of the 1 THz TO mode in

Ta₂NiSe₅ (1.2THz in Ta₂NiS₅), because the unique low energy of this mode promises possibility to observe its thermal behavior at low temperature.

In this paper, we first report that Ta₂NiS₅ has a much lower thermal conductivity κ below 100K than Ta₂NiSe₅ in spite of its lighter average atomic mass. In the sulfide, heat conduction is by phonons. In Ta₂NiS₅ below 60K we observe a depletion in the temperature dependence of κ but an Einstein-mode-like excess in C . Together, these observations suggest that in Ta₂NiS₅ a phonon mode at an energy close to the 1.2THz mode does not conduct heat but rather scatters the heat carrying phonons, dominantly the acoustic ones.

Turning next to Ta₂NiSe₅, the excess C is also observed, but it is two times smaller than in Ta₂NiS₅. This is reminiscent of the case of the EI phase of TmSe_{0.45}Te_{0.55} where the phonon coupled to the exciton has no specific heat.⁹⁶ Then we address the question as to whether the higher κ of the selenide is due to conduction by something other than phonons. Inspired by thermal conductivity measurements on superfluid ⁴He, we looked for deviations from Fourier's law and for size effects as possible evidence for conduction by the BEC but found none. Using the thermal diffusivity as a direct measurement of the mean free path (mfp) of the heat carriers, which assumes they are phonons, the values found for Ta₂NiSe₅ are characteristic of phonons, approaching the sample's thickness at 4K but decreasing by 4 orders of magnitude at 200 K. There is no evidence for energy conduction by a wave (e.g. a possible Goldstone mode) that would have mean free path longer than 1 μm at $T \gg 10\text{K}$. At $T > 100\text{K}$, the mfp of the sulfide and selenide behave similarly but within a factor of 2, suggesting that heat is conducted by phonons also in Ta₂NiSe₅. Below 50K, the difference in phonon mean free path between sulfide and

selenide grows to an order of magnitude, suggesting that the phonon-phonon Umklapp scattering is much stronger in the sulfide than in the selenide. We attribute that to the possibility that the 1.2 THz mode in the sulfide provides for a high density of available states for acoustic phonons to scatter into. In contrast, the 1 THz mode in the selenide, which has no heat capacity, does not. Our results therefore provide an evidence in a transport property for a strong coupling between the EI and one particular phonon. The ability to deplete the condensate optically^{95,101} then promises a new pathway to tune thermal properties of Ta_2NiSe_5 and create an optically actuated all-solid-state heat switch.

4.2. Experimental Results

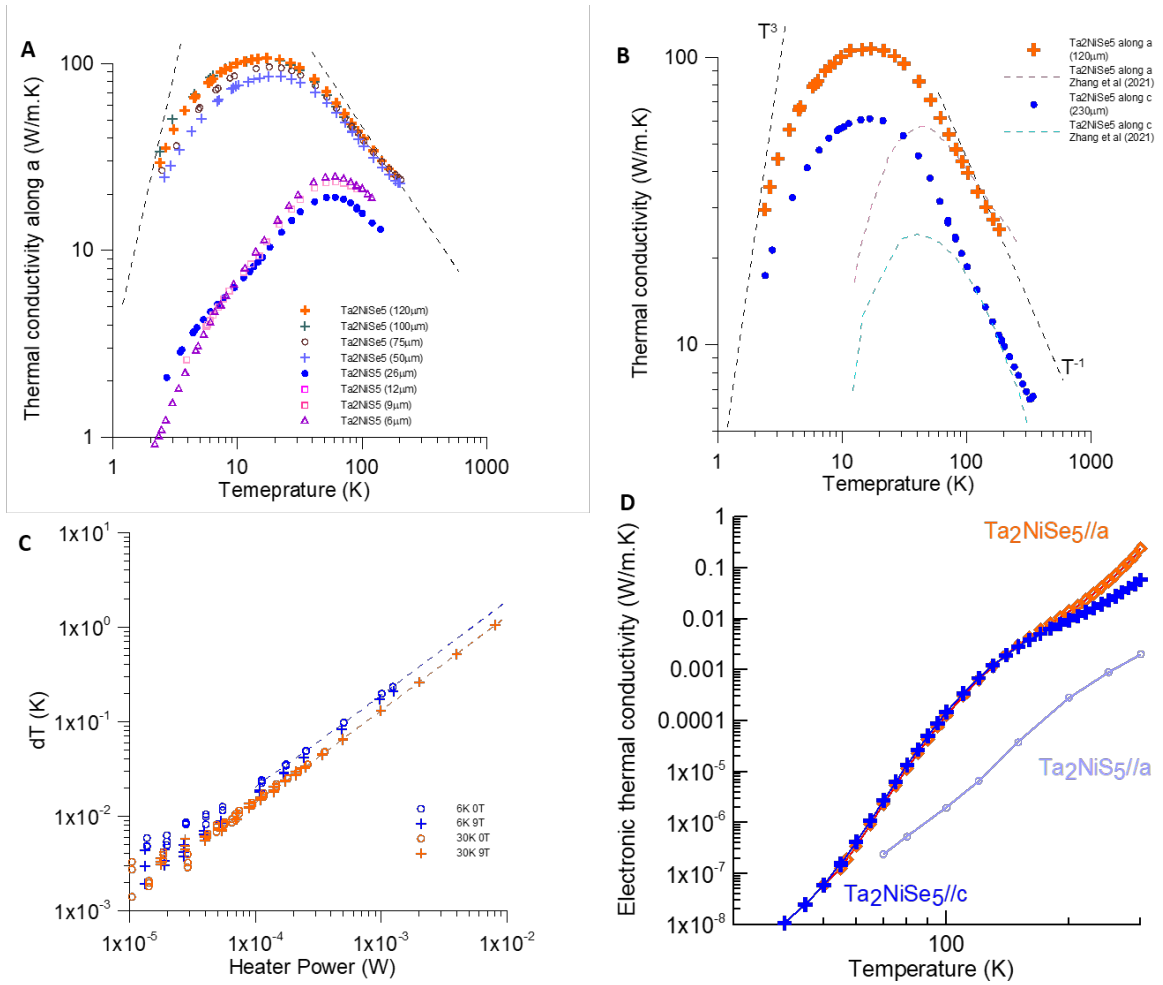


Figure 38. Thermal conductivity analysis of 4 different samples of Ta₂NiSe₅ and of 3 samples Ta₂NiS₅:

(A) Thermal conductivity of 4 different samples of Ta₂NiSe₅ and of 3 samples Ta₂NiS₅ along the a (in-chain) direction. Ta₂NiSe₅ shows much higher thermal conductivity despite Se being a heavier element than S. (B) Anisotropy of the thermal conductivity of Ta₂NiSe₅ along the a and c directions. Data by Zhang et al are added. (C) Heater power dependence of the temperature gradient in Ta₂NiSe₅, showing that the thermal conductivity follows Fourier's law. (D) electronic thermal conductivity calculated from the electrical conductivity and the Wiedemann-Franz law; the values are much lower than the measured thermal conductivity.

Figure 38a compares the measured thermal conductivity κ along the in-chain (a) direction of 4 samples of various thickness of Ta_2NiSe_5 to that of 3 samples of Ta_2NiS_5 . For Ta_2NiSe_5 , κ peaks at over 100 W/m.K around 15 K. At $T < 15$ K, κ decreases with decreasing temperature, tending asymptotically toward a T^3 law with a magnitude that scales with the sample thickness. At $T > 15$ K, the Ta_2NiSe_5 κ decreases monotonically with increasing temperature, tending asymptotically towards a T^{-1} function. The value at 100 K (46 W/m.K) is that predicted value by the Slack model (see Discussion) and is the same for all samples. **Fig. 38a** shows that the sample thickness (from 120 μm to 50 μm) does not affect the peak position much but affects the a-axis κ below 15 K. This suggests that the heat carrier's mean free path becomes of the order of tens of micrometers at 2 K. This behavior is consistent with a phonon-dominated thermal conductivity in the Casimir regime at $T \ll 15$ K and in the Umklapp regime at $T \gg 15$ K.

The Ta_2NiS_5 a-axis κ shown in **Fig. 38a** peaks at over 30 W/m.K at $T=60$ K. The main feature of this result is that the κ of the selenide is lower than that of the sulfide at all temperatures of the measurement, even though the average atomic mass of the selenide is 101 amu and that of the sulfide 72 amu. This is unexpected for phonon heat conduction. The natural isotopic abundance of Se (49.8% of ^{80}Se , 23.69% of ^{78}Se , 9.23% of ^{76}Se , 8.62% of ^{82}Se)¹⁰² is more varied than that of S (94.99% of ^{32}S), which, all things being equal, would result in an isotope-scattering-limited peak in κ that is lower and at a higher fraction of the Debye temperature¹⁰³ in Ta_2NiSe_5 than in Ta_2NiS_5 , again unlike the observation. Below 60 K, the Ta_2NiS_5 κ decreases and tends asymptotically toward a T^3 law, but unlike the case of the selenide, the sulfide's temperature dependence shows

inflection points in the 10-60 K temperature range. Note that $T=57$ K corresponds to the Einstein temperature of the 1.2 THz optical phonon mode in Ta_2NiS_5 .⁹⁵ As in the selenide, the temperature of the maximum in κ appears to be little affected by sample size, but the value of κ at $T < 10$ K is.

The anisotropy of the Ta_2NiSe_5 κ is shown in **Fig. 38b**, where the values along the in-chain (a) and cross-chain (c) directions of the 50 μm samples are shown. In the c direction, κ is about half of κ in the a direction, which will be shown to be about the anisotropy in the sound velocity. Also shown in **Fig. 38b** are the results reported earlier by Zhang et al.¹⁰⁴ At $T > 80$ K they are consistent with ours; this would be expected κ in the regime where $d\kappa/dT < 0$ is due to phonons in the Umklapp regime. Zhang et al's κ along a above 80 K also follows a T^{-1} law closely up to the structural transition temperature $T_c=328$ K. Our κ data are not quantitative above 200 K, due to metrology issues with the method used, and are not reported. At $T < 80$ K, the present data for Ta_2NiSe_5 peak at much lower temperature and much higher in value than Zhang et al's. The difference can be due to a difference between either the samples or the measurement techniques. When compare resistivity measured on the crystals, our samples showed lower resistances, especially below 60 K. The level of defects and doping in the sample can lead to change in the peak position and peak value of thermal conductivity. Zhang et. al. used heat pipe method, a comparative method which measure heat power in and out of the samples with thermocouples. At low temperatures where the κ of copper is high and that of constantan is low (the difference is 2 orders of magnitude), if conduction heat losses through copper wires at the heat links becomes significant, the error of the heat flux measurement could

be significant, resulting in error in calculated thermal conductivity. Our technique uses an absolute measurement of power and is optimized for low temperatures by using manganin wires posts to thermally insulate the thermometers wires and minimize heat loss through wires especially at the lowest temperatures; and estimate of the heat losses through wiring show them to be negligible compared to the heat flow in the sample.

At the transition temperature, both the Seebeck coefficient and κ along the c direction see abrupt change in slope whereas in the κ along the a direction the change is gradual and hardly noticeable. The abrupt change in thermal conductivity along c at the transition temperature is attributed to softening of a transverse acoustic phonon mode.¹⁰⁴

An extensive search was conducted to see if the κ of the selenide could be due to something other than phonons. The mean free path calculated in the next section (see Discussion) is less than 100 nm at 200 K, which is much shorter than the μm -scale propagation length of the coherent mode observed by Bretcher et al.,¹⁰⁵ although we cannot exclude a contribution by the Goldstone mode identified theoretically.⁹⁷

To look for heat conduction which involve potential superfluidity of a BEC, a careful examination of the power dependence of the temperature gradient and of the effect of the distance between thermometers on the sample was carried out. The heater power dependence measurements of κ (**Fig. 38c**) show that κ follows Fourier's with no evidence of a 2-fluid heat conduction mechanism related to superfluidity^{33,96,99,106} in ^4He , down to the lowest temperatures and the lowest power levels where we could still reliably measure the gradient. Neither did we observe a variation of κ with the distance between the

thermometers, at least at mm length scales. Our data thus offer no evidence for superfluid heat transport.

To look for a contribution of non-condensed excitons, the measurements were also carried out in an external magnetic field. Indeed, Dzyalozinskii¹⁰⁷ theorized that in an excitonic insulator, the Zeeman energy can open the band gap by $g\mu_B B$ (g is the Landé factor, μ_B the Bohr magneton and B the external applied magnetic induction), thereby reducing the exciton population at any given temperature. κ of both the Ta₂NiS₅ and Ta₂NiSe₅ in an applied magnetic field of 9 T was also measured. No change larger than error bar was observed. This is true for an external magnetic field applied along both the a and c directions. Assuming $g = 2$, the Zeeman energy at 9 T is of the order 2% of the gap and of exciton population; had this been important to κ , we could have picked up the effect just above the noise level of the measurements below 10K in κ of Ta₂NiSe₅. The fact that we did not observe a change of κ (or indeed specific heat) argues against the presence of a free excitonic contribution.

To look for an electronic contribution to κ , the electrical resistivity was measured, along with the Seebeck coefficient and Hall charge carrier concentration and mobility. In Ta₂NiS₅, Ta₂NiSe₅ along the a-direction and in Ta₂NiSe₅ along c-direction, the Wiedemann-Franz law with the free electron Lorenz ratio can be used to estimate the electronic contribution κ_E to the total thermal conductivity. This is reported in **Fig. 38d**: κ_E rapidly decays below 200 K in both selenide and sulfide. Taken in to account the departures from the free electron Lorenz ratio by amounts that are common in semiconductors,¹⁰⁸ κ_E is still at least four orders of magnitude smaller than κ at $T < 200$ K.

Thus κ is mostly free of contributions from by charged particles. Taken all together, the conclusion of the last four paragraphs is that the κ data **Fig. 38a** give the lattice thermal conductivity.

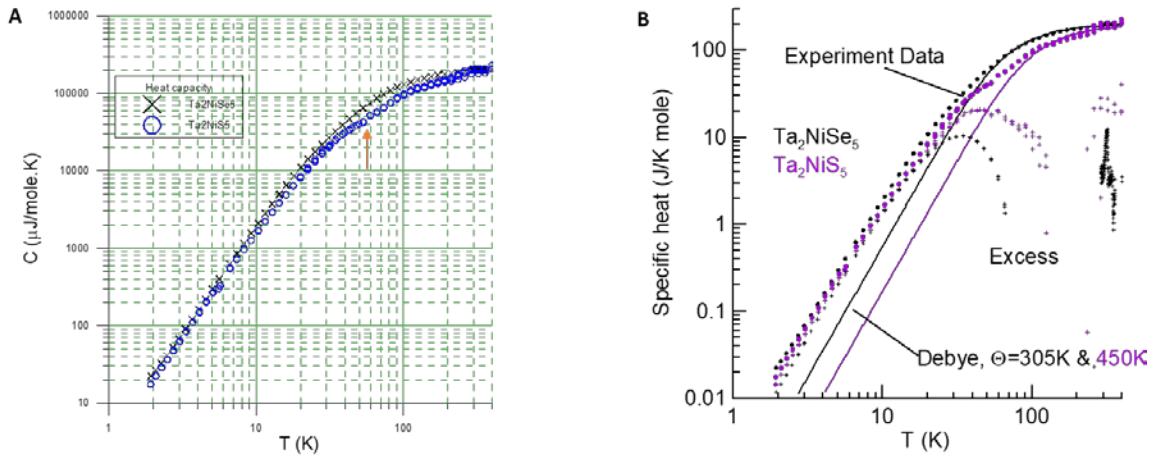


Figure 39. Specific heat of Ta_2NiSe_5 and Ta_2NiS_5

(A) Specific heat C data for Ta_2NiSe_5 and Ta_2NiS_5 . The C of Ta_2NiS_5 , but not that of Ta_2NiSe_5 , shows an excess heat below $T \sim 60$ K, equivalent to the energy of the 1.2 THz optical phonon mode. (B) Debye specific heat based on the Dulong-Petit value and Debye temperatures from **Table 5**. Subtracting these from the experimental data gives the excess C as marked. In the Ta_2NiSe_5 there is an excess at $T_c = 325$ K and around 40 K. In Ta_2NiS_5 the excess is at 50 K and is twice as large as in the selenide.

The heat capacity C data are reported in **Fig. 39a** for both Ta_2NiS_5 and Ta_2NiSe_5 . At $T < 10\text{K}$, C deviates slightly from the T^3 law, approaching $T^{2.5}$. Ta_2NiSe_5 shows a clear excess C at T_c . Except for that, at $T > 300\text{K}$ C approaches the Dulong Petit value $C_{D-P} = 3Rn = 199.548\text{J}/\text{mol}\cdot\text{K}$, for both compounds. C of both samples show deviation from a Debye function, but by different amounts: the deviation is very pronounced in the sulfide, where it turns into a cusp at $T < 60\text{K}$, as indicated by a red arrow in **Fig. 39a**. The specific heat measurements were also carried out in a magnetic field of 9T, but no difference is

found vis-à-vis the zero field data. In particular, no field-induced change is observed in the position of the peak in $C(T)$ near T_c in the selenide.

4.3. Discussion

Table 5. Calculated phonon properties of Ta_2NiSe_5 and Ta_2NiS_5

Calculated phonon properties	Unit	Ta_2NiSe_5			Ta_2NiS_5		
		a-axis	b-axis	c-axis	a-axis	b-axis	c-axis
ν , Sound velocity	m/s	3817	4300	2310	4611	5000	2610
θ , Debye temperature	K	305			447		
γ , Grüneisen parameter @ 300 K		1.42			1.36		
\bar{M} , Average atomic mass		101.92			72.6		
δ^3 , Volume primitive cell		344.55			306.39		
n , Number of atoms/prim. Cell		16			16		
Prefactor A		3.3E-08			3.35E-08		
κ a-axis (100K)	W/m K	33.4			100		

The present section thus starts from the argument made above that κ is dominated by phonon conduction. DFT calculation at 300 K provide values for the sound velocity and its anisotropy, the Debye temperature, and the energy-averaged Grüneisen parameter γ derived from the thermal expansion coefficient. From these calculated properties, it is possible to use the Slack formula¹⁰⁹ to obtain an estimate for the Umklapp-limited lattice thermal conductivity:

$$\kappa = A \frac{\bar{M} \theta^3 \delta}{\gamma^2 T n^{2/3}} \quad (4.1)$$

Where $A = 2.43 \cdot 10^{-8} / (1 - 0.514/\gamma + 0.228/\gamma^2)$ and the other variables are identified in **Table 5**. The values for κ at 100 K are also given in **Table 5**. For Ta₂NiSe₅, the calculated value is close to the experimental one. This is surprising: the Slack model produces reliable results for materials with small number of atoms per unit cell ($n < 3$). In materials with large number of atoms per unit cells, like Ta₂NiS₅ and Ta₂NiSe₅, Slack's model would be expected to become inaccurate due to the lowering in energy of optical phonon modes.¹⁰⁹ This holds for Ta₂NiS₅ but not for Ta₂NiSe₅. The fact that the calculated value is unexpectedly close to the experimental value at high temperature raises in Ta₂NiSe₅ is a first indication that the low-lying optical phonons play an important role in the κ of Ta₂NiS₅ but not in that of Ta₂NiSe₅.

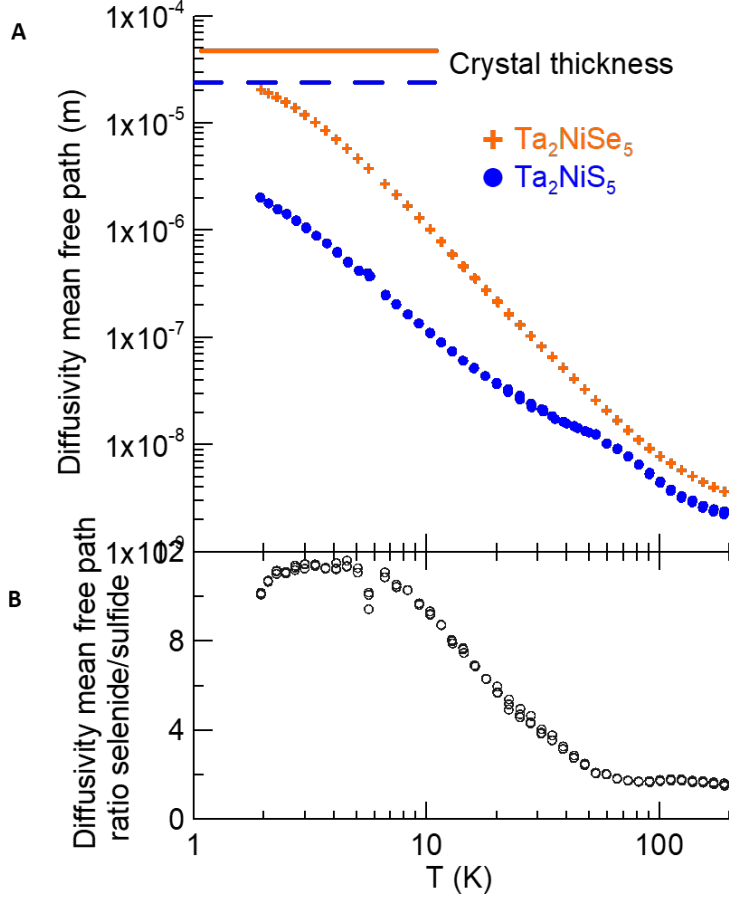


Figure 40. Mean free path calculated from the samples' diffusivity along the a-direction for the 50 μm thick Ta_2NiSe_5 and the 26 μm thick Ta_2NiS_5 samples, as function of temperature:

The behavior of Ta_2NiSe_5 is classical for phonon heat conduction and reaches asymptotically to the sample thickness, but that of the sulfide shows a pronounced cusp below 60K. The ratio of the two is shown in the bottom frame: it increases from about 1 above 60 K to over one order of magnitude below 8K.

Figure 40 shows the temperature-dependence of the mean free path λ of the heat-carrying phonons derived from the thermal diffusivity D , following the formula:

$$D = \frac{\kappa}{C'} = v\lambda \quad (4.2),$$

where C' is the volumetric heat capacity, and κ and v the thermal conductivity and sound velocity along the a-axis (v is taken from **Table 5**). For Ta_2NiSe_5 , λ tends asymptotically

toward the sample thickness, and the values are characteristic of phonon mean free paths limited by a combination of size, defect and Umklapp scattering, consistent with the assumption that heat is carried by phonons. The behavior of λ in Ta_2NiS_5 is best illustrated by contrasting it to that of the selenide as is done by plotting their ratio in **Fig. 40** (lower frame). This illustrates that above 100 K, both materials have similar heat conduction mechanisms, although the sulfide's λ is only about half of that of the selenide, but this difference in phonon-phonon scattering between the two materials grows to an order of magnitude below 60 K, which corresponds to a phonon frequency around 1 THz, and also to the temperature below which one observes new modes of vibration as an excess C .

The excess C is quantified in **Fig. 39b**. Here, Debye specific heats are plotted with values for θ from **Table 5** and C_{D-P} as high-temperature amplitude. The difference between the measured value and the Debye function is labeled an excess in C . In Ta_2NiSe_5 , it shows two maxima, one at T_c , and one near 30 K. Only one maximum is seen in Ta_2NiS_5 , at 45 K, but its intensity is twice that in Ta_2NiSe_5 . A search for the presence of an amorphous phase in the crystals revealed none and the fact that the mean free path in all samples reaches above 2 μm eliminates this possibility. This excess in C is therefore ascribed to an Einstein mode corresponding to the TO phonon at 1 THz in Ta_2NiSe_5 and 1.2 THz in Ta_2NiS_5 . In Ta_2NiSe_5 , the 1THz Ag mode phonon was reported to show anomalous behaviors below the phase transition.⁹⁵ It is known as a peculiar mode that couples to the excitonic system that affects its amplitude mode behavior.^{92,95} We argue that this coupling is the reason this mode's C is much lower in the selenide than in the sulfide. Indeed, Wachter reports a disappearance of phonon specific heat in $\text{TmSe}_{0.45}\text{Te}_{0.55}$.⁹⁶ He proposed

that when the phonon couples to the very heavy excitons it become more localized and no longer contribute significantly to the specific heat,^{96,99} and we observe the same effect in Ta₂NiSe₅.

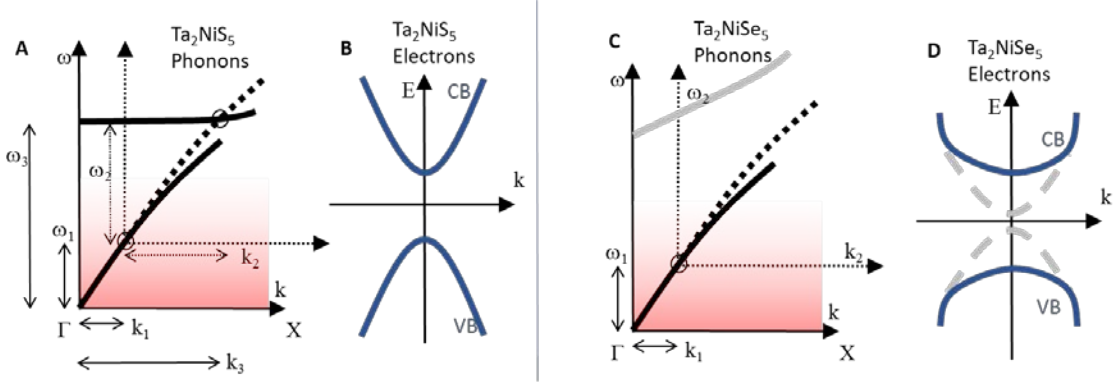


Figure 41. Schematic illustration of the phonon (A) and electron (B) dispersions in Ta₂NiS₅ and of the phonon (C) and electron (D) dispersions in Ta₂NiSe₅. In (A), two acoustic phonons, indexed 1 and 2 can interact and a point on the optical branch can be found such that the conditions $\hbar\omega_1 + \hbar\omega_2 = \hbar\omega_3$; $k_1 + k_2 = k_3$ are obeyed. In the proposed model, in the selenide the optical phonon (in light grey in frame C) hybridize with electronic states in (D) and develops a dispersion. Consequently, the optical branch in (C) can no longer interact strongly with the acoustic phonons via the conditions for conservation of momentum and energy during scattering

We extend the effect that the hybridization of the 1 THz mode has on C to its effect on κ using the diagram in **Fig. 41**, which gives very schematic electron and phonon dispersions. For the phonons, one acoustic mode (e.g. a TA mode), indexed 1. and the 1.2THz (sulfide) / 1 Thz (selenide) TO mode are shown. If phonon 1 collides with another TA phonon 2 (the shifted dashed dispersion), that constitutes a scattering event only if a state indexed 3 exists so that¹¹⁰ $\hbar\omega_1 + \hbar\omega_2 = \hbar\omega_3$; $k_1 + k_2 = k_3$. In the case of Ta₂NiS₅ (**Fig. 41a**) the TO phonon provides phase space so that this scattering event can happen, even below 60 K. At higher temperatures, higher-lying optical modes can supply such phase

space, but the 1.2THz mode is the lowest accessible optical mode available, and thus the dominant one at $T < 60$ K. Soft optical phonons that greatly increase the scattering phase space are responsible for extremely low thermal conductivity in other materials.^{111,112} In Ta_2NiSe_5 , the TO phonon (grey dashed line) is coupled with the exciton and develops a dispersion. We submit that, the dispersion developed makes the TO phonon behave like a Debye specific heat and reduces density of states. The higher energy of the TO phonon branch at finite k also makes it provides phase space for acoustic phonons to scatter into: this model explains both observations: the decrease in heat capacity and the increase in thermal conductivity.

Chapter 5. Thermal transport through magnetic ordering transitions of MnBi_2Te_4

5.1. Introduction

Crystalline materials that integrate both magnetism and topology are of emerging interest, as they often exhibit exotic anisotropic magneto-electro-thermal transport phenomena. One such material, MnBi_2Te_4 has attracted considerable recent attention as a potential magnetic topological insulator. MnBi_2Te_4 crystallizes in a rhombohedral lattice of space group $R\bar{3}m$ consisting of septuple van der Waals layers of Te-Bi-Te-Mn-Te-Bi-Te. This creates an intriguing structure that integrates a central layer of MnTe_6 octahedra inside the Bi_2Te_3 archetype, making it a magnetic relative of the 3D topological insulator (TI) Bi_2Te_3 . Bi_2Te_3 was first predicted as a TI by Fu and Kane in 2007 and that prediction has since been experimentally verified numerous times.^{113,114} In Bi_2Te_3 as well as MnBi_2Te_4 , the electronic states near the Fermi level mostly consist of Bi and Te p-orbital bands which exhibit band inversion. The Mn 3d bands, which contribute magnetic moments are many eV away from the Fermi level.¹¹⁵ In first-principles calculation work by Otrokov et al. in 2017,¹¹⁶ it was found that in MnBi_2Te_4 septuple layer, a rather large magnetically induced energy gap of the Dirac cones (up to 77 meV, much larger than the <1 meV gap in the more typical magnetically doped TIs) is opened at the topological surface states (TSSs) $\langle 0001 \rangle$, which promises a Chern insulator state, or a quantum anomalous Hall (QAH) state.^{116,117} Experimentally, Otrokov *et al.* showed that their prediction was correct with angle resolved photoemission spectroscopy (ARPES).¹¹⁸ Deng *et al.* and Liu *et al.* observed the QAH effect and zero longitudinal resistance in gated few

layers of MnBi_2Te_4 ^{19,119} in an external magnetic field in the out-of-plane direction. The external magnetic field flips individual ferromagnetic SLs and eventually fully polarizes all SLs where the sample becomes a robust QAH insulator.

Magnetic ordering in bulk MnBi_2Te_4 undergoes many transitions in both temperature and field. Intralayer Mn^{2+} ions are bonded to Te atoms in a slightly distorted octahedron. Thus, they experience ferromagnetic FM super-exchange through the Mn-Te-Mn bonds ($\sim 94^\circ$ bond angle). Above the Neel temperature, $T_N = 25$ K, MnBi_2Te_4 is a paramagnet. Below T_N , without an applied field, MnBi_2Te_4 has an A-type antiferromagnetic (AFM) structure: the Mn^{2+} spins have moments that are aligned in the out of plane direction, are ferromagnetically coupled within each layer, but are weakly antiferromagnetically coupled with neighboring layers. A-type AFM magnetic TIs (MTIs) like MnBi_2Te_4 are expected to reveal both topological axion insulating states with AFM ordering and QAHE depending on the number of layers and whether an external magnetic field is applied. The interplay between the magnetic structure and the topologically nontrivial bands endows the material with rich topological phases.^{118,120-122} In an out-of-plane magnetic field with temperatures below T_N , it is reported that the bulk magnetic ordering undergoes a spin-flop transition followed by a canted AFM ordering before the spins in all layers align, making MnBi_2Te_4 ferromagnetic at high field.^{123,124} The FM ordering is also very interesting as interlayer exchange coupling closes the band gap and induces band overlap; thus, in FM phase, MnBi_2Te_4 is a Type II Weyl semimetal with Weyl points separation from Γ -Z.¹²² The Weyl semimetals such as $\text{Bi}_x\text{Sb}_{1-x}$ have shown large changes in thermal and electrical conductivities when a magnetic field is oriented along the Weyl points as a consequence

of the thermal chiral anomaly.¹²⁵ Thus, the exploration of magnetothermal transport in a potential magnetic Weyl semimetal would be of great interest. We are not aware of any other published magneto-thermal transport studies to date.

Here we present the magnetothermal transport properties of MnBi_2Te_4 . We report field dependence of thermal conductivity κ in the in-plane direction under an applied magnetic field in the cross-plane direction in MnBi_2Te_4 from 2 K to 30 K. κ shows a decrease with field in the AFM phase which we attribute to enhanced magnon-phonon scattering and an increase in thermal conductivity in field in the FM phase. Thermal Hall data measured in the same configuration shows an anomalous thermal Hall at the spin-flop transition which strongly resembles the electrical Hall data and relates to it via the Wiedemann-Franz law. Thus, we conclude that the thermal Hall is of electronic origin. Magneto-thermoelectric data is also reported for the first time in bulk MnBi_2Te_4 . Particularly, from the results we can notice strong magnon-phonon interactions that suggest pathways for a new mechanism for magnetic field operated heat switches.

5.2. Results

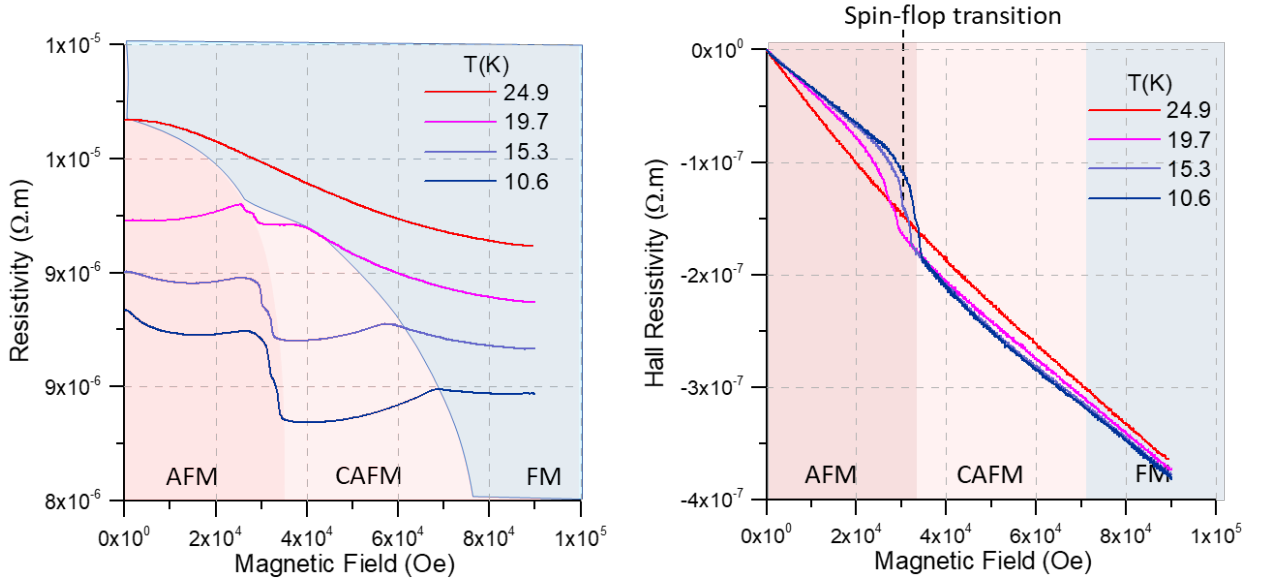


Figure 42. Electrical transport data. Left panel: Field dependence of in-plane resistivity. Right panel: Hall resistivity: At Spin flop transition, the resistivity drop, attributed to spin valve effect. Right panel: Hall resistivity $\rho_{xy}(B_z)$ shows anomalous Hall effect at the spin-flop transition.

Single crystals of $MnBi_2Te_4$ were grown by adapting the previously established flux method by slow cooling Bi_2Te_3 and $MnTe$ powders in approximately a 5:1 ratio into an alumina Canfield crucible and centrifuging at $595^\circ C$. Crystals having lengths and widths of 3-8 mm and thicknesses of 10 – 200 μm were prepared. Hall effect characterization of the carrier concentration (**Figure 42**) of studied samples shows that electrons are the majority charge carriers. Electron concentration at 20K is about $6 \cdot 10^{19} - 1 \cdot 10^{20} \text{ cm}^{-3}$. This is very similar to reported values typically ranging from $7 \cdot 10^{19} - 1 \cdot 10^{20} \text{ cm}^{-3}$.^{126,127} The carrier concentration indicates that the Fermi level is therefore about 0.3 eV into the conduction band.¹¹⁸ The n-type defects responsible for the intrinsic electron doping were explored by Hou *et al.* and Du *et al.* both experimentally and computationally.^{128,129} Like

Bi_2Te_3 , MnBi_2Te_4 growth faces challenges with donor $\text{Bi}_{\text{Mn}+}$ antisite defects,^{126,130} which heavily n-type dope the crystal.

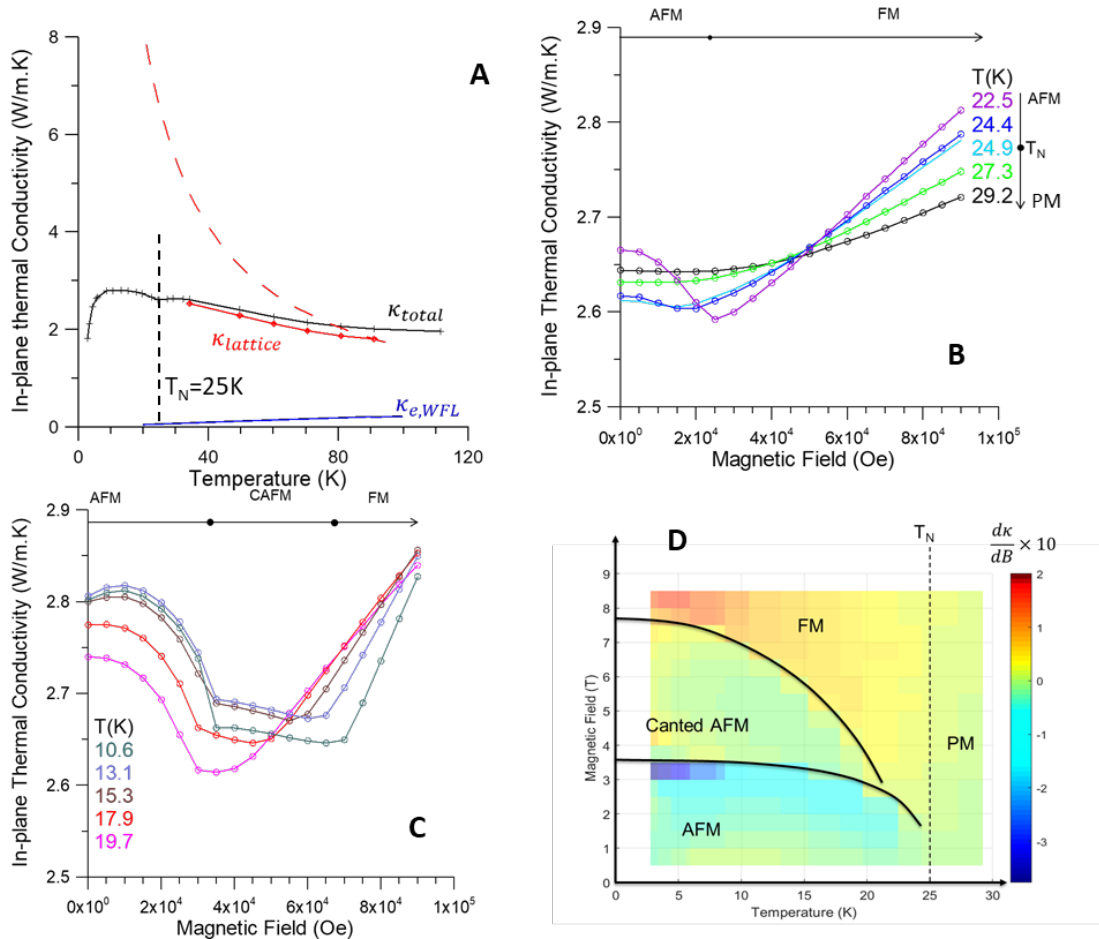


Figure 43. In-plane thermal conductivity of MnBi_2Te_4 :

(A) Temperature dependence of total in-plane thermal conductivity κ_{xx} . κ_{xx} decreases at the ordering temperature $T_N = 24.5\text{K}$ indicating scattering of phonon to magnon. The lattice thermal conductivity (in red) can be derived as the difference between the total thermal conductivity and the electronic thermal conductivity $\kappa_{lattice} = \kappa_{total} - \kappa_e$. Red dashed line is a $1/T$ law temperature dependence of phonon thermal conductivity for comparison, which illustrates the negative contribution to total thermal conductivity from spin scattering. (B, C) Field dependence of in-plane thermal conductivity $\kappa_{xx}(B_z)$. Across the ordering temperature, $\kappa_{xx}(B_z)$ develops contrasting behaviors at different field ranges. Above T_N , κ_{xx} plateaus at low field then slightly increases with field. Below T_N , κ_{xx} decreases with field at low field and increases linearly in field at high field. The magnetic field at which the field dependence changes correspond to the transition from AFM to FM ordering. Below 20 K, in addition to the initial decrease in AFM phase and linear increase in FM phase, there is a plateau in the intermediate Canted AFM ordering phase. (D) A

magnetic ordering phase diagram can be reconstructed from a map of $d\kappa/dB$. The large negative value near the boundary of AFM phase correspond to the spin-flop transition.

Figure 43A shows the temperature dependence of in-plane thermal conductivity κ_{xx} . Upon cooling down from 200 K, κ_{xx} initially decreases and forms a minimum at about 120 K. This decrease is attributed to the decrease in electronic thermal conductivity with temperature, shown in **Fig. 43A** as a blue line, obtained from the resistivity of the sample and using the Wiedemann-Franz law with the free-electron Lorenz ratio. The lattice thermal conductivity (in red) can be derived as the difference between the total thermal conductivity and the electronic thermal conductivity $\kappa_{lattice} = \kappa_{total} - \kappa_e$. At low temperature, the lattice thermal conductivity becomes dominant. An apparent suppression in κ_{xx} was observed at the Neel temperature $T_N = 24.5$ K. This is in agreement with data reported in the literature.¹³¹ Combined with the observation of a peak in heat capacity at the Neel temperature at zero field and absence of the peak at 9T field,¹³¹ this suggests the emergence of magnons and strong phonon-magnon scattering in the ordered phase. A similar behavior of $\kappa_{xx}(T)$ was observed in other magnetic materials near ordering temperature.¹³²⁻¹³⁴ The red dashed line shows a $1/T$ function through the highest temperature point that we calculated lattice thermal conductivity which is an expected temperature dependence of lattice thermal conductivity. $\kappa_{lattice}$ measured shows a clear deviation from this law, suggesting that phonon-magnon scattering greatly reduces the lattice thermal conductivity.

The field dependence of in-plane thermal conductivity $\kappa_{xx}(B_z)$ is shown in **Figure 43B**. Across the ordering temperature, $\kappa_{xx}(B_z)$ develops a non-monotonic field

dependence. Above T_N where the effect of magnetic scattering is observed, κ_{xx} slightly increases with field at high field. Below T_N , κ_{xx} decreases at low field and increases at high field. The magnetic field at which the slope $d\kappa_{xx} / dB$ changes correspond to the transition from AFM to FM ordering as shown in the magnetic ordering phase diagram in the literature.¹²³ Far below T_N , the canted AFM ordering phase appears in the intermediate field region. Our data in **Fig. 43C** shows that κ_{xx} saturates in this region with little field dependence. In the FM phase, the field dependence becomes a linear increase with field.

5.3. Discussion of in-plane thermal conductivity

Due to the small contribution of electronic thermal conductivity, the origin of the field dependence likely involves phonons since the electronic contribution is in the order of $0.05 \text{ W m}^{-1} \text{ K}^{-1}$ and the resistivity data shows less than a 2% change in an 9 T magnetic field at 25K. Above T_N , in a magnetic field, a paramagnet is polarized by the field and becomes ferromagnetic. In increasing magnetic field, the magnetic moments are stiffened thus magnetic scattering is reduced. This is consistent with the κ_{xx} data above T_N . The strong suppression of thermal conductivity in the AFM order and a sharp drop at the spin flop transition was also reported in a multiferroic material¹³⁵ although the origin was not well established. A linear increase with field of thermal conductivity was also reported in $\text{Na}_2\text{Co}_2\text{TeO}_6$ ¹³⁶ attributed to reduced phonon scattering. An increase in thermal conductivity at high field was observed in Bi-Sb TIs attributed to the thermal chiral anomaly, realized when an applied magnetic field is colinear with the heat flux and parallel to the WPs separation.¹²⁵ Although the FM phase of MnBi_2Te_4 is predicted to host a Type II Weyl semimetal state with Weyl points separation from Γ -Z,¹²² in this paper's

experimental setup, the applied heat flux direction is perpendicular to the WPs separation in the WSM phase. Theory of a Fermi arc mediated entropy transport in WSM¹³⁷ also predicted an increase of thermal conductance that is linear with an applied magnetic field that is perpendicular to the surfaces that host topologically protected Fermi arcs. In our experimental setup, it is possible that there is a small unintentional misalignment of the out-of-plane magnetic field so there can be a small in-plane magnetic field component $B_{in-plane}$ perpendicular to the arcs. However, no change was observed with the $B_{in-plane}$ component was increased by setting a small but intentional angle between the applied magnetic field and the sample's out-of-plane direction, in contradiction to the theory prediction of the $B_{in-plane}$ linear dependence of the Fermi arc mediated heat conduction. In the samples measured here, we noted that the position of the Fermi level of $MnBi_2Te_4$ is far (0.3 eV) from the bulk gap. Thus, the measured magnetothermal transport behavior is unlikely to be due to topological properties. It is striking, however, the contrast of the field dependence behavior of κ_{xx} in different magnetic ordering phase. From the $\kappa_{xx}(B_z)$ data we can reconstruct a phase diagram by plotting the derivative $d\kappa_{xx}/dB_z$ as function of B_z and T , and overlay that to the magnetic phase diagram as shown in **Fig 43D**. The reconstructed magnetic phase diagram using our thermal data shows stark similarities with the reported diagrams in literature.

5.4. Magnon band calculation in a magnetic field

To understand the behavior of the $\kappa_{xx}(B_z)$ data, we now discuss the evolution of the magnon bands and how they possibly interact with phonon dispersions. Atomistic spin dynamics based on the Heisenberg model using parameters from neutron diffraction

measurements¹³⁸ were used to calculate the magnon band dispersion in the ordered magnetic phases: AFM, CAFM and FM. The Hamiltonians are;

$$H = -\sum_{\langle ij \rangle, ||} J_{ij} S_i \cdot S_j - J_c \sum_{\langle ij \rangle, \perp} S_i \cdot S_j - D \sum_i (S_i^z)^2 - J_c^{aniso} \sum_{\langle ij \rangle, \perp} S_i^z S_j^z \quad (5.1)$$

where i labels the Mn ion with spin S_i at position R_i , J_c is the nearest-neighbor interlayer exchange, J_{ij} are the pairwise intralayer exchanges, D is the uniaxial single-ion anisotropy, and the last term of the Hamiltonian accounts for the anisotropic contribution in the interlayer interaction.

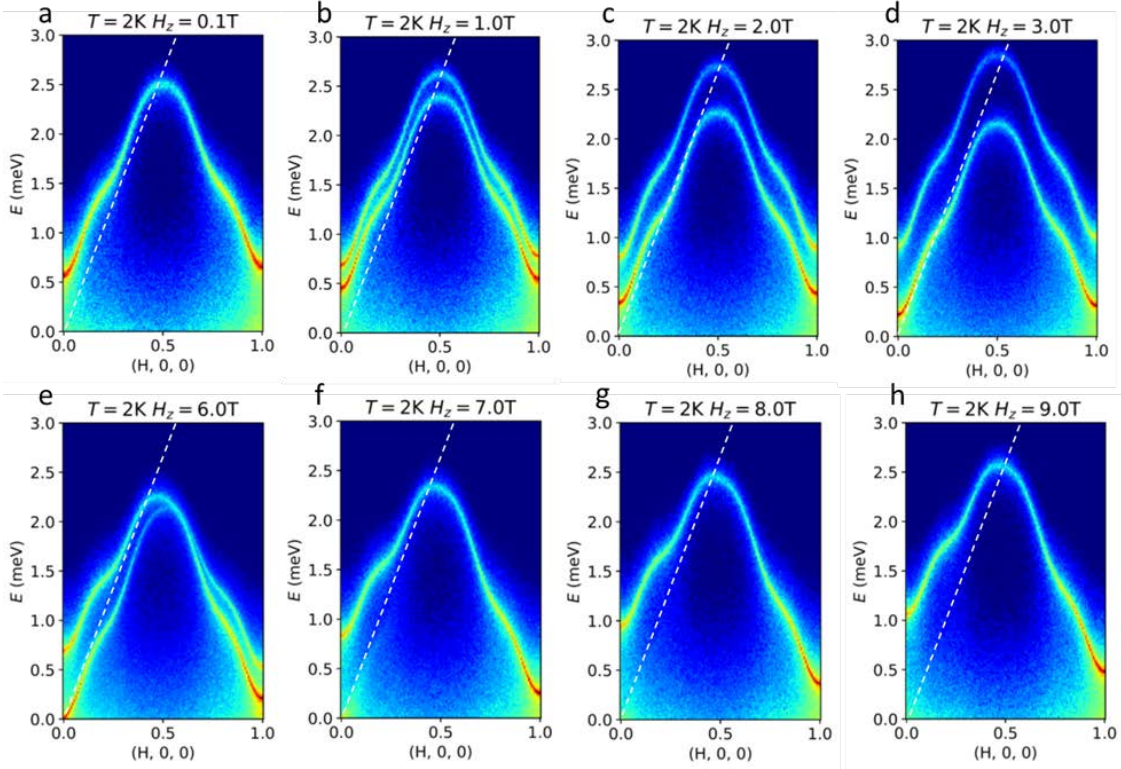


Figure 44. Calculated magnon band evolution in an out-of-plane magnetic field: (a-d) magnon bands in the AFM ordering phase (e,f) magnon bands in the canted AFM ordering phase and (g,h) magnon bands in FM ordering phase. Dashed line in qualitatively depicts an acoustic branch of phonon dispersion of MnBi₂Te₄ adopted from a monolayer phonon dispersion.

Figure 44 shows the calculated magnon band dispersions. In zero field, the system is in the AFM phase and the magnons have a near linear dispersion. A 0.6 meV energy gap at the zone center is induced by the magnetic anisotropy. The dashed lines qualitatively depicts an acoustic branch of phonon dispersion of MnBi_2Te_4 adopted from a monolayer phonon dispersion.¹²⁰ Although the bulk phonon dispersion may deviate from this dispersion, the deviation is expected to be small since both bulk MnTe and Bi_2Te_3 have similar acoustic phonon branches dispersing from 0 to 5 meV going from BZ center to BZ edge. Even at zero field, the magnon dispersion already has a large common phase space with this acoustic phonon. An external magnetic field along z breaks the symmetry between the spin-up and spin-down moments, thus splits the two degenerate AFM magnon branches split into two distinct bands with a gap proportional to the external field strength. Increasing the magnetic field causes one branch to blueshift to higher energy and redshifts the other branch. The redshifted branch gains more overlap in phase space with a gapless linear dispersing acoustic phonon branch as the field increases in AFM regime. This induces stronger magnon-phonon scattering and explains the decrease in $\kappa_{xx}(B_z)$. Once the energy gap of the lower AFM magnon dispersion is closed, further increasing the applied magnetic field will cause an instability in the magnetic order, producing the spin-flop transition. In the CAFM phase, there exist a gapless magnon branch attributed to a Goldstone mode and another high energy branch. The gapless mode retains its dispersion throughout the CAFM regime with little dependence on the magnetic field and overlaps well with the acoustic phonon mode. Thus the magnon-phonon scattering does not change as the magnetic field is increased in this phase. This is in excellent agreement with our experimental findings

that $\kappa_{xx}(B_z)$ is almost independent of field here. Finally, beyond the CAFM phase, the magnetic moments are forced to align with the magnetic field and the FM phase is established. In the FM phase the dispersion becomes a single FM branch. All Mn sites are now equivalent. The magnetic field increases the gap by a Zeeman energy, $g\mu_B B_{ext}$. The opening of the gap lifts the FM magnon dispersion to higher frequencies, thus reducing the phase space for scattering with phonons. This is consistent with the observation of a linear increase in thermal conductivity in the FM phase.

5.5. Thermoelectric and thermal Hall data

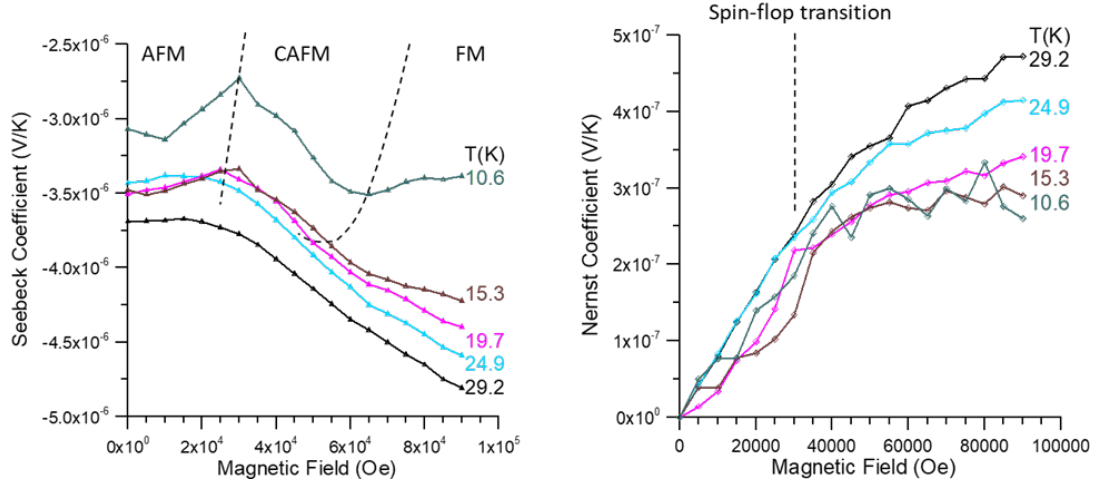


Figure 45. Field dependence of thermoelectric coefficients Seebeck $S_{xx}(B_z)$ (Left panel) and Nernst $N_{xy}(B_z)$ (Right panel):

Below T_N , Seebeck coefficient shows an increase with B in CAFM phase and plateau out at high field (FM). The Nernst coefficient shows a change of slope at the spin flop transition below T_N . The Nernst data shows behaviors of anomalous Nernst effect, even though the signal is small and noisy.

Figure 45 shows the field dependence of the thermoelectric coefficients Seebeck $S_{xx}(B_z)$ and Nernst $N_{xy}(B_z)$ at $T < 30$ K for the same sample. Both $S_{xx}(B_z)$ and $N_{xy}(B_z)$ are small in absolute value. The overall magnitude of S_{xx} is in the order of a few $\mu\text{V K}^{-1}$ in

the reported temperature range and a few tenths of $\mu\text{V K}^{-1}$ for N_{xy} . Although there are hopes for good thermoelectric properties of MnBi_2Te_4 because of its topological band structure, the small thermoelectric coefficients are consistent with a metallic system and are another result of the high Fermi level due to unintentional defect doping. Overall, the in-plane Seebeck coefficient and Nernst coefficient in an out-of-plane magnetic field is consistent with the resistivity and Hall resistivity data. In the canted AFM phase under T_N , the Seebeck coefficient is slightly increased, in accordance with the slight decrease of resistivity. The decrease in resistivity is attributed to the spin valve effect.¹³⁹ Nernst coefficient data shows behavior of anomalous Nernst effect and corresponds well with magnetization data. Below 20 K, $N_{xy}(B_z)$ has a small slope near zero field. At the spin flop transition, $N_{xy}(B_z)$ exhibits a jump where the jump due to spin-flop in magnetization data is observed.

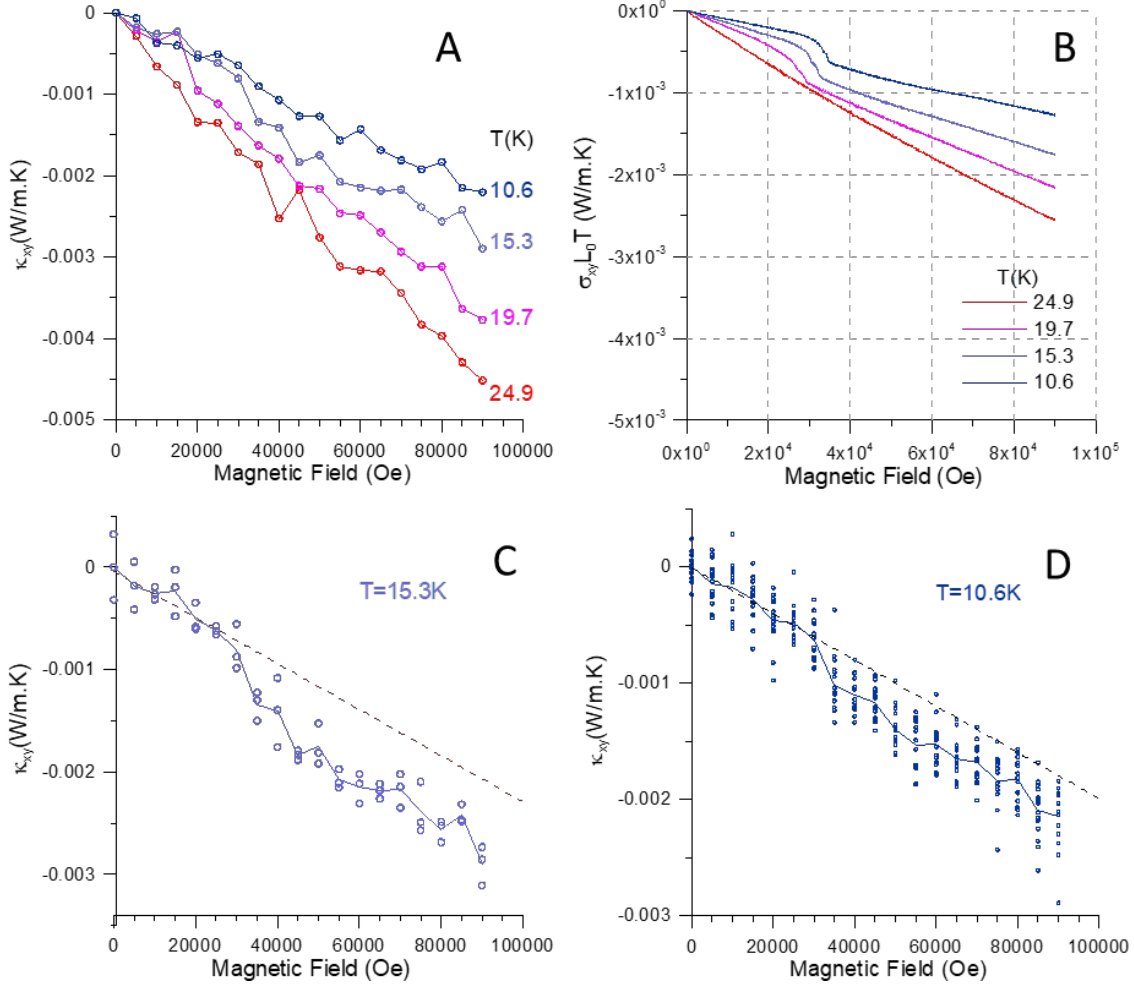


Figure 46. Thermal Hall and Hall shows good agreement with Wiedemann Franz Law: (A) Thermal Hall conductivity κ_{xy} measured below T_N . (B) Thermal Hall conductivity calculated from WFL $\kappa_{xy} = \sigma_{xy}L_0T$ at corresponding temperatures. (C,D) Blown-up plot of data at 15.3K and 10.6K shows a clear anomalous Thermal hall effect at spin flop transition. Quantitatively, thermal hall conductivity measured is about twice as large as values predicted by WFL.

The thermal Hall effect, κ_{xy} , was also measured and is reported in **Figure 46a**.

Above T_N , κ_{xy} is a linear function of field up to 9 T with the slope $d\kappa_{xy}/dB_z$ decreasing as the temperature decreases. Below T_N , κ_{xy} shows an abrupt increase at the spin-flop transition. One can observe the resemblance of the thermal Hall conductivity to the electrical Hall resistivity (**Fig. 42b**). In **Figure 46b**, we show the calculated thermal Hall

conductivity κ_{xy} using the Wiedemann Franz law, $\kappa_{xy} = \sigma_{xy}L_0T$, where L_0 is the free electron value. The calculated κ_{xy} is about half of the measured value for κ_{xy} . **Figure 46c** and **d** shows detailed raw data points and averaged curves at $T=10.6$ K and 15.3 K. A clear increase in κ_{xy} at 3.5 T at the spin flop transition is observed and can be attributed to the anomalous thermal Hall effect. The close agreement within an order of magnitude strongly indicates that the thermal Hall signal has an electronic origin from the bulk.

In summary, we show that MnBi_2Te_4 exhibits a significant and complex field-dependent magnetothermal conductivity and elucidate the mechanism to be of magnetic scattering origin. While the topological band structure of MnBi_2Te_4 promises novel thermal transport properties such as a quantized anomalous thermal Hall effect; the Fermi levels in these samples are far away from the band gap and thus, it is unlikely there is involvement of Weyl physics. Future studies on samples with greatly reduced doping levels may allow the realization of Weyl-induced magnetothermal transport phenomena.

Concluding Remarks

In this dissertation, we discussed solids in which thermal conductivity is tunable with external input. We investigated different sub-atomic particles and quasi-particles and their unique band structures to come up with new mechanisms to control their thermal transport properties.

The Bi-Sb alloys system with Sb concentration ranging 4-22 at. % shows highly-tunable electronic thermal conductivity $\kappa_{33}(B_3)$ attributed to the thermal chiral anomaly. Not only this is the first experimental realization of the thermal analog of the chiral anomaly, but the material system is also extremely promising in engineering a high-performance thermal switch. Our study has already showed a 300% increase in electronic thermal conductivity at 9 T without much optimization. The main drawback for this material system is its high background lattice thermal conductivity and small electronic thermal conductivity at low temperature. In order to optimize the performance of Bi-Sb alloys for thermal switching, the following steps are recommended:

- a. Investigate the effect of alloy scattering in Bi-Sb to lower the lattice thermal conductivity of Bi-Sb alloy. At the same time, examine the effect of Sb-doping on the thermal chiral anomaly to find the optimized Sb-doping concentration
- b. Investigate the effect of doping on the electronic thermal conductivity of Bi-Sb alloys and the effect of doping on the thermal chiral anomaly.
- c. Extend the measurement to low temperatures where lattice thermal conductivity is suppressed.

The thermal conductivity data of excitonic insulator Ta_2NiSe_5 shows possible hybridization of exciton to optical phonon that enhanced thermal transport in this material. The ability to melt the exciton condensate with high fluent LASER is promising in engineering a light activated heat switch. However, there are still challenges in proving the causal relationship between the enhanced thermal transport and the hybridization of exciton condensate and the optical phonons. Following steps are recommended:

- a. Investigate the effect of photo-excitation on thermal conductivity of Ta_2NiSe_5 . In my study, I have attempted to measure thermal conductivity of Ta_2NiSe_5 under the influence of a light source, however, the measurement method described in Section 2.3 is unfortunately not suitable for this type of experiment due to heat addition to the system from the light source. Perhaps an optical technique that is independent of heat flux measurement such as Frequency Domain Thermoreflectance (FDTR) or Time Domain Thermoreflectance (TDTR) will be more suitable for this investigation.
- b. Another possible approach to melt the exciton condensate is to change the Fermi level in-situ by making a gated device. Measuring with the electrical and thermal transport properties of the active layer in this device while varying the gate voltage may reveal the effect of the exciton condensate on both the electron and phonon band structure.

- c. An alternative approach to eliminate excitonic order is to dope Ta₂NiSe₅.

With dopant, the formation of exciton will be screened by free electron, thus preventing the formation of BEC and the structural transition.

We showed that MnBi₂Te₄ lattice thermal conductivity is greatly reduced by magnon-phonon scattering and revealed that the magnon band structure is responsible for this strong scattering. The scattering mechanism, remarkably, can be tuned with a magnetic field and can potentially be used to engineer a high switching ratio thermal switch. In order to build upon these findings, the following steps are recommended:

- a. Measure the sound velocity and calculate the phonon dispersion and the scattering phase space for each magnetic phase.
- b. It is also noteworthy that the magnon dispersion in MnBi₄Te₇ sister compound was also reported¹⁴⁰ with almost similar magnon dispersion and a vanished spin gap in the AFM phase. This promise even stronger magnon-phonon scattering at zero field. MnBi₄Te₇ also has smaller transition fields thus higher switching ratio at lower field.
- c. Finally, efforts to reduce unintentional doping level in MBT can bring the Fermi level down to interesting energy range in the bulk band gap in AFM phase and at the Weyl point in FM phase and enable additional thermal switching mechanisms such as the thermal chiral anomaly.

Bibliography

1. Gilmore, D. Spacecraft Thermal Control Handbook, Volume I: Fundamental Technologies. *Spacecraft Thermal Control Handbook, Volume I: Fundamental Technologies* (2002) doi:10.2514/4.989117.
2. Wehmeyer, G., Yabuki, T., Monachon, C., Wu, J. & Dames, C. Thermal diodes, regulators, and switches: Physical mechanisms and potential applications. *Applied Physics Reviews* **4**, 041304 (2017).
3. Ramirez, A. P. & Skinner, B. Dawn of the topological age? *Physics Today* **73**, 30 (2020).
4. McCormick, T. M. Electronic and Transport Properties of Weyl Semimetals. (2018).
5. Hirschberger, M. A. Quasiparticle Excitations with Berry Curvature in Insulating Magnets and Weyl Semimetals. (2017).
6. von Klitzing, K. The quantized Hall effect. *Reviews of Modern Physics* **58**, 519 (1986).
7. König, M. *et al.* Quantum spin hall insulator state in HgTe quantum wells. *Science* **318**, 766–770 (2007).
8. Chang, C. Z. *et al.* Experimental observation of the quantum anomalous Hall effect in a magnetic topological Insulator. *Science* **340**, 167–170 (2013).
9. Hasan, M. Z. & Kane, C. L. Colloquium: Topological insulators. *Reviews of Modern Physics* **82**, 3045–3067 (2010).
10. Xiao, D., Chang, M. C. & Niu, Q. Berry phase effects on electronic properties. *Reviews of Modern Physics* **82**, 1959–2007 (2010).
11. Kane, C. L. & Mele, E. J. \mathbb{Z}_2 topological order and the quantum spin hall effect. *Physical Review Letters* **95**, 146802 (2005).
12. Kaufmann, R. M., Li, D. & Wehefritz-Kaufmann, B. Notes on topological insulators. *Reviews in Mathematical Physics* **28**, (2016).
13. Kane, C. L. Topological Band Theory and the \mathbb{Z}_2 Invariant. *Contemporary Concepts of Condensed Matter Science* **6**, 3–34 (2013).
14. Hsieh, D. *et al.* A topological Dirac insulator in a quantum spin Hall phase. *Nature* **452**, 970–974 (2008).
15. Tokura, Y., Yasuda, K. & Tsukazaki, A. Magnetic topological insulators. *Nature Reviews Physics* **1**, 126–143 (2019).
16. Wang, P. *et al.* Intrinsic magnetic topological insulators. *The Innovation* **2**, 100098 (2021).
17. Li, J. *et al.* Intrinsic magnetic topological insulators in van der Waals layered MnBi₂Te₄-family materials. *Science Advances* (2019).

18. Otrokov, M. M. *et al.* Unique Thickness-Dependent Properties of the van der Waals Interlayer Antiferromagnet MnBi₂Te₄ Films. *Physical Review Letters* **122**, 107202 (2019).
19. Deng, Y. *et al.* Quantum anomalous Hall effect in intrinsic magnetic topological insulator MnBi₂Te₄. *Science* **367**, 895–900 (2020).
20. Yan, B. & Felser, C. Topological Materials: Weyl Semimetals. *Annual Review of Condensed Matter Physics* **8**, 337–354 (2017).
21. Weyl, H. Elektron und Gravitation. I. *Zeitschrift für Physik 1929 56:5* **56**, 330–352 (1929).
22. Nielsen, H. B. & Ninomiya, M. The Adler-Bell-Jackiw anomaly and Weyl fermions in a crystal. *Physics Letters B* **130**, 389–396 (1983).
23. Spivak, B. Z. & Andreev, A. v. Magnetotransport phenomena related to the chiral anomaly in Weyl semimetals. *Physical Review B* **93**, 085107 (2016).
24. Ashcroft, N. W. & Mering, N. D. *Solid state physics*. (Saunders College Publishing, 1976).
25. Berman, Robert. *Thermal conduction in solids*. (Clarendon Press Oxford, 1976).
26. Kittel, Charles. *Introduction to Solid State Physics*. (Wiley, 2007).
27. Heremans, J. P. Thermal spin transport and spin in thermoelectrics. *Advances in Thermoelectricity: Foundational Issues, Materials and Nanotechnology* 171–213 (2020) doi:10.48550/arxiv.2001.06366.
28. Boona, S. R. & Heremans, J. P. Magnon thermal mean free path in yttrium iron garnet. *Physical Review B* **90**, 064421 (2014).
29. Heremans, J., Shayegan, M., Dresselhaus, M. S. & Issi, J. P. High-magnetic-field thermal-conductivity measurements in graphite intercalation compounds. *Physical Review B* **26**, 3338 (1982).
30. Annett, J. F. Superconductivity, Superfluids and Condensates. *Oxford Master Series* 140 (2004).
31. Emsley, John. Nature’s building blocks : everything you need to know about the elements. *Oxford University Press* 699 (2011).
32. Keesom, W. H., Keesom, M. A. P. & Saris, B. F. A few measurements on the heat conductivity of liquid helium II. *Physica* **5**, 281–285 (1938).
33. Donnelly, R. J. The two-fluid theory and second sound in liquid helium. *Citation: Physics Today* **62**, 34 (2009).
34. Chase, C. E. Thermal Conduction in Liquid Helium II. I. Temperature Dependence. *Physical Review* **127**, 361 (1962).
35. Libbrecht, K. G., Black, E. D. & Hirata, C. M. A basic lock-in amplifier experiment for the undergraduate laboratory. (2003) doi:10.1119/1.1579497.
36. Larry, L. S., Robert, L. P. & William, J. H. *Reference Tables for Low-Temperature Thermocouples*. (1972).
37. Steinhart, J. S. & Hart, S. R. Calibration curves for thermistors. *Deep Sea Research and Oceanographic Abstracts* **15**, 497–503 (1968).
38. Wick, R. F. Solution of the Field Problem of the Germanium Gyration. *Journal of Applied Physics* **25**, 741 (2004).

39. Liang, S. *et al.* Experimental Tests of the Chiral Anomaly Magnetoresistance in the Dirac-Weyl Semimetals Na₃Bi and GdPtBi. *Physical Review X* **8**, 031002 (2018).
40. Chambers, R. G. The conductivity of thin wires in a magnetic field. *Proceedings of the Royal Society of London. Series A. Mathematical and Physical Sciences* **202**, 378–394 (1950).
41. Heremans, J. *et al.* Bismuth nanowire arrays: Synthesis and galvanomagnetic properties. *Physical Review B* **61**, 2921 (2000).
42. Heremans, J., Thrush, C. M., Lin, Y. M., Cronin, S. B. & Dresselhaus, M. S. Transport properties of antimony nanowires. *Physical Review B* **63**, 085406 (2001).
43. Baker, D. & Heremans, J. Linear geometrical magnetoresistance effect: Influence of geometry and material composition. *Physical Review B* **59**, 13927 (1999).
44. Noothoven van Goor, J. M. Donors and Acceptors in Bismuth. (1971).
45. Duthil, P. Material Properties at Low Temperature. *CERN Yellow Report CERN-2014-005* 77–95 (2014) doi:10.5170/CERN-2014-005.77.
46. Parma, V. Cryostat Design.
47. Arnold, F. *et al.* Negative magnetoresistance without well-defined chirality in the Weyl semimetal TaP. *Nature Communications* 2016 7:1 **7**, 1–7 (2016).
48. Huang, X. *et al.* Observation of the chiral-anomaly-induced negative magnetoresistance: In 3D Weyl semimetal TaAs. *Physical Review X* **5**, 031023 (2015).
49. Zhang, C. L. *et al.* Signatures of the Adler–Bell–Jackiw chiral anomaly in a Weyl fermion semimetal. *Nature Communications* 2016 7:1 **7**, 1–9 (2016).
50. Li, Q. *et al.* Chiral magnetic effect in ZrTe₅. *Nature Physics* 2016 12:6 **12**, 550–554 (2016).
51. Li, H. *et al.* Negative magnetoresistance in Dirac semimetal Cd₃As₂. *Nature Communications* 2016 7:1 **7**, 1–7 (2016).
52. Guo, S. T. *et al.* Large transverse Hall-like signal in topological Dirac semimetal Cd₃As₂. *Scientific Reports* 2016 6:1 **6**, 1–8 (2016).
53. Li, Y. *et al.* Resistivity plateau and negative magnetoresistance in the topological semimetal TaSb₂. *Physical Review B* **94**, 121115 (2016).
54. Li, Y. *et al.* Negative Magnetoresistance in Topological Semimetals of Transition-Metal Dipnictides with Nontrivial Z₂ Indices. *arXiv:1603.04056* (2016) doi:10.48550/arxiv.1603.04056.
55. Luo, Y. *et al.* Anomalous electronic structure and magnetoresistance in TaAs₂. *Scientific Reports* 2016 6:1 **6**, 1–7 (2016).
56. Shen, B., Deng, X., Kotliar, G. & Ni, N. Fermi surface topology and negative longitudinal magnetoresistance observed in the semimetal NbAs₂. *Physical Review B* **93**, 195119 (2016).
57. Hu, J., Rosenbaum, T. F. & Betts, J. B. Current jets disorder, and linear magnetoresistance in the silver chalcogenides. *Physical Review Letters* **95**, 186603 (2005).

58. Li, Y. *et al.* Negative magnetoresistance in Weyl semimetals NbAs and NbP: Intrinsic chiral anomaly and extrinsic effects. *Frontiers of Physics* 2017 12:3 **12**, 1–10 (2017).
59. Reis, R. D. D. *et al.* On the search for the chiral anomaly in Weyl semimetals: the negative longitudinal magnetoresistance. *New Journal of Physics* **18**, 085006 (2016).
60. Jin, H. *et al.* Phonon-induced diamagnetic force and its effect on the lattice thermal conductivity. *Nature Materials* 2014 14:6 **14**, 601–606 (2015).
61. Das, K. & Agarwal, A. Thermal and gravitational chiral anomaly induced magneto-transport in Weyl semimetals. *Physical Review Research* **2**, 013088 (2020).
62. Gallo, C. F., Chandrasekhar, B. S. & Sutter, P. H. Transport Properties of Bismuth Single Crystals. *Journal of Applied Physics* **34**, 144 (2004).
63. Andreev, A. v. & Spivak, B. Z. Longitudinal Negative Magnetoresistance and Magnetotransport Phenomena in Conventional and Topological Conductors. *Physical Review Letters* **120**, 026601 (2018).
64. Schindler, C. *et al.* Anisotropic electrical and thermal magnetotransport in the magnetic semimetal GdPtBi. *Physical Review B* **101**, 125119 (2020).
65. Gooth, J. *et al.* Experimental signatures of the mixed axial–gravitational anomaly in the Weyl semimetal NbP. *Nature* 2017 547:7663 **547**, 324–327 (2017).
66. Tolman, R. C. & Ehrenfest, P. Temperature Equilibrium in a Static Gravitational Field. *Physical Review* **36**, 1791 (1930).
67. Luttinger, J. M. Theory of Thermal Transport Coefficients. *Physical Review* **135**, A1505 (1964).
68. Vandaele, K., Otsuka, M., Hasegawa, Y. & Heremans, J. P. Confinement effects, surface effects, and transport in Bi and Bi_{1-x}Sb_x semiconducting and semimetallic nanowires. *Journal of Physics: Condensed Matter* **30**, 403001 (2018).
69. Liu, Y. & Allen, R. E. Electronic structure of the semimetals Bi and Sb. *Physical Review B* **52**, 1566 (1995).
70. Cucka, P. & Barrett, C. S. The crystal structure of Bi and of solid solutions of Pb, Sn, Sb and Te in Bi. *Acta Crystallographica* **15**, 865–872 (1962).
71. Mendez, E. E., Misu, A. & Dresselhaus, M. S. Pressure-dependent magnetoreflection studies of Bi and Bi_{1-x}Sb_x alloys. *Physical Review B* **24**, 639 (1981).
72. Brandt, N. B., Svistova, E. A. & Semenov, M. v. Electron transitions in antimony-rich bismuth–antimony alloys in strong magnetic fields. *Soviet Physics JETP* **32**, 434–444 (1971).
73. Şahin, C. & Flatté, M. E. Tunable Giant Spin Hall Conductivities in a Strong Spin-Orbit Semimetal: Bi_{1-x}Sb_x. *Physical Review Letters* **114**, 107201 (2015).
74. Cohen, M. H. & Blount, E. I. Philosophical Magazine The g-factor and de haas-van alphen effect of electrons in bismuth. *Philosophical Magazine* **5**, 115–126 (1960).
75. Smith, G. E., Baraff, G. A. & Rowell, J. M. Effective g Factor of Electrons and Holes in Bismuth. *Physical Review* **135**, A1118 (1964).

76. Vecchi, M. P., Pereira, J. R. & Dresselhaus, M. S. Anomalies in the magnetoreflexion spectrum of bismuth in the low-quantum-number limit. *Physical Review B* **14**, 298 (1976).
77. Kagan, V. D. & Red'ko, N. A. Phonon thermal conductivity of bismuth alloys. *Academy of Sciences of the USSR* **100**, 1205–121 (1990).
78. Argyres, P. N. & Adams, E. N. Longitudinal magnetoresistance in the quantum limit. *Physical Review* **104**, 900–908 (1956).
79. Wang, Z. *et al.* Evidence of high-temperature exciton condensation in two-dimensional atomic double layers. *Nature* 2019 574:7776 **574**, 76–80 (2019).
80. Kohn, W. Excitonic Phases. *Physical Review Letters* **19**, 439 (1967).
81. Seki, K. *et al.* Excitonic Bose-Einstein condensation in Ta₂NiSe₅ above room temperature. *Physical Review B - Condensed Matter and Materials Physics* **90**, 155116 (2014).
82. Jérôme, D., Rice, T. M. & Kohn, W. Excitonic Insulator. *Physical Review* **158**, 462 (1967).
83. Wakisaka, Y. *et al.* Excitonic insulator state in Ta₂NiSe₅ probed by photoemission spectroscopy. *Physical Review Letters* **103**, 026402 (2009).
84. Tang, T. *et al.* Non-Coulomb strong electron-hole binding in Ta₂NiSe₅ revealed by time- and angle-resolved photoemission spectroscopy. *Physical Review B* **101**, 235148 (2020).
85. Larkin, T. I. *et al.* Giant exciton Fano resonance in quasi-one-dimensional Ta₂NiSe₅. *Physical Review B* **95**, 195144 (2017).
86. Sunshine, S. A. & Ibers, J. A. Structure and Physical Properties of the New Layered Ternary Chalcogenides Ta₂NiS₅ and Ta₂NiSe₅. *Inorganic Chemistry* **24**, 3611–3614 (1985).
87. Mu, K. *et al.* Electronic structures of layered Ta₂NiS₅ single crystals revealed by high-resolution angle-resolved photoemission spectroscopy. *Journal of Materials Chemistry C* **6**, 3976–3981 (2018).
88. Ye, M. *et al.* Lattice dynamics of the excitonic insulator Ta₂Ni(Se_{1-x}S_x)₅. *Physical Review B* **104**, 045102 (2021).
89. Baldini, E. *et al.* The spontaneous symmetry breaking in Ta₂NiSe₅ is structural in nature. (2020).
90. Watson, M. D. *et al.* Band hybridization at the semimetal-semiconductor transition of Ta₂NiSe₅ enabled by mirror-symmetry breaking. *Physical Review Research* **2**, 013236 (2020).
91. Volkov, P. A. *et al.* Critical charge fluctuations and emergent coherence in a strongly correlated excitonic insulator. *npj Quantum Materials* 2021 6:1 **6**, 1–9 (2021).
92. Kim, M. J. *et al.* Phononic soft mode behavior and a strong electronic background across the structural phase transition in the excitonic insulator Ta₂NiSe₅. *Physical Review Research* **2**, 042039 (2020).
93. Kim, K. *et al.* Direct observation of excitonic instability in Ta₂NiSe₅. *Nature Communications* 2021 12:1 **12**, 1–8 (2021).

94. Volkov, P. A. *et al.* Failed excitonic quantum phase transition in Ta₂Ni(Se_{1-x}S_x)₅. *PHYSICAL REVIEW B* **104**, (2021).
95. Werdehausen, D. *et al.* Coherent order parameter oscillations in the ground state of the excitonic insulator Ta₂NiSe₅. *Science Advances* **4**, (2018).
96. Wachter, P. & Bucher, B. Exciton condensation and its influence on the specific heat. *Physica B: Physics of Condensed Matter Complete*, 51–57 (2013).
97. Remez, B. & Cooper, N. R. Effects of disorder on the transport of collective modes in an excitonic condensate. *Physical Review B* **101**, 235129 (2020).
98. Zittartz, J. Transport Properties of the “Excitonic Insulator”: Thermal Conductivity. *Physical Review* **165**, 612 (1968).
99. Wachter, P. & Wachter, P. Exciton Condensation and Superfluidity in TmSe_{0.45}Te_{0.55}. *Advances in Materials Physics and Chemistry* **8**, 120–142 (2018).
100. Takarada, S., Ogata, M. & Matsuura, H. Theory of thermal conductivity of excitonic insulators. *Physical Review B* **104**, 165122 (2021).
101. Bretscher, H. M. *et al.* Ultrafast melting and recovery of collective order in the excitonic insulator Ta₂NiSe₅. *Nature Communications* **2021 12:1** **12**, 1–8 (2021).
102. de Laeter, J. R. *et al.* Atomic weights of the elements. Review 2000 (IUPAC Technical Report). *Pure and Applied Chemistry* **75**, 683–800 (2003).
103. Morelli, D. T., Heremans, J. P. & Slack, G. A. Estimation of the isotope effect on the lattice thermal conductivity of group IV and group III-V semiconductors. *Physical Review B* **66**, 195304 (2002).
104. Zhang, Y. S., Bruin, J. A. N., Matsumoto, Y., Isobe, M. & Takagi, H. Thermal transport signatures of the excitonic transition and associated phonon softening in the layered chalcogenide Ta₂NiSe₅. *Physical Review B* **104**, L121201 (2021).
105. Bretscher, H. M. *et al.* Imaging the coherent propagation of collective modes in the excitonic insulator Ta₂NiSe₅ at room temperature. *Science Advances* **7**, (2021).
106. Atkins, K. R. Thermal Conductivity of Liquid Helium II in Very Narrow Channels. *Physical Review* **108**, 911 (1957).
107. Gor’kov, L. P. & Dzyaloshinskii, I. E. Contribution to the theory of the Mott exciton in a strong magnetic field. *Sov Phys JEPT* **26**, (1968).
108. Ziman, J. M. *Electrons and Phonons. Electrons and Phonons* (Oxford University Press, 2007). doi:10.1093/ACPROF:OSO/9780198507796.001.0001.
109. Slack, G. A. The Thermal Conductivity of Nonmetallic Crystals. *Solid State Physics - Advances in Research and Applications* **34**, 1–71 (1979).
110. Peierls, R. E. *Quantum Theory of Solids. Quantum Theory of Solids* (Oxford University Press, 2007). doi:10.1093/ACPROF:OSO/9780198507819.001.0001.
111. Delaire, O. *et al.* Giant anharmonic phonon scattering in PbTe. *Nature Materials* **2011 10:8** **10**, 614–619 (2011).
112. Yue, S. *et al.* Soft phonons and ultralow lattice thermal conductivity in the Dirac semimetal Cd₃As₂. *Physical Review Research* **1**, 033101 (2019).
113. Fu, L. & Kane, C. L. Topological insulators with inversion symmetry. *Physical Review B - Condensed Matter and Materials Physics* **76**, 045302 (2007).

114. Hasan, M. Z. & Kane, C. L. Colloquium: Topological insulators. *Reviews of Modern Physics* **82**, 3045–3067 (2010).
115. He, K. MnBi₂Te₄-family intrinsic magnetic topological materials. *npj Quantum Materials* vol. 5 (2020).
116. Otrokov, M. M. *et al.* Highly-ordered wide bandgap materials for quantized anomalous Hall and magnetoelectric effects. *2D Materials* **4**, 025082 (2017).
117. Mogi, M. *et al.* Tailoring tricolor structure of magnetic topological insulator for robust axion insulator. *Science Advances* **3**, (2017).
118. Otrokov, M. M. *et al.* Prediction and observation of an antiferromagnetic topological insulator. *Nature* **576**, 416–422 (2019).
119. Liu, C. *et al.* Robust axion insulator and Chern insulator phases in a two-dimensional antiferromagnetic topological insulator. doi:10.1038/s41563-019-0573-3.
120. Li, J. *et al.* Intrinsic magnetic topological insulators in van der Waals layered MnBi₂Te₄-family materials. *Science Advances* **5**, (2019).
121. Zhang, D. *et al.* Topological Axion States in the Magnetic Insulator MnBi₂Te₄ with the Quantized Magnetoelectric Effect. *Physical Review Letters* **122**, (2019).
122. Lei, C., Chen, S. & MacDonald, A. H. Magnetized topological insulator multilayers. *Proceedings of the National Academy of Sciences of the United States of America* **117**, 27224–27230 (2020).
123. Sass, P. M., Kim, J., Vanderbilt, D., Yan, J. & Wu, W. Robust A-Type Order and Spin-Flop Transition on the Surface of the Antiferromagnetic Topological Insulator MnBi₂Te₄. *Physical Review Letters* **125**, 037201 (2020).
124. Bac, S.-K. *et al.* Topological response of the anomalous Hall effect in MnBi₂Te₄ due to magnetic canting. *arXiv* arXiv:2103.15801 (2021).
125. Vu, D. *et al.* Thermal chiral anomaly in the magnetic-field-induced ideal Weyl phase of Bi_{1-x}Sbx. *Nature Materials* **20**, 1525–1531 (2021).
126. Yan, J. Q. *et al.* Evolution of structural, magnetic, and transport properties in MnBi_{2-x}SbxTe₄. *Physical Review B* **100**, (2019).
127. Chen, B. *et al.* Intrinsic magnetic topological insulator phases in the Sb doped MnBi₂Te₄ bulks and thin flakes. *Nature Communications* **10**, (2019).
128. Du, M. H., Yan, J., Cooper, V. R. & Eisenbach, M. Tuning Fermi Levels in Intrinsic Antiferromagnetic Topological Insulators MnBi₂Te₄ and MnBi₄Te₇ by Defect Engineering and Chemical Doping. *Advanced Functional Materials* **31**, (2021).
129. Hou, F. *et al.* Te-Vacancy-Induced Surface Collapse and Reconstruction in Antiferromagnetic Topological Insulator MnBi₂Te₄. *ACS Nano* **14**, 11262–11272 (2020).
130. Heremans, J. P., Cava, R. J. & Samarth, N. Tetradymites as thermoelectrics and topological insulators. *Nature Reviews Materials* vol. 2 (2017).
131. Zeugner, A. *et al.* Chemical Aspects of the Candidate Antiferromagnetic Topological Insulator MnBi₂Te₄. *Chemistry of Materials* **31**, 2795–2806 (2019).
132. Slack, G. A. Thermal Conductivity of CaF₂, MnF₂, CoF₂, and ZnF₂ Crystals. *Physical Review* **122**, 1451 (1961).

133. Kittel, C. Interaction of Spin Waves and Ultrasonic Waves in Ferromagnetic Crystals. *Physical Review* **110**, 836 (1958).
134. Slack, G. A. & Newman, R. Thermal Conductivity of MnO and NiO. *Physical Review Letters* **1**, 359 (1958).
135. Ideue, T., Kurumaji, T., Ishiwata, S. & Tokura, Y. Giant thermal Hall effect in multiferroics. *Nature Materials* **16**, 797–802 (2017).
136. Hong, X. *et al.* Strongly scattered phonon heat transport of the candidate Kitaev material Na₂Co₂TeO₆. *Physical Review B* **104**, (2021).
137. McCormick, T. M., Watzman, S. J., Heremans, J. P. & Trivedi, N. Fermi arc mediated entropy transport in topological semimetals. *Physical Review B* **97**, 195152 (2018).
138. Li, B. *et al.* Quasi-two-dimensional ferromagnetism and anisotropic interlayer couplings in the magnetic topological insulator MnBi₂Te₄. *Physical Review B* **104**, L220402 (2021).
139. Lee, S. H. *et al.* Spin scattering and noncollinear spin structure-induced intrinsic anomalous Hall effect in antiferromagnetic topological insulator MnBi₂Te₄. *Physical Review Research* **1**, (2019).
140. Li, B. Spin dynamics in the antiferromagnetic topological insulator MnBi₄Te₇. in *Bulletin of the American Physical Society* (American Physical Society, 2022).